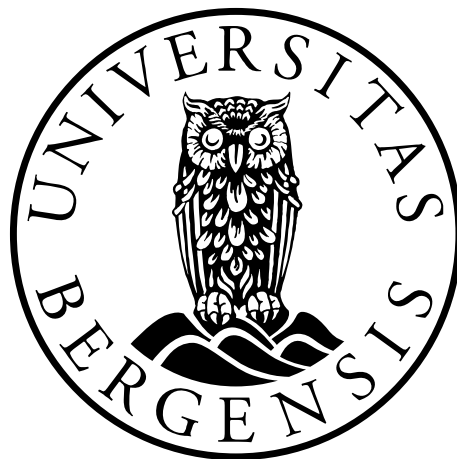


# **An *In vitro* Drug Study of Cabozantinib on Glioblastoma Cell Lines**

**Runar Oddvarson Hårklau**



This thesis is submitted in partial fulfilment of the requirements for the degree of Master of  
science – Biomedicine

The Faculty of Medicine and Dentistry – Department of Biomedicine

University of Bergen

Spring 2017



## Acknowledgements

I would like to give my greatest gratitude to my supervisor Prof. Frits Thorsen for letting me carry out my master project in your lab and introducing me to the exiting field of neuro-oncology. Thank you for all your help, interesting discussions, and motivating feedback throughout the last year.

Great thanks to my former co-supervisor postdoc Kislay Roy and PhD student Synnøve Nymark Aasen for helping me out in the lab and your willingness to always answering my many questions.

I would like to thank everyone in the Translational Cancer Research Group under the direction of Prof. Rolf Bjerkvig for creating such a friendly atmosphere and providing help whenever needed. A special thanks to Halala Sdik Saed, Anna Marie Moe and Berit Bølge Tysnes for technical support and guidance. Also, thanks to Prof. Martha Enger, postdoc Tor-Christian Aase Johannessen and researcher Lars Prestegarden for inputs regarding the western blot and your interest in my project.

Thanks to Hege Dale and Endy Spriet for helping me out with the imaging techniques, and running the confocal microscopy. Brith Bergum deserves great thanks for all your help regarding the flow cytometry.

Thanks to fellow master student Caroline Sørensen Singam for the exchange of ideas and excellent company in the lab.

Finally, great thanks to my family and friends for all your support and motivation. I would especially like to thank my mother and father for never ending encouragement.

Runar

Bergen May 2017



## Abstract

Glioblastoma is the most aggressive and frequently arising primary malignant brain tumor. Its rapid and invasive growth combined with complex aberrant signaling pathways and molecular alterations makes it refractory to treatment. The disease is associated with high morbidity, and despite application of all available treatment regimens, the survival rate is no more than 14.6 months.

Cabozantinib (XL 184) is a receptor tyrosine kinase inhibitor targeted against several surface receptors, including MET (mesenchymal-epithelial transition factor) and VEGFR-2 (vascular endothelial growth factor receptor 2), that are linked to overactive signaling pathways in cancer cells. The fact that cabozantinib can inhibit several of these receptors simultaneously, makes it a promising therapeutic agent against glioblastoma. The overall aim of this master thesis was to evaluate the effect of cabozantinib on four glioblastoma cell lines.

We carried out multiple *in vitro* experiments including cell viability and proliferation assays, flow cytometry analysis, assessment of the mitochondrial membrane potential, tumor spheroid based experiments, western blot, and a resistance evaluation.

Our results showed a dose-dependent reduction of cell viability in all four cell lines after treatment with cabozantinib. The drug inhibited cell proliferation, shown through a colony formation assay. The cells were arrested in the G<sub>2</sub>M phase of the cell cycle when a high dose of drug was introduced to the cells. Cabozantinib induced apoptosis in a dose-dependent manner, and lead to a depolarization of the mitochondrial gradient. Both growth and migration were significantly constrained in three-dimensional tumor spheroids. No alterations were observed on western blots of the MET and VEGFR-2 receptors, although several intracellular proteins were affected after treatment of cabozantinib, including AKT, mTOR and p27, suggesting an effect on the signaling pathways. The glioblastoma cells were not found to develop resistance towards the drug.

In conclusion, our work revealed an efficient reduction of tumorigenic traits after treatment with cabozantinib. However, we were not able to establish alteration of its targeted receptors.

---

## Abbreviations

ABBREVIATION	FULL NAME
AKT	Protein kinase B
AP-1	Activator protein 1 transcription factor
ATRX	Alpha thalassemia/mental retardation syndrome X-linked
AXL	Tyrosine-protein kinase receptor UFO
Bad	Bcl-2-associated death promoter
Bax	Bcl-2-associated X protein (Bcl-2-like protein 4)
BBB	Blood-brain barrier
BCA	Bicinchoninic acid
Bcl-2	B-cell lymphoma 2
Bcl-xL	B-cell lymphoma-extra large
BSA	Bovine serum albumin
BSC	Biosafety cabinet
CAK	Cyclin-dependent activating kinase
CDK	Cyclin-dependent kinase
CDK1	Cyclin-dependent kinase 1
CLSM	Confocal laser scanning microscopy
CNS	Central nervous system
CT	Computed tomography
CYP3A4	Cytochrome P450 3A complex
DAPI	4',6-diamidino-2-phenylindole
DIPG	Diffuse intrinsic pontine glioma
DMEM	Dulbecco's Modified Eagles Medium
ECM	Extracellular matrix
EGFR	Epidermal growth factor receptor
EthD-1	Ethidium homodimer-1
FasL	Fas ligand
FBS	Fetal bovine serum
FDA	Food and Drug Administration
FITC	Fluorescein isothiocyanate

---

FL	Fluorescent channel
FLAIR	Fluid attenuated inversion recovery
FOX	Forkhead box factor
FSC	Forward scattered light
G <sub>1</sub> phase	Gap 1 phase
G <sub>2</sub> M phase	Gap 2/mitotic phase
GAPDH	Glyceraldehyde 3-phosphate dehydrogenase
Gy	Gray
HBA	Hydrogen bond acceptor
HBD	Hydrogen bond donor
HGF	Hepatocyte growth factor
HIF-1 $\alpha$	Hypoxia-inducible factor 1 $\alpha$
HRP	Horseradish peroxidase
IC	Inhibitory concentration
IDH	Isocitrate dehydrogenase
IL-8	Interleukin 8
JC-1	5,5',6,6'-tetrachloro-1,1',3,3'- tetrathylbenzimidazolocarbo-cyanine iodine
KDR	Kinase insert domain receptor
logP	Logarithmical partition coefficient
MAPK/ERK	Mitogen-activated protein kinase/Extracellular signal- regulated kinase
MET/c-Met/HGFR	Mesenchymal-epithelial transition factor/Hepatocyte growth factor receptor
MGMT	O <sup>6</sup> -methylguanine-DNA methyltransferase
MRI	Magnetic resonance imaging
MTC	Medullary thyroid cancer
mTOR	Mechanistic (mammalian) target of rapamycin
mTORC1/2	Mechanistic target of rapamycin complex 1/2
MTT	3-(4,5-dimethylthiazol-2-yl)-2,5-diphenyltetrazolium bromide
NF- $\kappa$ B	Nuclear factor kappa-light-chain-enhancer of activated B cells
NSC	Neural stem cell
p14 <sup>ARF</sup>	Alternative Reading Frame protein, CDKN2A

---

p16	Cyclin-dependent kinase inhibitor 2A, multiple tumor suppressor 1, CDKN2A
p18	Cyclin-dependent kinase 4 inhibitor C, CDKN2C
p21	Cyclin-dependent kinase inhibitor 1A, CDKN1A
p27	Cyclin-dependent kinase inhibitor 1B, CDKN1B
PBS	Phosphate-buffered saline
PDA	Pancreatic ductal adenocarcinoma
PDGFR	Platelet-derived growth factor receptor
PE	R-phycoerythrin
PEITC	Phenethyl isothiocyanate
PET	Positron emission tomography
PFA	Paraformaldehyde
PI	Propidium iodide
PI3K	Phosphoinositide 3-kinase
PKC	Protein kinase C
PLC	Phospholipase C
PS	Phosphatidylserine
PTEN	Phosphatase and tensin homologue deleted on chromosome ten
PVDF	Polyvinylidene difluoride
Raf	Rapidly accelerated fibrosarcoma
Ras	Rat sarcoma
RB1	Retinoblastoma
RCC	Renal cell carcinoma
Resazurin	7-hydroxy-3 <i>H</i> -phenoxazin-3-one 10-oxide
RET	REarranged during Transfection
RT	Room temperature
RTK	Receptor tyrosine kinase
S phase	Synthesis phase
SRC	Proto-oncogene tyrosine kinase sarc
SSC	Side scattered light
$t_{1/2}$	Elimination half-time
TERT	Telomerase reverse transcriptase
TFF	Tumor treating fields
TMRE	Tetramethylrhodamine ethyl ester

TMZ	Temozolomide
TP53	Tumor protein p53
TRITC	Tetramethylrhodamine
uPAR	Urokinase plasminogen activator
VEGF	Vascular endothelial growth factor
VEGFR	Vascular endothelial growth factor receptor
VPLN	Vapor phase of liquid nitrogen
WHO	World Health Organization
$\Delta\psi$	Mitochondrial gradient
X <sup>o</sup>	Passage number X

## List of Figures and Tables

**Figure 1.1** Axial MRI images of glioblastoma WHO grade IV from a 70 year old man.

**Figure 1.2** Histological H&E-stained section of an astrocytoma WHO grade IV glioblastoma tumor, where several typical histological findings are present.

**Figure 1.3** A section of a brain in the coronal plane, affected by a glioblastoma showing the typical features represented by macroscopic examination.

**Figure 1.4** Overview of essential components in gliomagenesis.

**Figure 1.5** The structural formula of cabozantinib (XL 184).

**Figure 1.6** Structure formulas of the most essential metabolites of cabozantinib (XL 184).

**Figure 1.7** Delineated layout of the essential part of a flow cytometer.

**Figure 1.8** Overview of the microscopy imaging techniques used in this thesis.

**Figure 3.1** Template of the 96-well plate used in monolayer viability assay.

**Figure 3.2** Formula for calculating  $IC_{anything}$  from  $IC_{50}$  and the hill slope obtained from the drug-response curve

**Figure 3.3** Gating and analysis in FlowJo for the cell cycle analysis.

**Figure 3.4** Gating and analysis in FlowJo for the apoptosis assay

**Figure 3.5** Overview of the long-term treatment regime.

**Figure 4.1** Dose-response curves for the viability using the resazurin assay for the four cell lines.

**Figure 4.2** Viability bright-field and LIVE/DEAD<sup>®</sup> images of the A172 cell line.

**Figure 4.3** Viability bright-field and LIVE/DEAD<sup>®</sup> images of the U-87 MG cell line.

**Figure 4.4** Viability bright-field and LIVE/DEAD<sup>®</sup> images of the U-251 MG cell line.

**Figure 4.5** Viability bright-field and LIVE/DEAD<sup>®</sup> images of the GaMG cell line.

**Figure 4.6** Images of colonies from the A172 cell line

**Figure 4.7** Images of colonies from the U-87 MG cell line.

**Figure 4.8** Images of colonies from the U-251 MG cell line.

**Figure 4.9** Images of colonies from the GaMG cell line.

**Figure 4.10** Number for colonies formed after seeding 1000 cells.

**Figure 4.11** Cell cycle analysis of the A172 cell line.

**Figure 4.12** Cell cycle analysis of the U-87 MG cell line.

**Figure 4.13** Cell cycle analysis of the U-251 MG cell line.

**Figure 4.14** Cell cycle analysis of the GaMG cell line.

**Figure 4.15** Flow cytometry-based apoptosis distribution of the A172 cell line.

**Figure 4.16** Flow cytometry-based apoptosis distribution of the U-87 MG cell line.

**Figure 4.17** Flow cytometry-based apoptosis distribution of the U-251 MG cell line.

**Figure 4.18** Flow cytometry-based apoptosis distribution of the GaMG cell line.

**Figure 4.19** Quantification of the flow cytometry-based apoptosis assay.

**Figure 4.20** Mitochondrial gradient disruption in the A172 cells.

**Figure 4.21** Mitochondrial gradient disruption in the U-87 MG cells.

**Figure 4.22** Mitochondrial gradient disruption in the U-251 MG cells.

**Figure 4.23** Mitochondrial gradient disruption in the GaMG cells.

**Figure 4.24** Images of A172 spheroids over a 21-days treatment regime.

**Figure 4.25** Images of U-87 MG spheroids over a 21-days treatment regime.

**Figure 4.26** Images of U-251 MG spheroids over a 21-days treatment regime.

**Figure 4.27** Images of GaMG spheroids over a 21-days treatment regime.

**Figure 4.28** Growth curves of tumor spheroids for all cell lines.

**Figure 4.29** Migration assay of A172 spheroids.

**Figure 4.30** Migration assay of U-87 MG spheroids.

**Figure 4.31** Migration assay of U-251 MG spheroids.

**Figure 4.32** Migration assay of GaMG spheroids.

**Figure 4.33** Representative confocal scanning microscopy images of the GaMG spheroids.

**Figure 4.34** Western blots of tyrosine kinase receptors.

**Figure 4.35** Western blots of intracellular proteins.

**Figure 4.36** Resazurin assay after 5 passages

**Figure 4.37** Resazurin assay after 10 passages.

**Figure 4.38** Counting assay after 10 passages.

**Table 1.1** The 2016 CNS WHO grading scale of astrocytoma originating tumors

**Table 4.1** Overview of the mean  $IC_{50}$  doses and related standard deviation (SD) from the resazurin assay.

**Table 4.2** The other IC doses used in this thesis based on the  $IC_{50}$  values and graphs from the resazurin assay.

**Table 4.3** Results on the final day of spheroid treatment.

**Table 4.4** Fold resistance from the resazurin assay.

---

## Table of Contents

<b>ACKNOWLEDGEMENTS</b> .....	<b>III</b>
<b>ABSTRACT</b> .....	<b>V</b>
<b>ABBREVIATIONS</b> .....	<b>VI</b>
<b>LIST OF FIGURES AND TABLES</b> .....	<b>X</b>
<b>1. INTRODUCTION</b> .....	<b>1</b>
1.1 GLIOMAS – BACKGROUND, CLASSIFICATION AND GRADING .....	1
1.2 GLIOBLASTOMA – PATHOLOGY AND CLINICAL DIAGNOSIS.....	2
1.3 TUMOR MARKERS, CAUSES AND RISK FACTORS .....	5
1.4 CELL SIGNALING AND GENETIC ALTERATIONS OF GLIOBLASTOMA .....	6
1.5 CURRENT AND NOVEL TREATMENT STRATEGIES.....	9
1.6 CABOZANTINIB (XL 184) .....	10
1.7 EXPERIMENTAL BACKGROUND AND ANALYTICAL TECHNIQUES.....	12
1.7.1 <i>Cell Lines as Reflective Models of Cancer</i> .....	12
1.7.2 <i>Flow Cytometry</i> .....	13
1.7.3 <i>Microscopy Imaging Techniques</i> .....	14
<b>2. AIMS</b> .....	<b>16</b>
<b>3. MATERIALS AND METHODS</b> .....	<b>17</b>
3.1 CELL LINES.....	17
3.2 GENERAL CELL CULTURE TECHNIQUES.....	17
3.2.1 <i>Thawing</i> .....	18
3.2.2 <i>Passaging</i> .....	18
3.2.3 <i>Cryopreservation</i> .....	19
3.3 EXPERIMENTAL GROUNDWORK.....	19
3.3.1 <i>Mycoplasma Testing</i> .....	19
3.3.2 <i>Cell Counting</i> .....	20
3.3.3 <i>Drug Preparation</i> .....	20

---

3.4	MONOLAYER VIABILITY EXPERIMENTS .....	20
3.4.1	<i>Resazurin Assay</i> .....	20
3.4.2	<i>Obtaining IC Doses</i> .....	21
3.4.3	<i>Imaging – Bright-field and LIVE/DEAD® Fluorescence</i> .....	22
3.5	CELL TUMORIGENICITY – CLONOGENIC ASSAY .....	22
3.6	CELL CYCLE ANALYSIS .....	23
3.7	APOPTOSIS ASSAY .....	24
3.8	MITOCHONDRIAL MEMBRANE POTENTIAL .....	25
3.8.1	<i>Fluorimetric Quantification</i> .....	26
3.8.2	<i>Imaging</i> .....	26
3.9	GROWTH INHIBITION OF TUMOR SPHEROIDS .....	26
3.10	MIGRATION ASSAY .....	27
3.11	CLSM EVALUATION OF TUMOR SPHEROIDS .....	27
3.12	PROTEIN ANALYSIS – WESTERN BLOT .....	28
3.12.1	<i>Cell Lysate Preparation</i> .....	28
3.12.2	<i>Estimation of Protein Content – BCA Assay</i> .....	29
3.12.3	<i>Western Blot</i> .....	29
3.13	LONG-TERM TREATMENT WITH CABOZANTINIB .....	31
<b>4.</b>	<b>RESULTS</b> .....	<b>33</b>
4.1	MONOLAYER VIABILITY EXPERIMENTS .....	33
4.2	CELL TUMORIGENICITY – CLONOGENIC ASSAY .....	36
4.3	CELL CYCLE ANALYSIS .....	39
4.4	APOPTOSIS ASSAY .....	41
4.5	MITOCHONDRIAL MEMBRANE POTENTIAL .....	44
4.6	GROWTH INHIBITION OF TUMOR SPHEROIDS .....	46
4.7	MIGRATION ASSAY .....	49
4.8	CLSM EVALUATION OF TUMOR SPHEROIDS .....	51

---

4.9	PROTEIN ANALYSIS – WESTERN BLOT.....	52
4.10	LONG-TERM TREATMENT WITH CABOZANTINIB .....	53
<b>5.</b>	<b>DISCUSSION.....</b>	<b>56</b>
5.1	MONOLAYER VIABILITY .....	56
5.2	CELL TUMORIGENICITY – CLONOGENIC ASSAY .....	57
5.3	FLOW CYTOMETRY ASSAYS .....	58
5.4	MITOCHONDRIAL MEMBRANE POTENTIAL.....	61
5.5	TUMOR SPHEROID BASED ASSAYS .....	62
5.6	WESTERN BLOT.....	64
5.7	LONG-TERM TREATMENT WITH CABOZANTINIB.....	67
5.8	SUMMARY AND FUTURE PERSPECTIVES.....	68
	<b>REFERENCES .....</b>	<b>70</b>



# 1. Introduction

## 1.1 Gliomas – Background, Classification and Grading

A brain tumor is an abnormal formation of tissue in the brain parenchyma. Primary brain tumors are neoplasms arising within the brain, and they can be both benign (noncancerous) or malignant (cancerous) [1]. The central nervous system (CNS) consists of two classes of cells: neurons and neuroglia [2]. Neuroglia (i.e. astrocytes, oligodendrocytes, microglia) works as accessory cells for the neurons. They provide the neurons with mechanical support, nutrient supply, removal of waste products and formation of protective myelin sheets. Whereas neurons seldom have the capability to become cancerous, the neuroglia can transform into cancer cells. Tumors arising from glial cells are called gliomas, and are the most common type of primary brain tumors [3]. Gliomas are designated according to cell type and the location within the brain cortex, and they display a heterogeneous group of tumors. The glial cells consist of several cell types. The three most important ones from an oncologic point of view are astrocytes, oligodendrocytes, and ependymal cells. They give rise to astrocytoma, oligodendroglioma and ependymoma, respectively [4].

The classification and diagnosis of gliomas have largely been based on the thorough criteria document compiled by the World Health Organization (WHO) from 2007 [5]. In 2016, the WHO classification system for CNS tumors was revised, giving more focus to genetic alterations commonly found in gliomas [6]. During the last years, comprehensive research has been carried out on the molecular biology of gliomas, and the revised classification system has incorporated these results [6]. The status of the isocitrate dehydrogenase 1 (*IDH1*) gene is now used to characterize glial tumors. Gliomas are WHO graded on a scale from I to IV, where WHO grade I is the most benign and WHO grade IV (glioblastoma) is the most malignant. Tumors of WHO grade I – II (low grade) are most often found in younger patients, and WHO grade III – IV (high grade) are more common among the adult population. Gliomas in children tend to be infratentorial (in the cerebellum and brainstem) whereas adult gliomas are mostly supratentorial (in the cerebrum) [7].

Astrocytomas are the most prevalent class of gliomas [7]. They make up around 65% of all malignant primary brain tumors, and 75 % of all gliomas originates from astrocytes [8]. The different types of astrocytic tumors and their grading are given in **Table 1.1**. These tumors can be both benign and malignant, but the malignant ones are predominating. The pilocytic astrocytoma and subependymal giant cell astrocytoma WHO grade I are prevalent among the cases of astrocytoma diagnosed in children. This type is benign and nowadays mostly cured if surgical resection is achievable. The other cases of astrocytoma tend to recur, display malignancy and are rarely curable.

**Table 1.1** The 2016 CNS WHO grading scale of astrocytoma originating tumors [6]. Tumors are graded on a scale of I to IV, and the *IDH1* gene is used to subtype the tumors.

<b>WHO Grade</b>	<b>Name of Tumor</b>
<i>I (low)</i>	Pilocytic astrocytoma Subependymal giant cell astrocytoma
<i>II (low)</i>	Diffuse astrocytoma, <i>IDH</i> -wildtype Diffuse astrocytoma, <i>IDH</i> -mutant Pleomorphic xanthoastrocytoma
<i>III (high)</i>	Anaplastic astrocytoma, <i>IDH</i> -wildtype Anaplastic astrocytoma, <i>IDH</i> -wildtype Anaplastic pleomorphic xanthoastrocytoma
<i>IV (high)</i>	<b>Glioblastoma, <i>IDH</i>-wildtype</b> <b>Glioblastoma, <i>IDH</i>-mutant</b> Diffuse midline glioma

## 1.2 Glioblastoma – Pathology and Clinical Diagnosis

Glioblastoma is an astrocytoma WHO grade IV tumor (**Table 1.1**), and the most common malignant primary tumor of the CNS [9]. It counts for over half of all astrocytoma and around 45 % of all malignant CNS tumors, with an incident rate of 3.19 per 100 000 per year. In the United States between 2006 and 2010, the number of patients diagnosed with glioblastoma was 50 872 [8]. Glioblastoma is one of the most aggressive types of cancer, and the causes are still not fully understood. The disease is associated with a high rate of morbidity and mortality. Despite improvements in the treatment of glioblastoma, the median survival rate is no more than 14.6 months [10, 11]. The 5-year relative survival rate of European patients diagnosed with glioblastoma has been estimated to 2.7 % [12].

Glioblastoma affects people at any age, but is more common among the elderly, especially between 64 and 70 years of age [7, 13]. Although rare, the disease also occurs in children.

The prognosis worsens proportionally with increasing age, and among the older patients the survival time is as poor as 4-11 months [13]. Males are more commonly affected than females, with a 3:2 male to female ratio [14].

Common clinical symptoms that could indicate an intracranial tumor are dependent on localization, and include headache due to increased intracranial pressure, focal neurological deficits, cognitive dysfunction, visual impairment, nausea, mood change, paralysis, speaking difficulties and seizures [15]. Although glioblastoma can occur anywhere within the brain, the frontal lobe is the most predominant site of location [8]. The frontal lobe make up 2/3 of the cortex and is involved in important functions like defining personality traits, concentration and emotion [16].

If a patient is suspected to have a brain tumor, a computed tomography (CT) scan or a magnetic resonance imaging (MRI) scan is usually obtained [14]. During the last years, there have been continuous improvements in MR technology, making MRI the first choice in diagnostics of brain tumors due to excellent soft tissue contrast [17]. The most common techniques are  $T_1$ -weighted spin-echo (SE) sequences and  $T_2$ -fluid attenuated inversion recovery (FLAIR) sequences, often combined with gadolinium-based contrast agents [14]. The description of the physics behind MR imaging is beyond the scope of this thesis. The  $T_1$ - and  $T_2$ -weighted imaging techniques highlights different tissues of the glioma, based on the dark (hypointense) to light (hyperintense) relationship (**Figure 1.1**). Structures appearing dark on  $T_1$  are bright on  $T_2$ , and the other way around.  $T_1$  images are good at locating lesions within the brain and  $T_2$ -FLAIR visualize edema within and around the tumor.

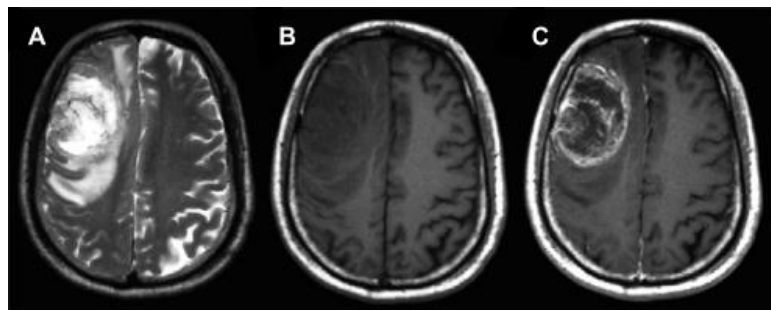


**Figure 1.1** Axial MRI images of a glioblastoma WHO grade IV from a 70 year old man. **A)**  $T_2$  weighted image showing the vascularity within and around the tumor as white (hyperintense) areas. **B)**  $T_1$  weighted image revealing a black (hypointense) lesion. **C)**  $T_1$  weighted image with contrast agent, indicating a large invasive tumor within the brain including border definition. Reprinted (*Open Access*) from [18].

Even though advanced imaging techniques are essential in the diagnosis of glioblastoma, a pathohistological examination of a biopsy from the tumor tissue is important in order to establish the correct diagnose. Histological features present in glioblastoma includes poor cellular differentiation, pleomorphism (including hyperchromatism), high cell density, nuclear atypia, mitotic activity, vascularity (blood vessels) and necrosis [14] (**Figure 1.2**). If all the criteria are present except for high vascular proliferation and necrosis, the diagnose will be anaplastic astrocytoma WHO grade III. If, however vascular proliferation and necrosis is present, the diagnose will be a glioblastoma WHO grade IV tumor.

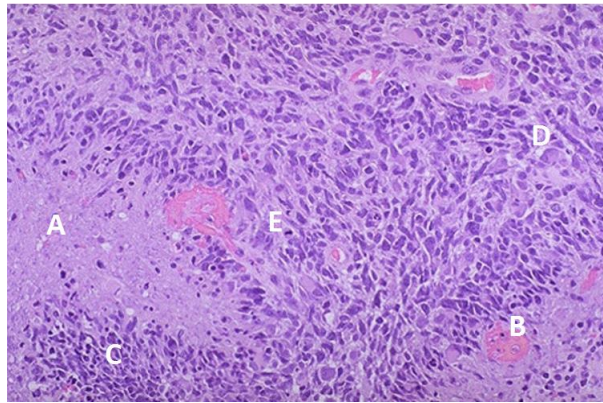


**Figure 1.2** Histological H&E-stained section of an astrocytoma WHO grade IV glioblastoma tumor, were several typical histological findings are present. **A)** necrosis, **B)** vascularization, **C)** high cell density, **D)** pleomorphism and **E)** hyperchromatism. Feature **A** and **B** are unique to the glioblastoma disease. Modified and reprinted with permission from [19].

Glioblastoma has a highly invasive and infiltrative growth pattern. Tumor cells have the capability to invade large region of the cortex, and can form tumors of considerable sizes before symptoms are present. Glioblastomas are highly vascular tumors consisting of comprehensive angiogenesis. The relationship between hypoxia and angiogenesis is important in glioblastoma (**Figure 1.3**). The figure shows a coronal section of a tumor representing epidemic vascularity and hemorrhage. There is also spread to the contralateral hemisphere through the *Corpus callosum*, leading to infiltration of multiple lobes. The excessive fluid leakage can lead to peritumoral edema, which can easily be visualized as a heterogeneous assessment in an  $T_2$ -weighted MRI image (**Figure 1.1**). This vasogenic edema is associated with increased intracranial pressure, which can lead to life threatening

transtentorial- or tonsillar herniation [13]. Many patients with glioblastoma die as a cause of compression of the breathing center in the brain stem, because of brain herniation.

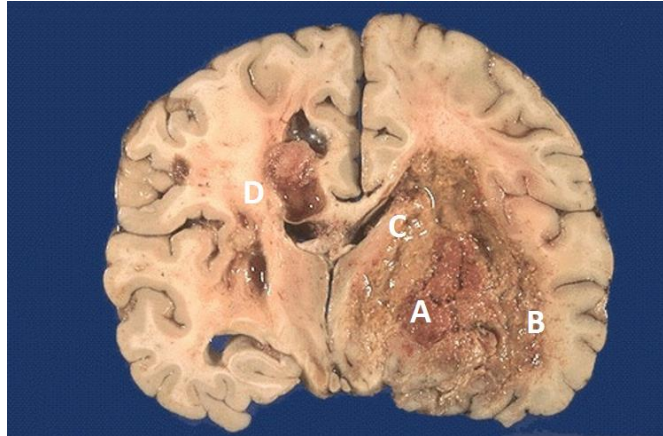


**Figure 1.3** A section of a brain in the coronal plane, affected by a glioblastoma showing the typical features represented by macroscopic examination. **A)** high vascularity/hemorrhage (hypervascularization), **B)** necrosis in the linings, **C)** excessive fluid leakage and **D)** infiltration of the opposite hemisphere affecting the basal ganglia and further spread down the temporal lobe. Modified and reprinted with permission from [19].

### 1.3 Tumor Markers, Causes and Risk Factors

The processes related to initiation and progression of glioblastomas are still poorly understood. Studies have indicated that gliomagenesis can occur in neural stem cells (NSC), precursor cells or already mature brain cells [20, 21]. NSC identified in primary brain tumors have an antigen CD133, on its cell surface [21]. This is used as a biomarker for NSC containing glioblastomas. There is to some extent a disagreement among scientist where the exact origin of glioblastoma is located. NSC positioned in the tumor are postulated to play a major role in treatment resistance [22].

The etiology of glioblastoma remains to the greatest extent unknown. Two risk factors have been entrenched: ionizing radiation exposure and genetic predisposition [23]. Therapeutic X-ray radiation has shown to increase the risk of glioma development later in life [24, 25]. Not only therapeutic radiation, but any ionizing radiation is likely to be a risk factor, including CT scan of the head, and should therefore be kept at a minimum. Mutations in genes, including tumor protein p53 (*TP53*) both inherited and induced, have been linked to an increased risk of glioblastoma development [13, 23]. The excessive use of mobile phones is

a concerning factor in relation with elevated risk of brain tumor, but no significant increase has been found. However, the long-term effect is still uncertain [26].

Glioblastoma can be defined in subgroups based on biomarkers. According to the 2016 CNS WHO classification system, glioblastoma can be divided in two groups by mutation in the *IDH1* gene (*IDH1*<sup>R132H</sup> mutation); *IDH*-wildtype glioblastoma and *IDH*-mutant glioblastoma [6] (**Table 1.1**). *IDH* is an important enzyme in cellular metabolism and especially the tricarboxylic acid cycle [27]. *IDH*-wildtype glioblastoma is by far the most common (90%), carries the poorest survival rate and arises *de novo*. *IDH*-mutant tumors develops from lower grade astrocytoma, has a better prognosis and affects younger patients [6]. These two groups often carry different genetic profiles, that might be of prognostic value [28]. Alpha thalassemia/mental retardation syndrome X-linked (*ATRX*) gene is important in histone modification and telomere length. It is along with *TP53* used as biomarkers for glioblastoma [29]. The neuropathologist uses immunohistochemistry for detection of these three markers to rule out glioblastoma from other types of glioma. Profiling of *IDH1/ATRX/TP53* has also shown to have prognostic relevance and impact on survival rate [29].

## 1.4 Cell Signaling and Genetic Alterations of Glioblastoma

The research on molecular mechanisms of glioblastoma the last years has revealed answers to several questions and probably raised an equal number of new inquiries. Cell signaling plays a key role in gliomagenesis and gene mutations may lead to altered molecular features of the glia, which in turn can promote uncontrolled cell division and tumor growth. The abnormal signaling pathways affecting glioblastoma can be divided in two broad groups: those that affect growth factor signaling, and those that alter cell cycle regulation [7]. Mutated growth factor receptors include PDGFR (platelet-derived growth factor receptor), EGFR (epidermal growth factor receptor), VEGFR (vascular endothelial growth factor receptor) and MET/HGFR (mesenchymal-epithelial transition factor/hepatocyte growth factor receptor). As for cell cycle pathway regulation, *TP53* and *RBI* (retinoblastoma) genes are of great importance, as well as cyclic dependent kinases (CDKs) and CDK-activating kinase (CAK) [7, 30] (**Figure 1.4**).

Receptor tyrosine kinases (RTK) are transmembrane receptors where many growth factors bind extracellularly and cause dimerization, leading to autophosphorylation of tyrosine residues. This leads to attraction of several intracellular proteins, generating a cascade reaction involving various cytoplasmic entities inducing a signal transduction [31]. Simplified, the receptor can be viewed as on/off buttons telling the cell to grow and divide or remain latent. Essential pathways are the PI3K/AKT/mTOR (phosphoinositide 3-kinase/protein kinase B/mechanistic target of rapamycin), Ras/Raf/MAPK (rat sarcoma/rapidly accelerated fibrosarcoma/mitogen-activated protein kinase) in addition to recruitment of the transcription factor NF- $\kappa$ B (nuclear factor kappa-light-chain-enhancer of activated B cells) (**Figure 1.4**). The oncogenic activation of these pathways by driver mutations of its encoding genes lead to abnormal cell proliferation. Mutation of such oncogenes are common feature in glioblastoma, and RTK plays a major role of its carcinogenesis [32].

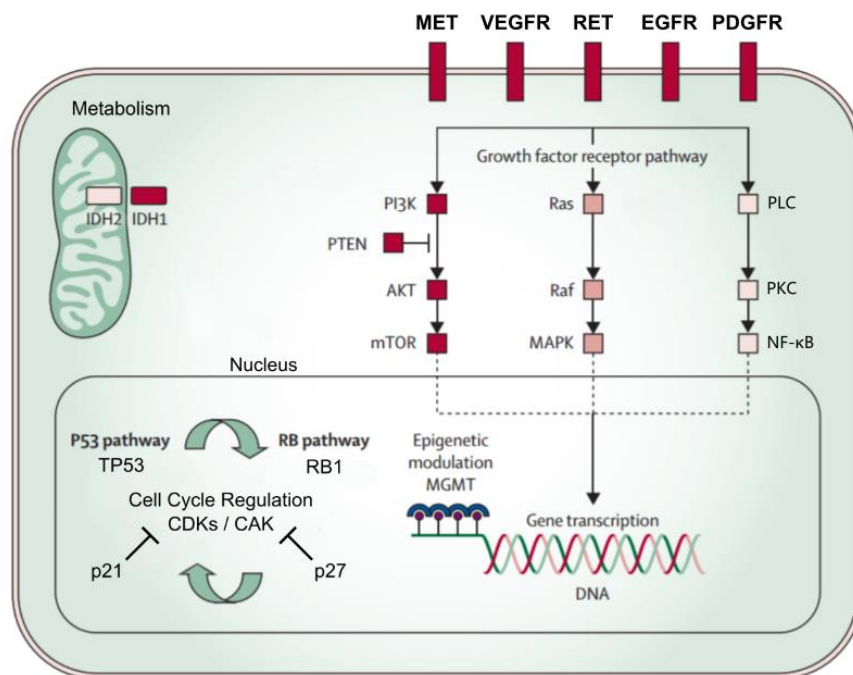


**Figure 1.4** Overview of essential components in gliomagenesis. The receptor tyrosine kinases MET, VEGFR (mostly endothelial), RET, EGFR and PDGFR activates pathways like PI3K/AKT/mTOR, Ras/Raf/MAPK, and PLC/PKC, and its encoding genes are important oncogenes in glioma development. Regulation of the cell cycle includes tumor suppressors like TP53 and RB1, along with CDKs and CAK, and p21/p27 which negatively regulates the kinases. MGMT is affected by epigenetic alterations of its promoter region. IDH1/2 are important regulators of metabolism and marker of subtypes of glioblastoma. Modified and reprinted with permission from [14].

The VEGFR is the receptor for vascular endothelial growth factor (VEGF), and is the essential inducer of angiogenesis. Three subtypes exist: VEGFR-1, -2 and -3. In the developed brain, angiogenesis is normally downregulated. Upregulation of VEGF and other angiogenic factors, in combination with oncogenic activation of VEGFR and mutations in tumor suppressor genes can activate new blood vessel formation [7, 33]. Also, the transduction mediators of the PI3K/AKT/mTOR pathway are involved in the process. When a tumor cell becomes hypoxic it upregulates hypoxia-inducible factor 1 $\alpha$  (HIF-1 $\alpha$ ), which in turn leads to secretion of VEGF [34]. An often-mutated tumor suppressor gene in glioblastoma is *PTEN* (phosphatase and tensin homologue deleted on chromosome ten) (**Figure 1.4**) [31]. Loss of PTEN leads to uncontrolled regulation of angiogenesis. This molecular pathway, and the relationship between hypoxic and normoxic tumors are essential for glioblastoma development. Other important RTK in gliomagenesis are HGFR/MET and RET. HGFR is encoded by the oncogene *MET* and engage growth, survival and migration [35]. MET and its ligand HGF are often overexpressed or co-expressed, leading to invasion and deviation of apoptosis [36]. The proto-oncogene *RET* codes for RET (REarranged during Transfection), which is shown to have a high expression rate on glioblastoma cells. This receptor is involved in the pathophysiology by promoting cell proliferation [37].

In addition to oncogenic alteration of glioblastoma, tumor suppressor genes enforce leverage on gliomagenesis. *TP53* is mutated in 81 % of *IDH*-mutant glioblastoma [6], *RBI* mutation is found in more than 20 % of high-grade gliomas [30] and is along with *PTEN* important genes in negation of gliomagenesis. TP35 and RB are also important regulators of the cell cycle, in co-operation with CDKs. CDKs are activated by cyclins (CAK) to stop the cell cycle, and inactivated again as the cell cycle progress [38]. During the cell cycle, the cell must pass these checkpoints regulated by CDKs. Cyclin D1 is essential for holding back cell cycle progression, and is found downregulated in glioblastoma [39]. This process controlled by CDKs is negatively regulated by the CDK inhibitors p21 (CDKN1A) and p27 (CDKN1B), among others [40] (**Figure 1.4**). These inhibitors prevent the cyclins from phosphorylating the CDKs, leading to withhold of the cell cycle. The functions of such regulator proteins have been found to be aberrant in glioblastoma tumors resulting in a dysregulated cell cycle [41, 42].

---

Epigenetic alterations in glioblastoma involves the *O*<sup>6</sup>-methylguanine-DNA methyltransferase (*MGMT*) and telomerase reverse transcriptase (*TERT*) genes among others [32]. Methylation of promoter regions lead to silencing of *MGMT*, has clinical implications and is found in 40% of *IDH*-wildtype glioblastoma. *MGMT* is involved in DNA repair (**Figure 1.4**). The promotor of *TERT* is mutated in over 70% of *IDH*-wildtype glioblastoma. *TERT* affects the telomeric machinery of the cell, presumably aggravating the overall survival rate [32].

## 1.5 Current and Novel Treatment Strategies

Glioblastoma is still an incurable condition. None of the treatments available can cure the disease, and tumor progression will eventually lead to patient death. Therefore, the therapy mainly aims to prolong the patient's life and curtail symptoms as much as possible. Available treatment options include surgery, radiation therapy and chemotherapy, along with medication to reduce symptoms, side effects and complications [14].

Resection of as much tumor tissue as possible through craniotomy is the preferred and most beneficial treatment method. Even a subtotal resection will most often lead to improvement of symptoms and valuable survival benefits [43]. Nevertheless, surgery is not always possible due to the tumor location, and neurological impairment after surgery may be high. Craniotomy with intraoperative awakening is now common in the clinic. Advanced anesthetic facilities make it possible for patients to stay awake during tumor removal. This is profitable since the patient's neurological status can be closely monitored and resection in decisive areas of the brain becomes less precarious [44].

Radiation therapy is another important therapeutic modality, and has been widely used for both post-surgical treatment and in cases with unresected glioblastomas [45]. It involves high frequent X-ray beams and is often carried out over a period of several weeks, giving the neoplasm multiple exposures to ionizing radiation. The main mechanism is to induce DNA damage in the cancerous cells. A standard, total dose of 60 Gy has been established as being most efficient in glioma treatment [45]. A new and upcoming treatment method is tumor treating fields (TTF). Small electric fields that interfere with cell division are emitted from a

cap on the head [46]. The therapeutic principle is fairly easy and the results so far seems promising [47].

Several therapeutic agents are in clinical use, with more or less convincing efficiency. One drug has modestly improved the treatment of glioblastoma when it was introduced in 2005. It is the alkylating agent temozolomide (TMZ) with brand name Temodal<sup>®</sup>. In combination with radiation therapy, TMZ prolonged the median survival rate of glioblastoma patient from 12.1 to 14.6 months [10, 11]. TMZ depletes the MGMT enzyme and low levels of MGMT has been associated with prolonged survival [11]. Patients with methylated promotor of *MGMT* respond better to TMZ. Cisplatin, a platinum based DNA interfering anticancer drug was previously used against glioblastoma [48]. New knowledge shows that cisplatin can decrease the activity of MGMT, and thereby possibly increase the efficiency of TMZ [49, 50]. Bevacizumab is a humanized monoclonal antibody against VEGF, with the aim to suppress angiogenesis. The drug showed remarkably good response to tumor growth, but no significance on the overall survival rate [51]. Bevacizumab is in clinically use today under the brand name Avastin<sup>®</sup>, although the overall therapeutic effect is still disputed.

## 1.6 Cabozantinib (XL 184)

Cabozantinib (1-*N*-(4-(6,7-dimethoxyquinolin-4-yloxy) phenyl)-1-*N'*-(4-fluorophenyl) cyclopropane-1,1-dicarboxamide; XL 184) is an RTK inhibitor [52]. It inhibits several tyrosine kinase receptors simultaneously, and is therefore referred to as a multiple RTK inhibitor. The drug was discovered by the company Exelixis, and the United States Food and Drug Administration (US FDA) approved cabozantinib for the treatment of advanced renal cell carcinoma (RCC) in 2015 [53]. The brand name for this drug is Cabometyx<sup>®</sup>. It is also approved for the treatment of progressive medullary thyroid cancer (MTC), under the brand name Cometriq<sup>®</sup> [54]. Cabozantinib has a molecular weight (MW) of 501.514 kDa and is a highly hydrophobic compound with a logarithmical partition coefficient (logP; solubility in a nonpolar liquid divided by solubility in a polar liquid) value of ~ 4 [55] (**Figure 1.5**).

One of the obstacles in therapeutic treatment of patients with tumors in the central nervous system is the penetration of the blood-brain barrier (BBB). The BBB is the assembly of tight junctions in the capillaries surrounding the brain and spinal cord, formed by cell adhesion

molecules [56]. Cabozantinib has been discovered in whole brain cell lysates from mice, where it was detected at 20 % of the concentration in plasma [57]. Intracranial effect of cabozantinib has been observed in one patient with brain metastasis, thus providing preliminary results of a possible BBB penetration [58]. From a chemical point of view, for an optimal CNS penetration of a drug, four criteria should be fulfilled:  $MW \leq 400$  kDa,  $\log P \leq 5$ , hydrogen bond donor (HBD)  $\leq 3$  and hydrogen bond acceptor (HBA)  $\leq 7$  [59]. As for cabozantinib, the number of hydrogen bonds are HBD = 2 and HBA = 6 (**Figure 1.5**). Thus, it satisfies all criteria except the molecular weight. Taken all these results together it is most likely that cabozantinib penetrates the BBB, at least to some extent.

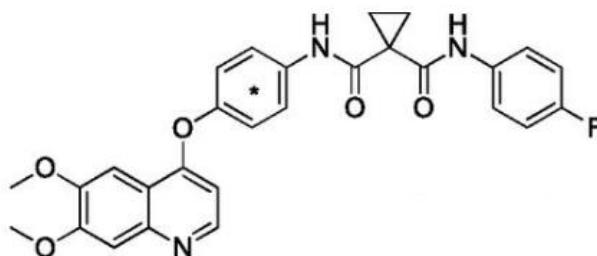


**Figure 1.5** The structural formula of cabozantinib (XL 184). The compound has a molecular weight of 501.514 kDa, and its complex ring structures implicates high hydrophobicity. \*Position of possible radiolabeling with e.g.  $^{14}\text{C}$ . Modified and reprinted with permission from [60].

The metabolism of cabozantinib has been studied in detail in healthy adults using liquid chromatography-tandem mass spectrometry [60] and radiolabeled  $^{14}\text{C}$ -cabozantinib to trace the disposition and biotransformation. The labeling takes place on the benzene ring (phenyl group) adjacent to the cyclopropane-1,1-dicarboxamide group (**Figure 1.5**). Cabozantinib is metabolized in the hepatic cytochrome P450 3A4 (CYP3A4) complex. Most of the identified metabolites were discovered in feces and some in the urine and plasma. The two most active metabolites are XL 184 desmethyl sulfate and XL 184 monohydroxy sulfate (**Figure 1.6**), thus probably carrying most of the anticancer features of the drug. The half-life ( $t_{1/2}$ ) of cabozantinib has been determined in a study to be as long as 55 hours [61]. This review also indicated good oral absorption, so does the  $\log P$  value. Cabozantinib is administered as capsules of malate salt to increase the absorption [62].

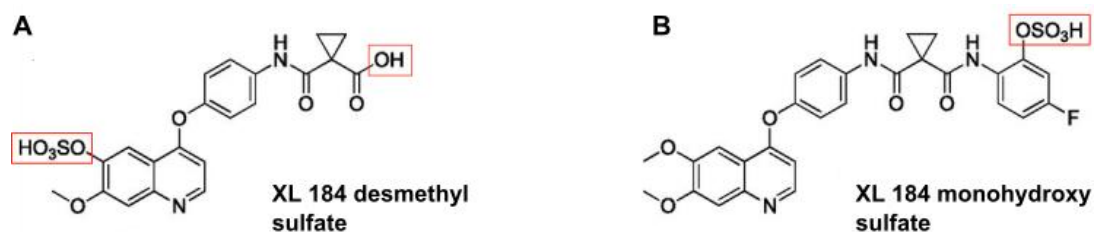


**Figure 1.6** Structure formulas of the most essential metabolites of cabozantinib (XL 184). **A)** XL 184 desmethyl sulfate. **B)** XL 184 monohydroxy sulfate. These are proposed to carry out the anticancer property of the drug. Modified and reprinted with permission from [60].

Cabozantinib simultaneously inhibits various RTKs, including MET, VEGFR-2 and RET [63, 64]. These are all receptors regulating the ability of cells to proliferate, induce angiogenesis and invade surrounding tissue. The MET receptor and its ligand HGF (hepatocyte growth factor) are found at low levels in normal developed tissues, but is upregulated during embryogenesis [65]. In many neoplasms including gliomas, dysregulation of MET and HGF is commonly found and its activation promotes cell survival, growth, and invasion [66]. HGF is also a potent angiogenic factor, and synergistic with VEGF engender angiogenesis [67]. VEGFR-2 is encoded by the *KDR* (kinase insert domain receptor) gene, and becomes phosphorylated by VEGF attachment [68]. It is shown that VEGFR-2 is a key modulator of angiogenesis in tumor cells [69]. VEGF is up-regulated in glioblastoma [70], leading to an overexpression of VEGFR-2. Instances of phosphorylated RET have also been identified in some glioblastoma tumors [71]. The ability of cabozantinib to arrest these receptors makes it a promising and future derived agent against glioblastoma. Side effects regarding use of cabozantinib has been evaluated [72]. The most common side effects reported include fatigue, nausea, vomiting, and constipation. These symptoms can be well controlled with the administration of antiemetic drugs. Serious, although very rare side effects, are severe hemorrhage, gastrointestinal perforation, and thromboembolism.

## 1.7 Experimental Background and Analytical Techniques

### 1.7.1 Cell Lines as Reflective Models of Cancer

Resected tumor tissue can be used to make cell lines by culturing tissue pieces and collect migrating cells (referred to as explant technique) [73]. This procedure preserves the biology

---

and provides reproduction of the characteristics of the neoplasm. Human cell line models are extensively used to test the potency of anticancer agents [74, 75]. *In vitro* models are beneficial in drug screening, because they are easy to work with, give rapid results and multiple analyses can be carried out within a short period. Specific conditions can be applied to mimic more closely the tumor environment *in situ*, such as supplement of extracellular matrix (ECM) proteins and culturing cells in small artificial clumps, called tumor spheroids [74, 75]. Performing molecular- and protein analysis are also readily feasible. Cell lines are excellent for evaluation of resistance development, since long-term treatment of cells can easily be carried out. If the treatment dose needs to be multiplied after some time, resistance is present. This is described using fold resistance, which is obtained dividing the dose needed for the resistance cell line by the dose for the unaffected cell line [76].

### 1.7.2 Flow Cytometry

In biomedical research, flow cytometry is a laser based technology used for cell counting, cell sorting and biomarker detection, by suspending cells in a stream of liquid (sheath fluid) and passing them one by one through a laser beam and an electronic detection apparatus (**Figure 1.7**). A sample of cells is being forced into a narrow hose leading to a flow of single cells through the instrument. Each cell is then hit by a laser generating a scatter of light from the cell [77]. The scattering light will be emitted in all directions from the cell, and collected using different detectors, which convert the light signal into an electronic, digitized signal. Forward scattered light (FSC) is detected by a detector placed on the other side of the laser beam, and give information on cell size. Side scattered light (SSC) is collected by a detector placed at an angle to the laser beam, and provide information on the granularity of the cells [77]. Cells can be stained with fluorochromes that absorb photons provided by the laser and after excitation emits light at a distinct wavelength of that particle. Filters separate the light of specific wavelength according to the desired fluorochrome and fluorescence channels (FL) obtain the signal. Dichroic mirrors guide the light to the channels [78] (**Figure 1.7**). Advanced software analyzes the data and create diagrams of the flowing cells. Multiple fluorochromes can be used simultaneously due to different emission spectra, generating polychromatic flow diagrams.

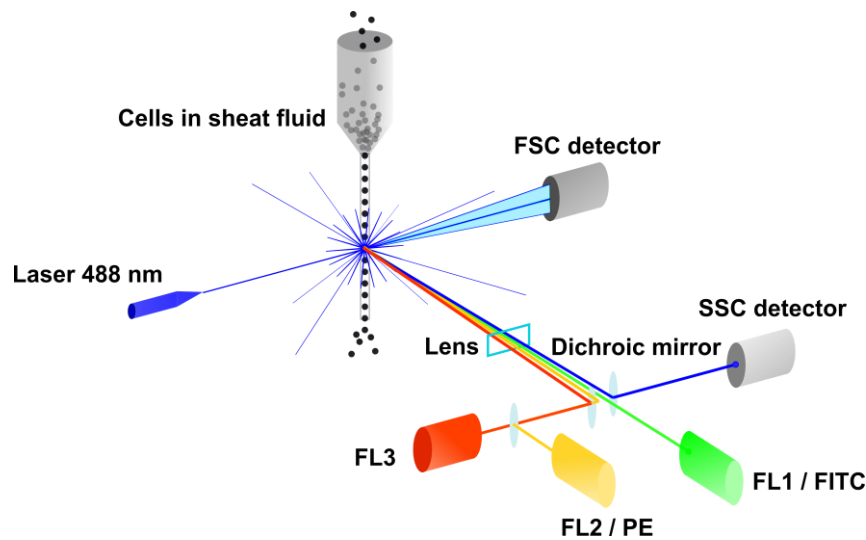


**Figure 1.7** Delineated layout of the essential part of a flow cytometer. Cells are forced pass a laser, that makes the cells scatter light and fluorescence. The fluorescent signals are detected in fluorescent channels (FL) or dye channels (e.g. PE and FITC), depending on the flow cytometer. FSC = forward scattered light, SSC = side scattered light.

Flow cytometry is commonly used to study apoptosis and cell cycle distribution. In early phase of apoptosis, the plasma membrane starts to crumble and thereby expose phosphatidylserine (PS) residues present in the wrenched membrane. Annexin V is a protein capable of specific binding to PS, and when stained with a fluorochrome can be used to quantify apoptotic events [79]. Propidium iodide (PI) is a membrane impermeable dye that binds to nucleic acids, and can be used to distinguish apoptotic cells from necrotic (dying) cells. When PI and Annexin V are used together in dual chromatic flow cytometry, a distribution of apoptosis and cell death can be obtained [79]. Since PI intercalates with DNA and the cells contain unequal amount of DNA in the different phases of the cell cycle, PI can also be used to generate a cell cycle distribution. Cells need to be fixated and permeabilized prior to analysis, as PI do not penetrate intact cell membranes [80].

### 1.7.3 Microscopy Imaging Techniques

Bright-field imaging is the most commonly used microscopy technique for *in vitro* cancer work, where normal visible light along with different objectives magnifies the specimen (**Figure 1.8**). Fluorescent microscopy is based on the same principle as for fluorescence in flow cytometry. The cells are introduced to exogenous fluorescent molecules (fluorochromes), which bind to certain components of the cell. These can be visualized at the

presence of excitatory light (usually from a UV lamp) due to fluorescence of the fluorochrome (**Figure 1.8**). Fluorescent microscopes have filters to isolate distinct sets of excitation and fluorescence emission wavelengths [81]. The technique makes it possible to detect even small details within the cell, and is commonly used in imaging of live cells [82].

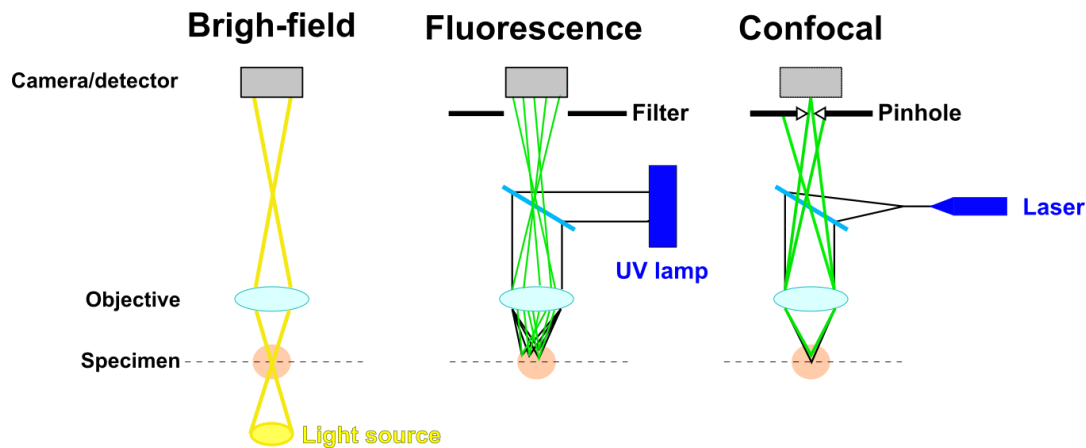


**Figure 1.8** Overview of the microscopy imaging techniques used in this thesis. Bright-field imaging uses regular light, whereas fluorescence- and confocal microscopies excite fluorochromes. Fluorescence microscopes use an UV lamp for excitation, and confocal operates with a laser. Confocal imaging is in addition done through a pinhole for high resolution images.

Trying to visualize specimen that are too thick for the light to penetrate properly, gives blurry and unfocused images. Confocal laser scanning microscopy (CLSM) solves this problem and opens the possibility to image even clusters of cells. Out-of-focus light to the image is one of the factors causing this blurriness. Confocal microscopes remove this obscuring light and gain resolution, providing clear images [83]. Rather than focusing on the entire sample, confocal microscopy focuses the laser beam onto one small spot at a time through a pinhole aperture (**Figure 1.8**). Thus, one precise piece is in conjugated focus, hence the name confocal. The microscopy technique targets distinct focal planes in the sample and scans multiple spots providing an image. This settlement improves contrast by removing light that is out-of-focus in all other planes [83]. Fluorochromes are used to stain the desired parts of the cell prior to imaging. The microscope uses laser light for excitation and the emission is detected through the pinhole. Multiple fluorochromes can be used simultaneously. Since the scanning is done in planes, it gives the opportunity to obtain images in 3D. Deconvolution of out-of-focus light back to its point source in the specimen at multiple planes are used to obtain 3D images [82]. This is also known as optical sectioning.

## 2. Aims

Glioblastoma is one of the most feared of all cancer diseases, due to its incurability and serious impact on the patient's life both physical and psychological. The need for new therapeutic agents is urgent, and finding out more about this disease and possible treatment opportunities is therefore of great importance. The Translation Cancer Research Laboratory at the University of Bergen are performing all-encompassing research on brain tumors, to validate effectiveness of agents for clinical use and learning more about the biology of such tumors. The main aim of this thesis is to find out if the receptor tyrosine kinase inhibitor cabozantinib is effective on glioblastoma cell lines and ascertain its possible mechanisms of action. Several *in vitro* techniques will be performed, such as viability testing, three-dimensional models, flow cytometry and advanced imaging applications. By carrying out these procedures, we will provide more knowledge on the cell signaling and molecular alterations by which cabozantinib is targeted against.

Six sub aims have been assessed for this thesis:

1. Certify the effect of cabozantinib on monolayer of cells using viability- and proliferation assay.
2. Use flow cytometry to reveal how the drug affects cell cycle and apoptosis.
3. Find out if cabozantinib interferes with the mitochondrial membrane potential.
4. Study tumor spheroids after drug treatment related to tumor growth and migration.
5. Use western blot to obtain information on cell surface receptors and intracellular proteins after treatment.
6. Verify if glioblastoma cells gain resistance to cabozantinib.

## 3. Materials and Methods

### 3.1 Cell Lines

In this thesis, four different glioma cell lines were used: A172, U-87 MG (Uppsala 87 Malignant Glioma), U-251 MG (Uppsala 251 Malignant Glioma) and GaMG (Gade Malignant Glioma). All cell lines were derived from astrocytoma WHO grade IV (glioblastoma) tumors, and have been commonly used in previous studies. A172 was derived from a 53 year old male, and was established using explant technique [84]. The cell line exhibits many glioblastoma characteristics and is still extensively included in drug testing experiments [85]. U-87 MG is probably the most frequently used cell line in glioblastoma research. The original tumor of origin was from a 44 year old male [86], but recent investigation states that the commercial available U-87 MG cell line is different from the initial tumor [87]. U-251 MG is along with U-87 MG established at the University of Uppsala, hence its abbreviation [88]. The source of origin for U-251 MG was a 75 year old male, with a tumor in the parietal lobe [89]. There are several subclones with different characteristics of this cell line available, but genetic analysis has confirmed that the cell line used in this project reflects a glioblastoma tumor [90]. GaMG is from a 42 year old female with histologically defined glioblastoma tumor. Primary cultures from the tumor biopsies were obtained using explant technique. The cell line have a near triploid chromosome content [91]. Mutations in the *TP53* and *PTEN* genes have been accessed for all cell lines. *TP53* is mutated in all cell lines except U-87 MG, and *PTEN* in all cell lines except GaMG [92-94]. In addition, *CDKN2A* (p14<sup>ARF</sup>/p16) is reported mutated in A172 and U-87 MG, and *CDKN2C* (p18) in U-87 MG [95]. GaMG was established at the Department of Pathology, The Gade Institute, Haukeland University Hospital. A172, U-87 MG and U-251 were purchased from the American Tissue Culture Collection (ATCC; Manassas, VA, USA).

### 3.2 General Cell Culture Techniques

All cell culture work was performed under sterile conditions, in a biosafety cabinet (BSC) with laminar air flow. The surface of the cabinet and everything placed inside was sterilized

using 70% ethanol. Culture flasks used were EasYFLask™ T25 (25 cm<sup>2</sup>), T75 (75 cm<sup>2</sup>) and T175 (175 cm<sup>2</sup>) (Thermo Scientific, Nunc, Roskilde, Denmark). Unless otherwise specified, the growth medium was DMEM ALT consisting of: 450 mL Dulbecco's Modified Eagles Medium (DMEM; Sigma-Aldrich Inc., St. Louis, MO, USA), 50 mL heat inactivated fetal bovine serum (FBS; Life Technologies, Gibco™, Bleiswijk, Netherlands), 16 mL non-essential amino acids 100× (BioWhittaker™, Verviers, Belgium), 10 mL L-glutamine – 200 nM (BioWhittaker™), 10 mL penicillin/streptomycin (PEN-STREP) – 100 µL/mL (BioWhittaker™) and 0.1 mL Plasmocin™ – 25 mg/mL (InvivoGen, San Diego, CA, USA). Phosphate-buffered saline (PBS) was prepared at a 1× concentration using a custom 10× Dulbecco's phosphate-buffered saline (Sigma-Aldrich Inc.) diluted in autoclaved MilliQ water. To detach the cells, 0.25 % trypsin-EDTA (BioWhittaker™) was used unless otherwise stated. Sterile Corning® Costar® Stripette serological pipettes and Corning® Centrifugation Tubes (Sigma-Aldrich Inc.) was used for fluid transfer. For smaller volumes, autoclaved Eppendorf Tubes® (Eppendorf, Hamburg, Germany) was used. Incubation properties were 37°C, 5 % CO<sub>2</sub> and 100 % humidity.

### **3.2.1 Thawing**

About 20 min before the thawing process, a T25 flask filled with 6 mL DMEM ALT growth medium was preheated in the incubator. A sample of the desired cell line was taken out of the vapor phase of liquid nitrogen (VPLN) in the N<sub>2</sub> tank, and put on dry ice for transportation to minimize slow-thawing of cells. The vial was as soon as possible put in a 37°C water bath. When the solution had completely melted, it was centrifugated at 900 rpm for 4 min. The supernatant containing special freezing chemicals was discarded, and the cell pellet resuspended in 4 mL DMEM ALT growth medium. The cell suspension was then transferred into the preheated T25 flask, so that the total volume was 10 mL. Passage number and date of thawing was marked on the flask, and it was put into the incubator for growing.

### **3.2.2 Passaging**

Cells were routinely passaged when they reached 70-90 % confluency. Growth medium was discarded, and cells washed twice with PBS, about 0.5 mL / 10 cm<sup>2</sup> cell surface. Trypsin-EDTA was added in a volume corresponding to 0.2 mL / 10 cm<sup>2</sup>, and the flask was set into the incubator a few minutes for the cells to detach. When the cells were loose, an amount of

---

growth medium corresponding to the volume of trypsin or higher was added to neutralize the enzymatic reaction. The cell suspension was resuspended several times to obtain a single cell solution. A desired amount of cell solution was then transferred into a pre-heated culture flask containing a suitable amount of DMEM ALT, 10-15 mL for a T75 flask and 25-30 mL for a T175 flask. When the cells had been passaged ten times, they were discarded and a new batch of cells was taken from the liquid nitrogen storage and into culture.

### **3.2.3 Cryopreservation**

For preservation of cells, they were frozen down in the VPLN. A fully confluent T175 flask of cells was washed and trypsinized as explained in the previous section. The single cell suspension was transferred to a centrifugation tube and spun down at 900 rpm for 4 min. Meanwhile, a freezing solution consisting of 4 mL DMEM ALT, 0.5 mL FBS and 0.5 mL dimethyl sulfoxide (DMSO; Sigma-Aldrich Inc.) was prepared. The growth medium was discarded and the freezing solution was added to the cell pellet and resuspended well. The solution was aliquoted in 1 mL aliquots into CryoTube™ Vials (Thermo Scientific, Denmark). The vials were placed in a pre-cooled Nalgene Mr. Frosty™ Freezing Container (Thermo Scientific, Rockford, IL, USA) with isopropanol and placed at -80°C for 24 hours. The freeze container ensures a cooling rate by -1°C per minute so that the viability of the cells is maintained. After 24 hours, the vials were transported on dry ice to the liquid nitrogen tank and placed in the VPLN for long-term storage.

## **3.3 Experimental Groundwork**

### **3.3.1 Mycoplasma Testing**

Before cryopreservation of the cells, all cell lines were inspected for contaminants. The cells were closely examined under the microscope to detect large impurities. To exclude the possibility of mycoplasma contamination, a mycoplasma test was carried out using MycoAlert™ PLUS Mycoplasma Detection Kit (Lonza Walkersville Inc., Walkersville, MD, USA). At least 48 hours prior to testing, the normal DMEM ALT growth medium was discarded and DMEM without plasmocin was added to the flask. After 2 days of growing, 2 mL supernatant was removed and centrifugated at 1500 rpm for 5 min to removed possible

dead cells. 100  $\mu$ L of cleared supernatant was tested following the protocol provided by Lonza Walkersville [96].

### 3.3.2 Cell Counting

For obtaining an accurate cell number, a Countess<sup>TM</sup> Automated Cell Counter (Invitrogen, Carlsbad, CA, USA) was used. 10  $\mu$ L of the cell suspension was combined with 10  $\mu$ L 0.4 % Trypan Blue Stain (Life Technologies, Eugene, OR, USA) and mixed well by pipetting. The solution was added to each side of a Countess<sup>®</sup> Cell Counting Chamber Slide (Invitrogen). The slide was inserted into the counting machine, and counting was performed following the provided manual [97].

### 3.3.3 Drug Preparation

The drug used in this study was XL 184 (free base) CABOZANTINIB in powder form, provided by ChemiTek. CAS No: 1140909-48-3 (ChemiTek, Indianapolis, IN, USA). The drug was dissolved in DMSO to prepare a 200 mM stock solution. The solution was retained at -20°C and was stable under such conditions for several months [98]. To make the desired concentration of drug, the stock solution was diluted in DMEM ALT and heated to 37°C in a water bath before added to the cells.

## 3.4 Monolayer Viability Experiments

### 3.4.1 Resazurin Assay

$3 \times 10^3$  cells were seeded into a 96-well plate (Thermo Scientific, Denmark), in a volume of 100  $\mu$ L growth medium. Three plates per cell line were used. The cells were allowed to attach during 24 hours and thereafter treated with 100  $\mu$ L of cabozantinib in DMEM ALT in a 10-fold dilution series (100-10-1  $\mu$ M, 100-10-1 nM, 100-10-1 pM; One column per dose). One control column with DMEM ALT and cells was included as non-treated control. Wells with only DMEM ALT was also included to collect background from the growth medium (**Figure 3.1**). The cells were incubated with drug for 72 hours. After this period, a 0.1 mg/mL solution of resazurin sodium salt (Sigma-Aldrich Inc.) diluted in PBS was prepared,

and added to the cells in 10 % of the volume of the wells. Resazurin is a blue dye that viable cells reduces to resorufin, a pink compound [99]. After 4 hours of incubation, the growth medium had changed color, and the absorbance at dual wavelength 560/590 nm was detected using VICTOR<sup>3</sup> 1420 Multilabel Plate Counter (Perkin Elmer, Waltham, MA, USA) and WorkOut 2.0 (Dazdaq Ltd., Brighton, England) scanning software. Additional plates with DMSO content corresponding to the DMSO present in the drug samples were also set up and analyzed.

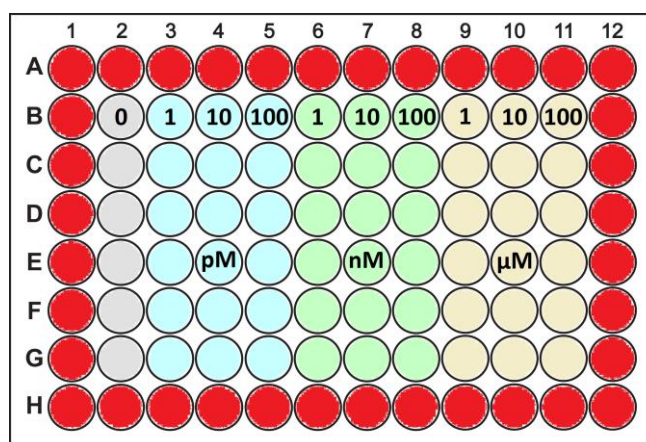


**Figure 3.1** Template of the 96-well plate used in the monolayer viability assay. Red = only DMEM ALT, grey = cells in DMEM ALT, blue = cabozantinib in pM, green = cabozantinib in nM and yellow = cabozantinib in μM. See main text for more details.

### 3.4.2 Obtaining IC Doses

Based on the viability results from the resazurin assay, the half maximum inhibitory concentration ( $IC_{50}$ ) was acquired. This is the dose of cabozantinib that is required for 50 % inhibition of the cells, making them non-viable *in vitro*. With the aid of the dose-response curve, one can use nonlinear regression and the derivative to obtain the hill slope of the curve in the  $IC_{50}$ -point. This can be used to calculate other IC doses (**Figure 3.2**).  $IC_{25}$ ,  $IC_{50}$  and  $IC_{90}$  obtained were used throughout the experiments of this thesis.

$$IC_X = \left( \frac{100 - X}{X} \right)^{\frac{1}{Hill\ slope}} \times IC_{50}$$

**Figure 3.2** Formula for calculating  $IC_{anything}$  from  $IC_{50}$  and the hill slope obtained from the drug-response curve. Modified and reprinted with permission from [100].

### 3.4.3 Imaging – Bright-field and LIVE/DEAD® Fluorescence

A 96-well plate was prepared as described in chapter 3.4.1, but treated with the IC<sub>25</sub>, IC<sub>50</sub> or IC<sub>90</sub> doses, two rows per treatment (no resazurin was added). Two rows received only growth medium, and two rows were used for DMSO control. The LIVE/DEAD® Viability/Cytotoxicity Kit (Molecular Probes Inc., Eugene, OR, USA) was used to obtain fluorescent images of the monolayer cell viability. Live cells are stained with calcein AM and emits green fluorescence whereas EthD-1 (ethidium homodimer-1) penetrates dead cells and emits red fluorescence. The kit was set up according to the protocol provided with the kit [101]. Half of the wells were left unstained for bright-field imaging. Images were obtained using Nikon Eclipse TE2000 Inverted Microscope (Nikon Instruments Inc., Melville, NY, USA) with a 10× objective. For fluorescent images FITC- (green) and TRITC (red) filters were used.

## 3.5 Cell Tumorigenicity – Clonogenic Assay

The procedure is also referred to as the colony forming assay. It is a three-step process that involves treatment of cells, plating of a defined number of cells after treatment and finally fixation and staining of colonies. In a 12-well plate (Thermo Scientific, Denmark), 1 mL of cell suspension containing  $1.5 \times 10^4$  cells were seeded into each well, (one plate per cell line). When the cells reached 80-90 % confluency (24-48 hours), the growth medium was discarded and cells treated in triplicates with the IC<sub>25</sub>, IC<sub>50</sub> or IC<sub>90</sub> doses. 1 mL DMEM ALT was added to three wells as control. The plate was then incubated for 72 hours. After the treatment period, growth medium was removed and the cells carefully washed twice with 0.5 mL PBS. Trypsination using 500 µL trypsin-EDTA in each well was then performed, followed by addition of 1 mL DMEM ALT to stop the detachment of the cells. Each well of cells were resuspended to produce a single cell suspension and transferred to a tube. The tube was centrifugated at 900 rpm for 4 min to obtain a cell pellet. The growth medium containing trypsin was removed and 1.5 mL fresh DMEM ALT was added. The tubes were now kept on ice. One random chosen tube for each triplicate was used for cell counting. We assume that the cell numbers in all the triplicates are approximately the same. Each of the 12 samples was then diluted with growth medium to produce solutions containing  $1 \times 10^4$  and  $5 \times 10^4$  cells per milliliter. In four 6-well plates (Thermo Scientific, Denmark) 1 mL DMEM

---

ALT were added to each well. 100  $\mu$ L of the cell solution from the individual tubes were then transferred into its corresponding well in the 6-well plates to attain  $1 \times 10^3$  and  $5 \times 10^3$  cells. The cells were thoroughly resuspended by pipetting and observed under the microscope to verify the low number of cells. The plates were then incubated for 7 days to form colonies. On the final day, the growth medium was removed and the cells washed with 1 mL PBS. The colonies were fixed using 1 mL 4 % paraformaldehyde (PFA; 16 % diluted in PBS) (Thermo Scientific, USA) and incubated for 30 min. After fixation, the colonies were stained using a crystal violet solution (0.5 % crystal violet (Sigma-Aldrich Inc.) and 6 % glutaraldehyde (Merck Millipore, Darmstadt, Germany)) and incubated at room temperature (RT) for 5-10 min. Crystal violet staining were removed, followed by a double wash with PBS. The plates were left in the biosafety cabinet for a few min to dry up, and the colonies were counted.

### 3.6 Cell Cycle Analysis

Flow cytometry was used to analyze the DNA content within the cells after treatment with cabozantinib.  $1.8 \times 10^5$  cells in 3 mL medium were seeded in a 6-well plate and incubated for 24 hours, for the cells to attach to the wells. After incubation, growth medium was aspirated and 1.5 mL drug in triplicates corresponding to IC<sub>25</sub>, IC<sub>50</sub> or IC<sub>90</sub> doses were added. Fresh DMEM ALT was used for three control wells. The cells were incubated with cabozantinib for 72 hours. A regular trypsination with 0.5 mL trypsin and 1 mL growth medium for neutralizing was used to harvest the cells from the wells. The cell solutions were transferred to a tube and constantly kept on ice from this step. Tubes were centrifugated in a cooling centrifuge at 4°C, 900 rpm for 5 min and supernatant was removed. 3 mL ice-cold absolute ( $\geq 99.8$ ) ethanol (VWR Chemicals, Fontenay-sous-Bois, France) was added dropwise to the pellet while vortexing to fixate the cells. Tubes were then kept in the fridge for a minimum of 24 hours for complete fixation. After fixation, the cells could be kept in the fridge for many weeks. Before analysis by flow cytometry, the samples were centrifugated at 4°C, 900 rpm for 5 min. The ethanol was removed, and cells washed using 1 mL of PBS followed by one additional centrifugation. The PBS was discarded and 50  $\mu$ L 1 mg/mL Ribonuclease A (RNase A from bovine pancreas; 50 mg/mL diluted in PBS) (Sigma-Aldrich Inc.) was added to the samples. Staining of the DNA was done resuspending the cells with 150  $\mu$ L propidium iodide, (PI; 50  $\mu$ g/mL in PBS) (Sigma-Aldrich Inc.). The samples were incubated at RT for

20 min away from light. After the incubation period, the samples were put back on ice and analyzed as soon as possible using an Accuri™ C6 flow cytometer (Accuri Cytometers Inc., Ann Arbor, MI, USA). Before putting the tubes on the cytometer, they were mixed by vortexing. Doublets that can interfere with the results, was removed by gating on FL2-H vs. FL2-A. Cell counting was stopped when  $1 \times 10^4$  cells were reached inside the gate. Detection in FL2-A was plotted against cell count to obtain a cell cycle histogram. The results were analyzed using FlowJo software (Tree Star Inc., Ashland, OR, USA) (**Figure 3.3**).

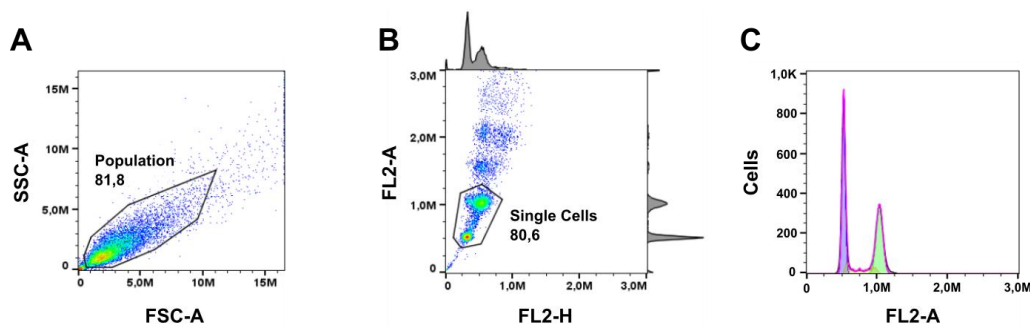


**Figure 3.3** Gating and analysis in FlowJo for the cell cycle analysis. **A)** Gating in FSC-A vs. SSC-A to remove the debris and doublets, and define the population. **B)** Gating in FL2-H vs. FL2-A to identify the single cells for the analysis, and remove more debris and doublets. The adjacent histograms show the cell counts that makes up the flow chart. **C)** The final diagram after analysis.

### 3.7 Apoptosis Assay

A flow cytometry analysis was performed to study apoptosis.  $5 \times 10^4$  cells in 1.5 mL growth medium were plated out in a 6-well plate. The cells were incubated until they reached 70-80 % confluency (about 2-3 days). They were then treated with cabozantinib doses of IC<sub>25</sub>, IC<sub>50</sub> or IC<sub>90</sub> in triplicates. Three wells containing only DMEM ALT were used as negative controls. The plates were incubated for 72 hours. Meanwhile, annexin-binding buffer was prepared: 0.1 M HEPES (Sigma-Aldrich Inc.), 1.4 M NaCl (Sigma-Aldrich Inc.) and 25 mM CaCl<sub>2</sub> (Merck Millipore) in 0.5 L MilliQ water. The pH was adjusted to 7.4 using 10 mM NaOH (Sigma-Aldrich Inc.), and the buffer stored in the fridge. After incubation of the cells with drug, the growth medium was removed and transferred to a centrifugation tube, to collect the floating apoptotic cells. The adherent cells were washed twice with 1 mL PSB and 0.5 mL trypsin-EDTA was added. After 2-3 min, 1 mL DMEM ALT was added to stop the enzymatic reaction. The cells were resuspended to obtain a single cell solution and transferred to the same tube, and spun down at 900 rpm for 4 min and the supernatant was

discarded. The cell pellet was resuspended in 50  $\mu\text{L}$  annexin-binding buffer, 0.5  $\mu\text{L}$  50  $\mu\text{g}/\text{mL}$  PI and 2  $\mu\text{L}$  Annexin V Alexa Flour<sup>®</sup> 488 conjugate (Molecular Probes Inc.) were added to each sample. One control was not stained and received only 50  $\mu\text{L}$  annexin-binding buffer, as a negative control. Samples were incubated at RT, away from light for 15-30 min. After incubation, the samples were put on ice and 200  $\mu\text{L}$  annexin-binding buffer was added to each tube. The cell solution was transferred to Falcon<sup>®</sup> 5 mL Round-Bottom tubes (Corning Science México, Tamaulipas, Mexico C.P) and analyzed by a BD LSRFortessa<sup>™</sup> cell analyzer (BD Bioscience, San Jose, CA, USA). The unstained sample was used to set parameters of the flow cytometer. Debris was gated out at FCS vs SCC. Blue 488 nm laser light was used, and fluorescence in the FITC-A and PE-A channels was detected. The results were analyzed using FlowJo software (**Figure 3.4**).

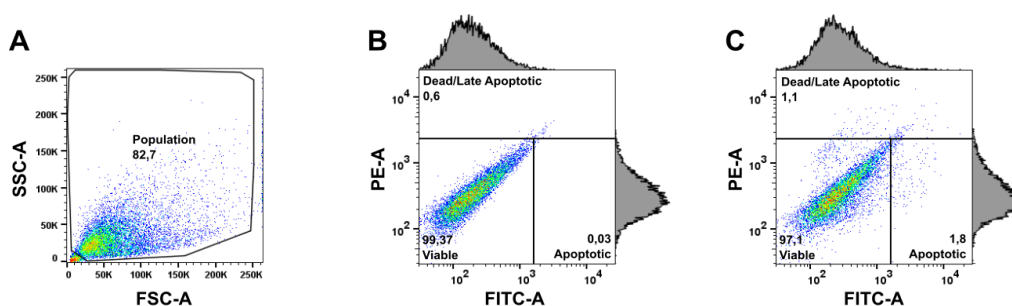


**Figure 3.4** Gating and analysis in FlowJo for the apoptosis assay. **A)** Gating in FSC-A vs. SSC-A to remove debris and define the population. **B)** Gating in FITC-A vs. PE-A of the unstained sample, and defining the populations. The adjacent histograms show the cell counts that makes up the flow chart. **C)** Applying the gating of the unstained sample to the untreated.

### 3.8 Mitochondrial Membrane Potential

$1.5 \times 10^3$  cells were seeded in a 96-well plate and incubated for 24 hours. Cells were then treated with cabozantinib corresponding to  $\text{IC}_{25}$ ,  $\text{IC}_{50}$  or  $\text{IC}_{90}$  (three wells per treatment). DMSO controls and positive controls with only DMEM ALT were also included. The cells were incubated with drug for 72 hours. A Mitochondria Staining Kit with JC-1 dye (Sigma-Aldrich Inc.) was used to measure the mitochondrial membrane status. The assay used a cationic fluorescent dye, JC-1 which aggregates (J-aggregated) in energized mitochondria and emits red fluorescence. When the mitochondrial gradient ( $\Delta\psi$ ) gets disrupted, the JC-1 monomer dominates and the fluorescence shifts to green. The assay was set up according to the technical bulletin [102] provided in the kit with following modifications: 40  $\mu\text{L}$  of staining solution was added to each well and the incubation period was 25 min. For positive

controls, 0.5  $\mu$ L 1 mg/mL valinomycin (Sigma-Aldrich Inc.) which disrupts the mitochondrial membrane was added to the staining solution. As the JC-1 fluorescence rapidly diminishes in the excited state, different plates were used for fluorometry and imaging.

### **3.8.1 Fluorimetric Quantification**

The plate was scanned using a VICTOR<sup>3</sup> Perkin Elmer 1420 Multilabel Plate Counter with excitation at 525 nm and emission at 590 nm for the J-aggregates (red), and excitation at 490 nm and emission at 530 nm for the JC-1 monomers (green). The measurement was done using WorkOut 2.0 scanning program.

### **3.8.2 Imaging**

For the fluorescent imaging, the plate was prepared as described previously, but the incubation with dye was stopped after 10 min. 60  $\mu$ L of 10 mg/mL Hoechst 33342 (Molecular Probes Inc.) diluted 1:2000 in PBS was added to each well and the plate further incubated for 15 min. Images were obtained using Nikon Eclipse TE-2000 microscope with DAPI- (blue), FITC- (green) and TRITC (red) filters.

## **3.9 Growth Inhibition of Tumor Spheroids**

A special 96-well Corning<sup>®</sup> Costar<sup>®</sup> Ultra-Low attachment plate (Sigma-Aldrich Inc.) was applied to generate tumor spheroids. The outer boundary wells were filled with 100  $\mu$ L DMEM ALT and the rest of the plate was divided into 4 squares, one for each cell line and filled with 100  $\mu$ L cell suspensions of the corresponding cell line containing  $5 \times 10^3$  cells. The plate was centrifugated at 900 g for 15 min and incubated for 5 days in order to form spheroids. After the incubation period, drugs corresponding to IC<sub>25</sub>, IC<sub>50</sub> or IC<sub>90</sub> doses were prepared. A DMSO control with the concentration reciprocal to the content of the IC<sub>90</sub> dose (0.05 %) was also prepared. The spheroids were now treated in triplicates with DMEM ALT as untreated, the three drug doses and 0.05 % DMSO, in volumes of 100  $\mu$ L which gives a total volume of 200  $\mu$ L and uniform concentration of drugs. On the same day as the start of treatment, images of the spheroids were taken on Nikon Eclipse TE2000 microscope with a

---

4× objective. The diameter was measured along the longest and shortest axes of the spheroid. For the next 21 days, the plate was kept in the incubator and the image- and measure process on Nikon Eclipse TE 2000 carried out every 7<sup>th</sup> day. The plate was inspected every 3<sup>rd</sup> day, and regularly during the culturing course some of the growth medium, drug- and DMSO solutions were replaced to avoid relinquish of nutrients.

### 3.10 Migration Assay

Tumor spheroids were made using a 96-well Corning<sup>®</sup> Costar<sup>®</sup> Ultra-Low attachment plate as described above. Solid spheroids were formed over a period of 7 days in the incubator. The spheroids were then transferred to a 12-well plate with the aid of a regular pipette set to 200 µL to generate enough suction force to disengage the spheroid from its corning well. For each spheroid, two orthogonal diameters were measured using a graded eyepiece graticule (100 index) inserted into the ocular of a regular inverted light microscope. Then, DMEM ALT or drug doses corresponding to IC<sub>25</sub>, IC<sub>50</sub> or IC<sub>90</sub> were added in a volume of 600 µL. Three spheroids for untreated controls, and three per treatment. To align the spheroids in the middle of the plate, bubbles were removed using a sterile cannula and the plate given a light swirl. The plate was then warily placed in the incubator for the spheroid to attach to the plate and cells start to migrate out of the spheroid. Measurements using the graticule were done on day 0 (before adding of the drug), day 2 and day 4 after the start of the migration. On the final day, images using Nikon Eclipse TE-2000 were taken to visualize the spread of tumor cells. For the U-87 MG cell line, pre-coating of the 12-well plate was necessary for the spheroids to adhere to the well. Collagen Type I (EMD Millipore, Temecula, CA, USA) 5.5 µg/mL in PBS was added to the plate in a volume of 200 µL and incubated at RT for 30 min. Excess collagen I was removed followed by a double wash with PBS and the plate allowed to air dry. Spheroids were then transferred and treated as described previously.

### 3.11 CLSM Evaluation of Tumor Spheroids

The GaMG cell line was chosen for the experiment due to its favorable spheroid formation capability and round shape.  $4 \times 10^3$  cells were seeded in a 96-well Corning<sup>®</sup> Costar<sup>®</sup> Ultra-Low attachment plate, volume 100 µL. The plate was centrifugated at 900 g for 15 min, and

incubated for 7 days for spheroid to form. When solid spheroids had formed, three spheroids were treated with their IC<sub>50</sub> dose of cabozantinib, in 100 µL growth medium. Three spheroids received 100 µL DMEM ALT as untreated controls. The spheroids were incubated with drug for 72 hours. The LIVE/DEAD® Viability/Cytotoxicity Kit was used according to the protocol provided [101] with addition directly in the wells and extended incubation period with the fluorochromes for 1.5 hours. The spheroids were transferred from the plate to a Lab-Tek™ II Chambered Coverglass (Thermo Scientific, USA) filled with PBS. Images of the spheroids were obtained using Leica TCS SP8 STED Confocal Scanning Microscope (Leica Microsystems, Wetzlar, Germany). The calcein AM (live) was detected in the green channel, and EthD-1 (dead) in the red channel. Objective used was HC PL APO CS2 20× with an immersion of 0.75. Pinhole was set to 56.6 µm.

## **3.12 Protein Analysis – Western Blot**

### **3.12.1 Cell Lysate Preparation**

A fresh batch of cells from the VPLN was thawed and directly divided into two T75 flasks with 12 mL DMEM ALT. The cells were incubated until they reached 70 % confluency. The growth medium was discarded and 10 mL IC<sub>50</sub> dose of cabozantinib added to one flask and 10 mL DMEM ALT to the other as control, followed by an incubation period of 72 hours. If the control flask reached 100 % confluency prior to 72 hours, the cell lysate was collected at this point. The cells were washed with 4 mL PBS, and 5 mL ice-cold PBS was added to the flask. With the aid of a cell scraper (TPP AG, Transadingen, Switzerland) the cells were detached from the flask. The cell solution was thoroughly suspended several times and transferred to a pre-cooled tube and spun down at 900 rpm for 4 min. The tube was kept on ice the entire time from now on. The PBS was discarded and 15 µL 10× cOmplete™ Mini Protease Inhibitor (Roche Diagnostics GmbH, Mannheim, Germany) and 15 µL 10× PhosSTOP EASYpack (Roche Diagnostics GmbH), both diluted in MilliQ-H<sub>2</sub>O added to the cell pellet. 150 µL ice-cold Lysis Buffer 17 (R&D Systems Inc., Minneapolis, MN, USA) was finally added and the pellet resuspended. The cell solution was incubated on ice for 15 min and vortexed once during this period, followed by sonication for 1 min at 30 amplitudes. The lysate solution was transferred to a pre-cooled 1.5 mL Eppendorf tube and centrifugated

---

at 4°C, 14 000 rpm for 20 min. Supernatant was collected, aliquoted in 0.5 mL Eppendorf tubes and frozen at -80°C.

### 3.12.2 Estimation of Protein Content – BCA Assay

A standard protein solution was prepared with bovine serum albumin (BSA; Sigma-Aldrich Inc.) dissolved in Lysis Buffer 17 at a concentration of 10 µg/µL, and sterile filtered (0.2 µM filter). This was diluted to make a dilution series of several known BSA concentrations. Pierce BCA Protein Assay Kit (Thermo Scientific, USA) was used for the protein analysis. Bicinchoninic acid (BCA) makes a color change in the presence of proteins. The two components of the kit were combined and pipetted into a 96-well plate. In triplicates, 2 µL of the known BSA concentrations, and cell lysates was added to the wells. Negative controls using 2 µL MilliQ-H<sub>2</sub>O was also included. The plate was incubated at 37°C in the dark for 30 min and scanned on Multiskan<sup>TM</sup> FC Microplate Photometer (Thermo Scientific, USA) at 560 nm. The optical density values of the BSA samples was used to make a standard series, and with linear regression the protein concentrations of the cell lysates were obtained.

### 3.12.3 Western Blot

Western blot was performed by separating the proteins of the cell lysates using electrophoresis, transferring them to a membrane and detect the specific protein using antibodies (immunoblotting). The electrophoresis- and blotting system used was NuPage<sup>®</sup> (Invitrogen), following the NuPage<sup>®</sup> protocol [103]. For a more in-depth description than provided here see [104] and the protocol. All products used, unless otherwise stated was from Invitrogen. For each sample, 35 µg protein (based on the BCA assay) was reduced using NuPage<sup>®</sup> Sample Reducing Agent and heated at 70°C for 10 min and mixed with NuPage<sup>®</sup> LDS Sample Buffer as loading dye. Gel used was NuPage<sup>®</sup> 4-12% Bis-Tris 1.0 mm 10 wells, accompanied by NuPage<sup>®</sup> MOPS SDS Running Buffer. 2.5 % NuPage<sup>®</sup> Antioxidant was added to the running buffer. SeeBlue<sup>®</sup> Plus2 Pre-stained Protein Standard served as a guiding ladder. Electrophoresis was carried out at 60 V for 5-10 min and then approximately 90 min at 120 V. The proteins were transferred from the gel to Amersham Protan Premium 0.2 µm Nitrocellulose Membrane (GE Healthcare, Life Sciences, Germany), using wet-transfer in transfer buffer (NuPage<sup>®</sup> Transfer Buffer, 10 % methanol (Sigma-

Aldrich Inc.), and 1% NuPage<sup>®</sup> Antioxidant). Transfer was performed at constant 35 V for 120 min.

10× Tris-buffered saline (TBS) was prepared with 200 mM Tris-Base (Sigma-Aldrich Inc.) and 1.5 M NaCl, pH adjusted to 7.6 using 6 M hydrochloric acid (Sigma-Aldrich Inc.). This solution was again used to make TBS-Tween (TBST), with 10 % 10× TBS, 0.1 % Tween<sup>®</sup> 20 (Sigma-Aldrich Inc.). After transfer, the membrane was blocked in blocking solution (5% BD Difco<sup>™</sup> Skim Milk (Becton, Dickinson and Company, Sparks, MD, USA) dissolved in TBST) for 60 min under agitation at RT.

When the blocking of the membrane was completed, primary antibodies of interest was diluted in 5 % skim milk blocking solution and added to the membrane. Incubation with primary antibody was carried out over-night under agitation at 4°C. Primary antibodies used in this thesis were: Phospho-c-Met (Tyr1230, Tyr1234, Tyr1235) #44-888G (diluted 1:1000) (Invitrogen), Phospho-VEGF Receptor 2 (Tyr 951) (7H11) #2476 (diluted 1:1000), Phospho-mTOR (Ser2448) (49F9) #2976 (diluted 1:1000) and Phospho-Akt (Ser473) #9271 (diluted 1:1000) from (Cell Signaling Technology, Boston, MA, USA), HIF-1 $\alpha$  (28b): sc-13515 (diluted 1:500), PI 3-kinase p101 (I-18): sc-130230 (diluted 1:500), Akt1 (7): sc-135829 (diluted 1:500), PTEN (A2B1): sc-7974 (diluted 1:1000), GAPDH (0411): sc-47724 (diluted 1:1000), p27 (F-8): sc-1641 (diluted 1:500), p21 (F-5): sc-6246 (diluted 1:500) and cytochrome c (2G8): sc-65396 (diluted 1:500), all from (Santa Cruz Biotechnology Inc., Dallas TX, USA).

The next day, the membrane was washed 3×10 min with TBST under agitation at RT. Secondary antibody was diluted 1:20 000 in 5% skim milk blocking solution, and added to the membrane and incubated for 90 min under agitation at RT. The secondary antibodies used were Pierce<sup>™</sup> Antibody Goat Anti-Rabbit IgG (H+L) #31462, and Pierce<sup>™</sup> Antibody Goat Anti-Mouse IgG (H+L) #31430, (depending on the host of the primary antibody) both from (Thermo Scientific, USA). After the incubation of primary antibodies were completed, the membrane was again washed with TBST, this time 3×5 min under agitation at RT. For visualization of the protein bands, enhanced chemiluminescence (ECL) was utilized. The secondary antibodies were conjugated with horseradish peroxidase (HRP) that makes certain substrates illuminate. Those used was SuperSignal<sup>®</sup> West Pico Chemiluminescent Substrate and SuperSignal<sup>®</sup> West Femto Maximum Sensitivity Substrate, both from (Thermo

---

Scientific, USA). The images after addition of ECL substrates, was obtained using LAS-3000 Fujifilm Intelligent DarkBox precooled to  $-25^{\circ}\text{C}$ .

For blotting of the VEGFR-2 protein the same basic method applies, but several procedures were modified: The gel used was NuPage<sup>®</sup> 3-8% Tris-Acetate 1.0 mm 10 wells, with NuPage<sup>®</sup> Tris-Acetate SDS Running Buffer. Electrophoresis was performed at constant 100 V for about 90 min. The membrane used was Immobilon<sup>™</sup>-P polyvinylidene difluoride (PVDF) 0.45  $\mu\text{m}$  (Millipore Corporation, Bedford, MA, USA), soaked in absolute ethanol for 5 min prior to transfer. The transfer buffer was added 0.1 % sodium dodecyl sulfate (SDS) (Bio-Rad Laboratories Inc., Hercules, CA, USA). Transfer was carried out at 25 V for 4 hours.

### 3.13 Long-term Treatment with Cabozantinib

To appraise the effect of cabozantinib treatment over time and evaluate possible resistance development, the cell line A172 was chosen for its predictable growth rate and stable culture aspect. A new batch was thawed from the VPLN and grown in a T25 flask until confluency. The flask was split into three T75 flasks. The treatment started when the flasks reached 40 % confluency. Flask 1 (untreated) received only DMEM ALT. Flask 2 (clinical dose) was treated with cabozantinib doses calculated from a clinical point of view. The standard treatment dose of cabozantinib used in the clinic is 60 mg daily [105]. Studies have measured plasma concentration after administration of other cabozantinib doses [106, 107]. Based on these studies, a calculation of corresponding *in vitro* drug doses was done according to pharmacokinetic principles [108]. Thus, the cells were treated with 0.5  $\mu\text{M}$  for one week, 1.0  $\mu\text{M}$  for the second week and then 1.5  $\mu\text{M}$  for the rest of the experiment, to reflect a 60 mg treatment plan. Flask 3 (high dose) was treated with the  $\text{IC}_{50}$  dose for A172. The flasks were passaged alongside each other 10 times, roughly one passage per week over a period of two months (**Figure 3.5**). The growth medium and drug containing growth medium was changed once in between the passages. During the passages, the cells were detached with trypsin and DMEM ALT and spun down at 900 rpm for 4 min. The DMEM ALT was removed and an equal amount of drug containing growth medium was added and the cells resuspended before dispersion into pre-heated culture flasks, to ensure the right concentration of cabozantinib the entire time. After 5 and 10 passages, the cells were cultured in regular growth medium for 50

hours (wash-out of drug), to make sure no remaining cabozantinib could influence the final testing. Resazurin assay as described in section 3.4.1 was performed to utilize the effect of long-term treatment. Three plates per flask were analyzed. A counting assay was also done after 10 passages.  $5 \times 10^4$  cells were seeded in a 6-well plate, one plate per flask. The cells were allowed to attach for 24 hours. The next day, 3 wells per plate received growth medium and the other 3 were treated with  $5.0 \mu\text{M}$  cabozantinib (volume 2 mL). After 72 hours, each well was counted and cell number obtained.

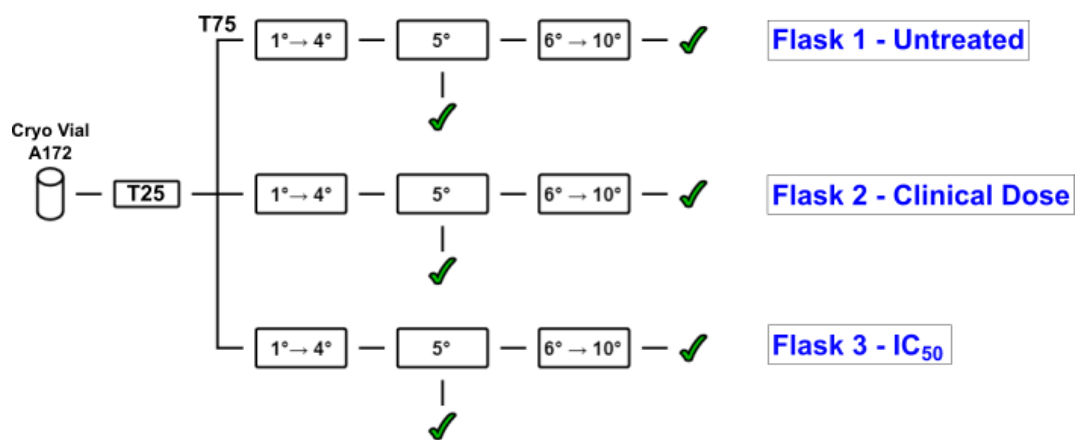


**Figure 3.5** Overview of the long-term treatment regime. A vial of A172 was thawed and grown until confluent in a T25 flask and split into three T75 flasks. These were passaged alongside each other 10 times over a period of two months, with various doses of cabozantinib. The tick indicates wash-out period and resistance evaluation.

## 4. Results

### 4.1 Monolayer Viability Experiments

The viability experiments were performed to utilize the effect of cabozantinib on cell monolayers, and to determine the  $IC_{50}$  doses. A resazurin viability assay was performed to obtain this information. In our experiments, cabozantinib clearly reduced the cell viability in all the cell lines (**Figure 4.1**). When plotting relative cell viability in percentage against increasing logarithmical drug doses, the results showed a dose-dependent deprivation of viability. The  $IC_{50}$  doses were in the low micromolar range for all the cell lines, varying from 2- to 13.06  $\mu$ M.  $IC_{50}$  values indicates that half of the cells are non-viable. The dose-response curves had the typical sigmoid shape.

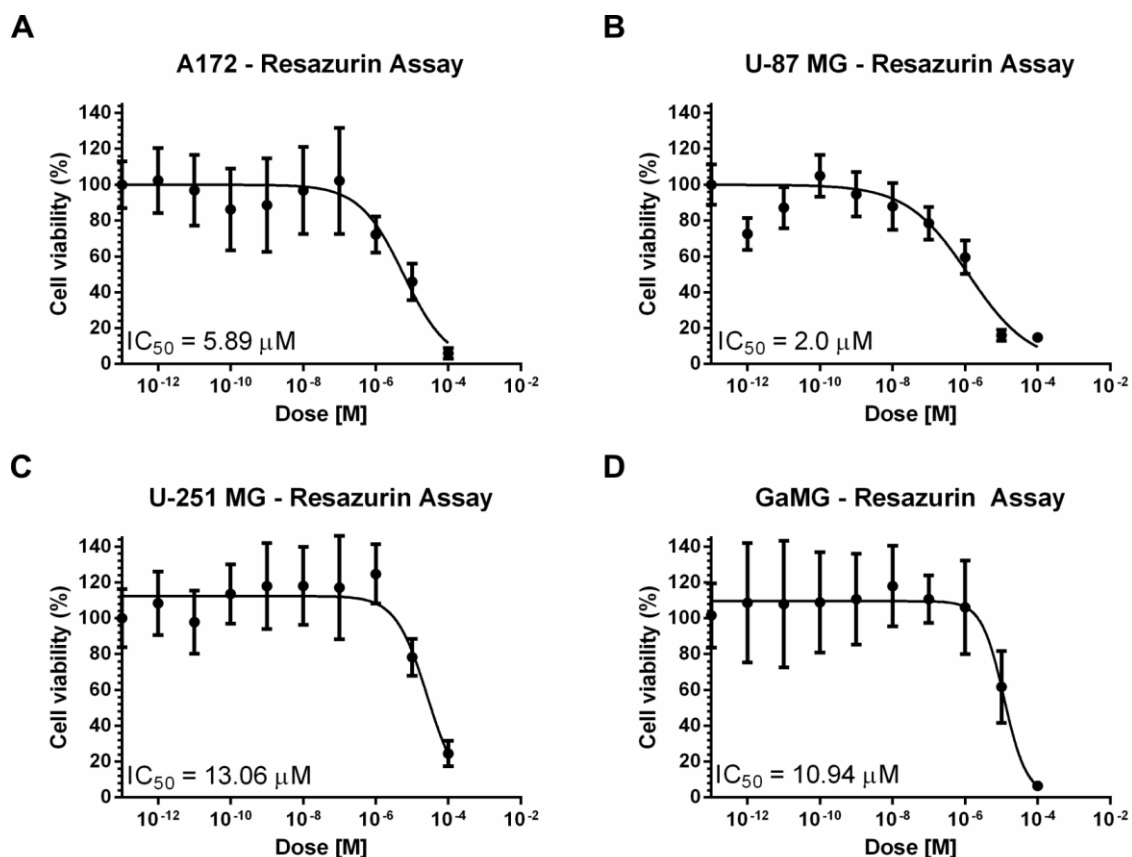


**Figure 4.1** Dose-response curves for the viability using the resazurin assay for the four cell lines. Mean  $\pm$  SD. The viability is represented on the y-axis and increasing log doses of cabozantinib in molar on the x-axis. The assay was carried out three times, and a representative graph per cell line is shown here. The  $IC_{50}$  dose is the mean dose of the three replicates.

**Table 4.1** Overview of the mean IC<sub>50</sub> doses and related SD from the resazurin assay. All doses are given in micromolar.

<b>Monolayer IC<sub>50</sub> Doses (10<sup>-6</sup> M) – Resazurin Assay</b>		
<b>Cell line</b>	<b>Mean IC<sub>50</sub></b>	<b>± SD</b>
A172	5.89	± 2.58
U-87 MG	2.0	± 1.20
U-251 MG	13.06	± 1.93
GaMG	10.94	± 2.62

The mean IC<sub>50</sub> doses obtained from the three resazurin assays with corresponding standard deviation (SD) showed divergent results. U-251 MG had the highest IC<sub>50</sub> dose, whereas U-87 MG has the lowest (**Table 4.1**). The SD was also lowest for the U-87 MG cell line. Based on the IC<sub>50</sub> values of the dose-response curves, the IC<sub>25</sub> dose was calculated mathematically (**Table 4.2**). Since the curve never reached zero for none of the cell lines (**Figure 4.1**), and the highest dose (100 µM) used is very high, this dose was designated as IC<sub>90</sub>. For the U-251 MG and GaMG cell lines (**Figure 4.1C-D**), the maximum viability had to be set above 100 % due to best curve-fit regression. This is taken into account for calculation of the IC<sub>50</sub> doses.

**Table 4.2** The other IC doses used in this thesis based on the IC<sub>50</sub> values and graphs from the resazurin assay.

<b>Other IC Doses Obtained from IC<sub>50</sub></b>		
<b>Cell line</b>	<b>IC<sub>25</sub></b>	<b>IC<sub>90</sub></b>
A172	1.1 µM	~100 µM
U-87 MG	0.6 µM	~100 µM
U-251 MG	7.5 µM	~100 µM
GaMG	1.9 µM	~100 µM

To exclude the possibility of a DMSO effect on the cells, plates with DMSO concentrations corresponding to the content in the dilution fold of cabozantinib treatments in the resazurin assay was analyzed in triplicates. Two additional plates, one with the DMSO corresponding to the 100 µM treatment and with only DMEM ALT was also analyzed. The results showed no effect of the DMSO, and the cells were as viable as the untreated ones (data not shown).

Images, both bright-field and fluorescent with LIVE/DEAD<sup>®</sup> staining were obtained for all the cell lines, untreated and treated with the three IC doses (**Figure 4.2-4.5**). All images were obtained using a 10× objective.

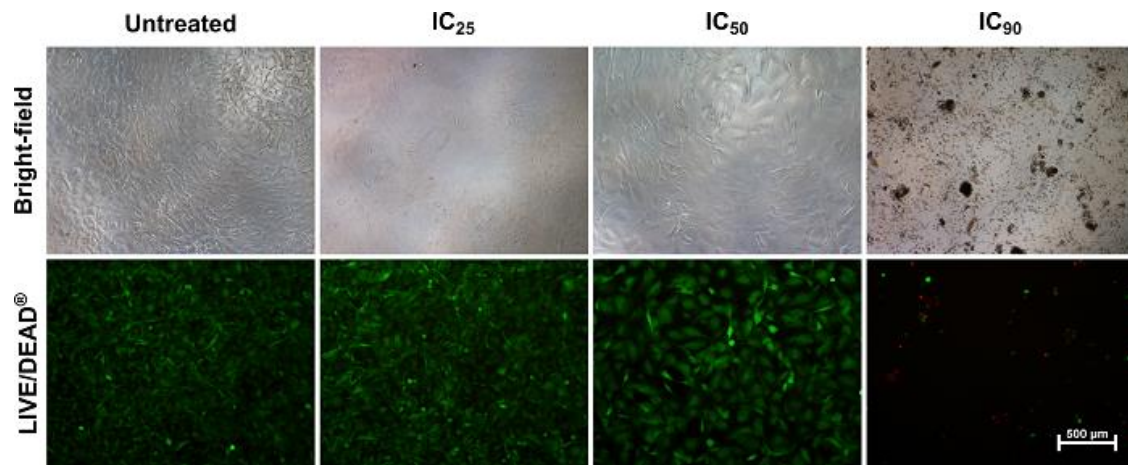


**Figure 4.2** Viability bright-field and LIVE/DEAD® images of the A172 cell line. Scale bar = 500  $\mu\text{m}$

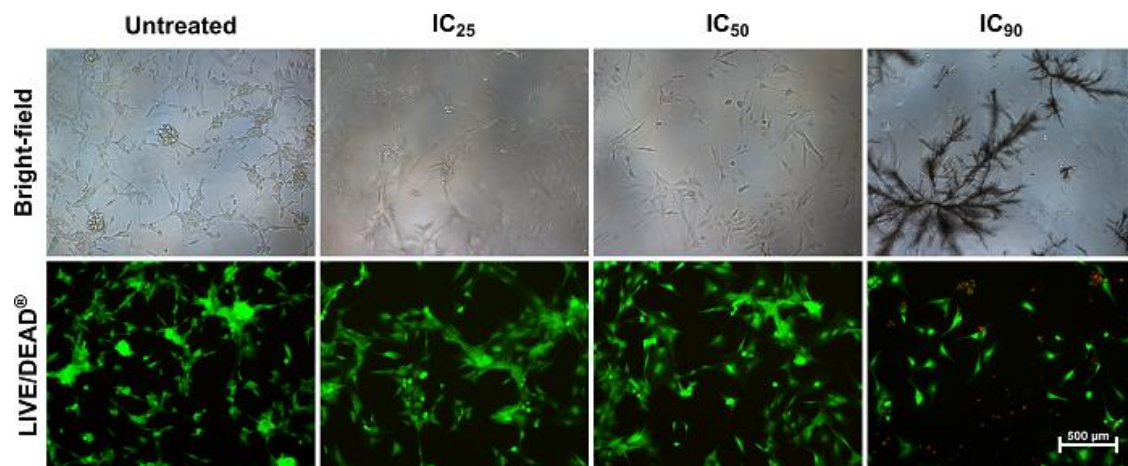


**Figure 4.3** Viability bright-field and LIVE/DEAD® images of the U-87 MG cell line. Scale bar = 500  $\mu\text{m}$

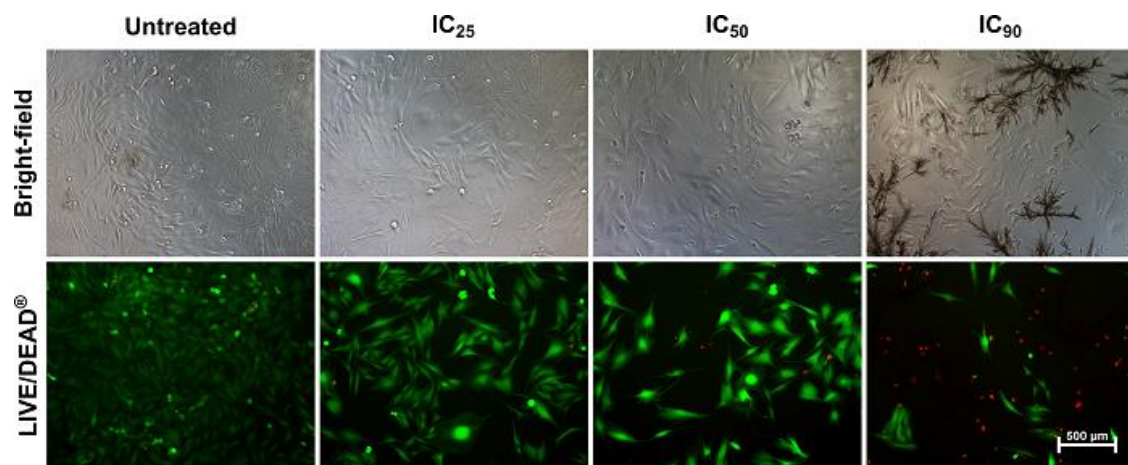


**Figure 4.4** Viability bright-field and LIVE/DEAD® images of the U-251 MG cell line. Scale bar = 500  $\mu\text{m}$ .

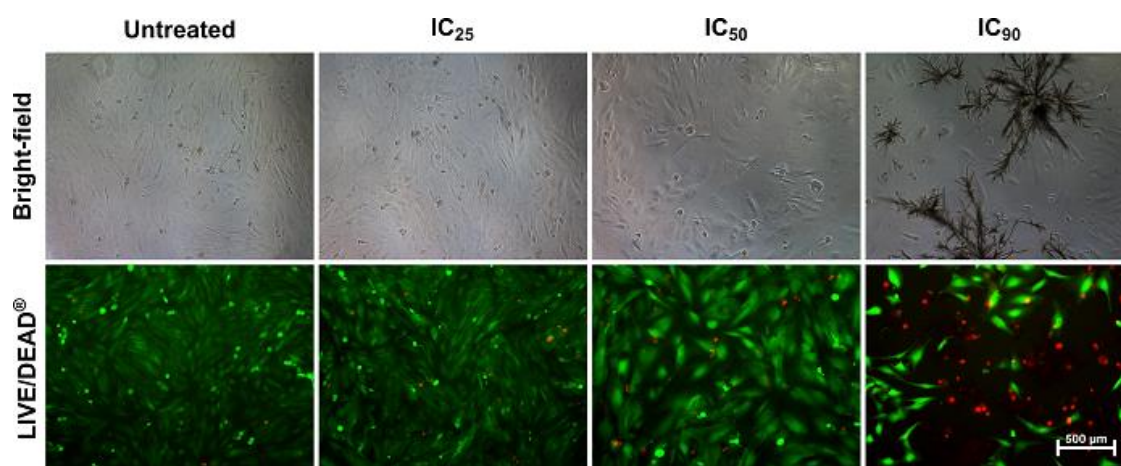


**Figure 4.5** Viability bright-field and LIVE/DEAD® images of the GaMG cell line. Scale bar = 500  $\mu\text{m}$ .

The number of cells in general decreased with increasing drug doses for all cell lines, this was especially seen for the IC<sub>90</sub> dose. The cells also increased somewhat in size after IC<sub>25</sub> or IC<sub>50</sub> treatment. For the highest dose of cabozantinib, the drug crystalized into small flakes, which was very clear on the bright-field images, except for A172 where the drug made round clumps (**Figure 4.2-4.5**). For the A172 cell line, the number of live cells also decreased with increasing doses, although dead cells were not very prominent for neither of the drug doses. This cell line also had the lowest number of cells left when the IC<sub>90</sub> dose was used (**Figure 4.2**). The cell line U-87 MG made typical clusters, which are well shown on both bright-field and LIVE/DEAD® images. Very few dead cells were visible (**Figure 4.3**). The increase in cell volume after treatment was very prominent for the U-251 MG cell line. Untreated cells were small, but increased with increasing doses of cabozantinib (**Figure 4.4**). The number of dead cells were highest in the GaMG cell line (**Figure 4.5**).

## 4.2 Cell Tumorigenicity – Clonogenic Assay

An evaluation of the tumorigenic potential of the cells after treatment of cabozantinib was done using the clonogenic assay. The assay was performed twice, once plating out  $1 \times 10^3$  cells and one with  $5 \times 10^3$  cells, in triplicates. This was done to evaluate the implication of cell seeding density on the final results. As the cell lines formed various sized colonies, one colony size was defined for each cell line after a microscopic examination. For A172  $\geq 30$  cells, U-87 MG  $\geq 10$  cells, U-251 MG  $\geq 20$  and GaMG  $\geq 50$  cells (**Figure 4.6-4.9**).

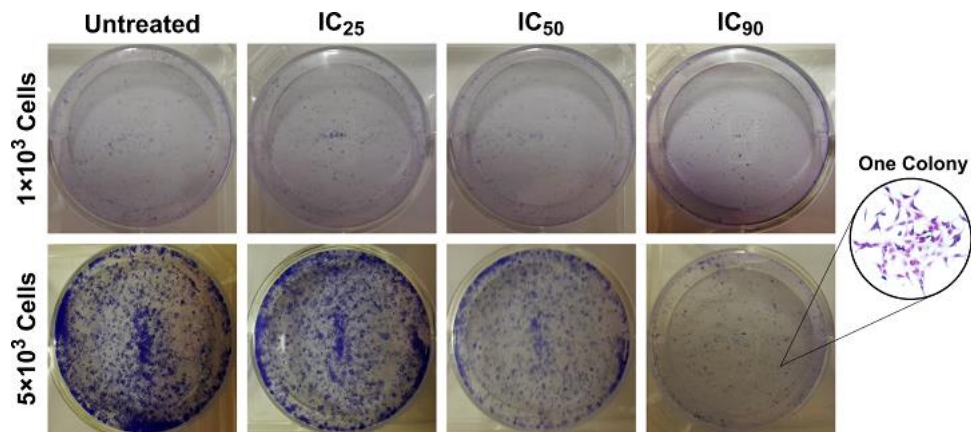


**Figure 4.6** Images of colonies from the A172 cell line. The top row shows colonies after seeding 1×10<sup>3</sup> cells and below 5×10<sup>3</sup>. For this cell line, one colony was defined as ≥ 30 cells.

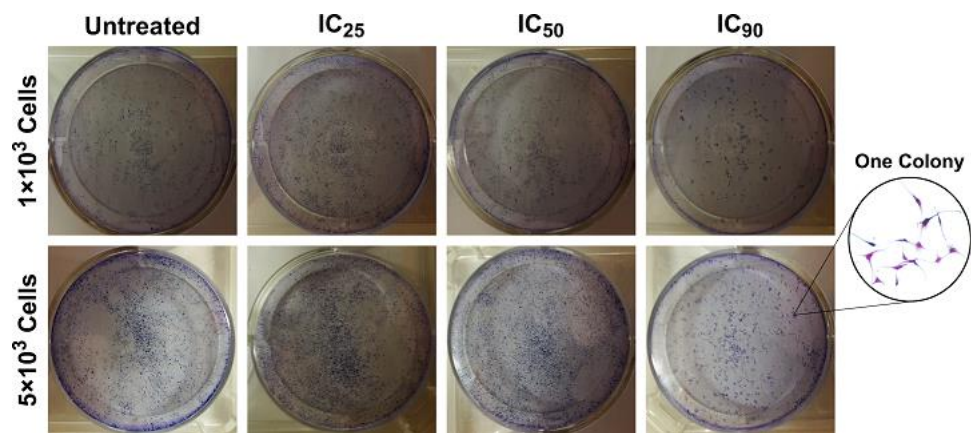


**Figure 4.7** Images of colonies from the U-87 MG cell line. The top row shows colonies after seeding 1×10<sup>3</sup> cells and below 5×10<sup>3</sup>. For this cell line, one colony was defined as ≥ 10 cells.

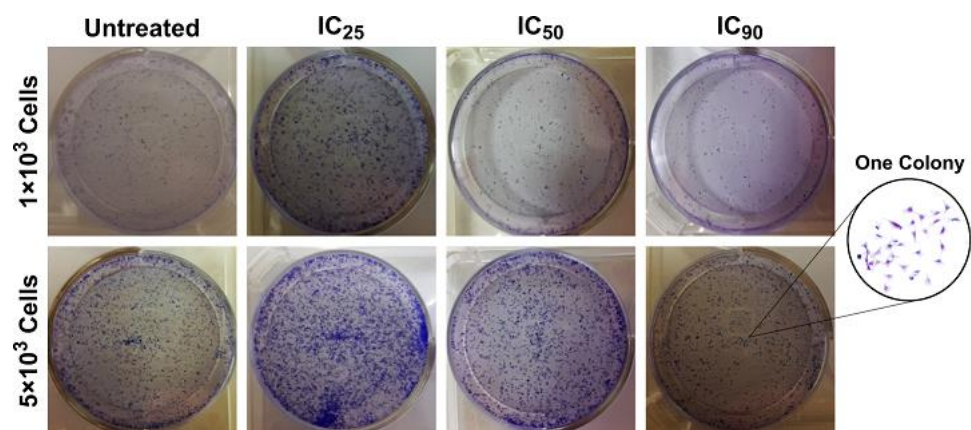


**Figure 4.8** Images of colonies from the U-251 MG cell line. The top row shows colonies after seeding 1×10<sup>3</sup> cells and below 5×10<sup>3</sup>. For this cell line, one colony was defined as ≥ 20 cells.

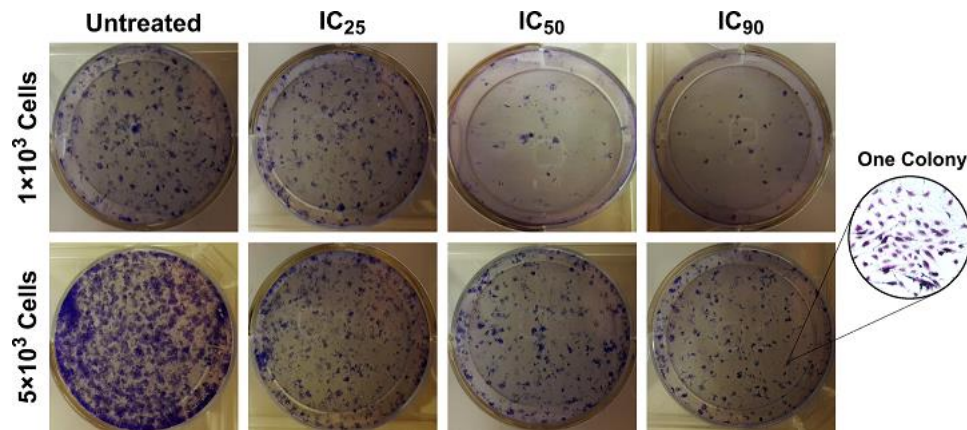


**Figure 4.9** Images of colonies from the GaMG cell line. The top row shows colonies after seeding  $1 \times 10^3$  cells and below  $5 \times 10^3$ . For this cell line, one colony was defined as  $\geq 50$  cells.

Cabozantinib generally reduced the tumorigenicity for all the cell lines, since fewer colonies formed with increasing doses of drug (**Figure 4.6-4.9**). However, the  $IC_{25}$  dose surprisingly increased the formation of colonies except for the GaMG cell line both for the  $1 \times 10^3$  and the  $5 \times 10^3$  seeding experiments. All the colonies were counted, and the results indicated that the seeding density had no impact on the final results, as the relative number of cells were the same. For this reason, only the  $1 \times 10^3$  experiment is further described (**Figure 4.10**). A two-tailed unpaired student *T*-test showed that the number of colonies were statistically significant when comparing untreated cells and cells treated with the  $IC_{50}$  for A172 ( $p \leq 0.05$ ) and GaMG ( $p \leq 0.001$ ). When comparing untreated cells with cells treated with the  $IC_{90}$  dose the results were significant for all cell lines: A172 ( $p \leq 0.001$ ), U-87 MG ( $p \leq 0.05$ ), U-251 ( $p \leq 0.01$ ) and GaMG ( $p \leq 0.001$ ).

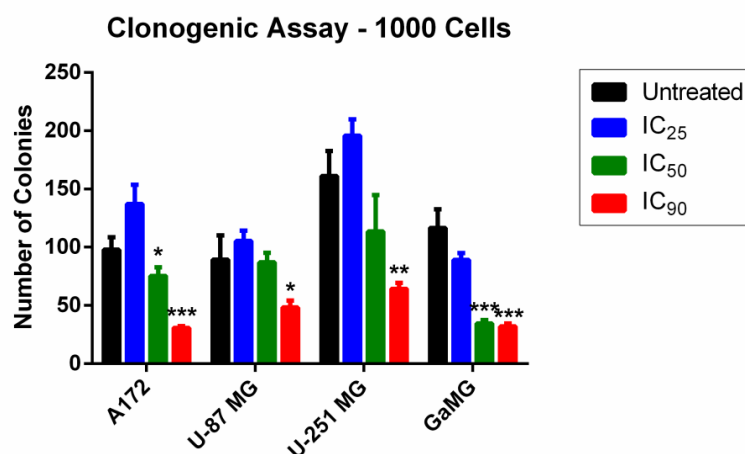


**Figure 4.10** Number for colonies formed after seeding 1000 cells. Mean  $\pm$  SD. (\* =  $p \leq 0.05$ , \*\* =  $p \leq 0.01$  and \*\*\* =  $p \leq 0.001$ .)

### 4.3 Cell Cycle Analysis

Propidium iodide stained cells were analyzed by flow cytometry to identify cell cycle distribution based on DNA quantity before and after treatment with cabozantinib. Triplicates of each sample were analyzed. A two-tailed unpaired student *T*-test comparing treated cells with untreated cells was used for statistical analysis.

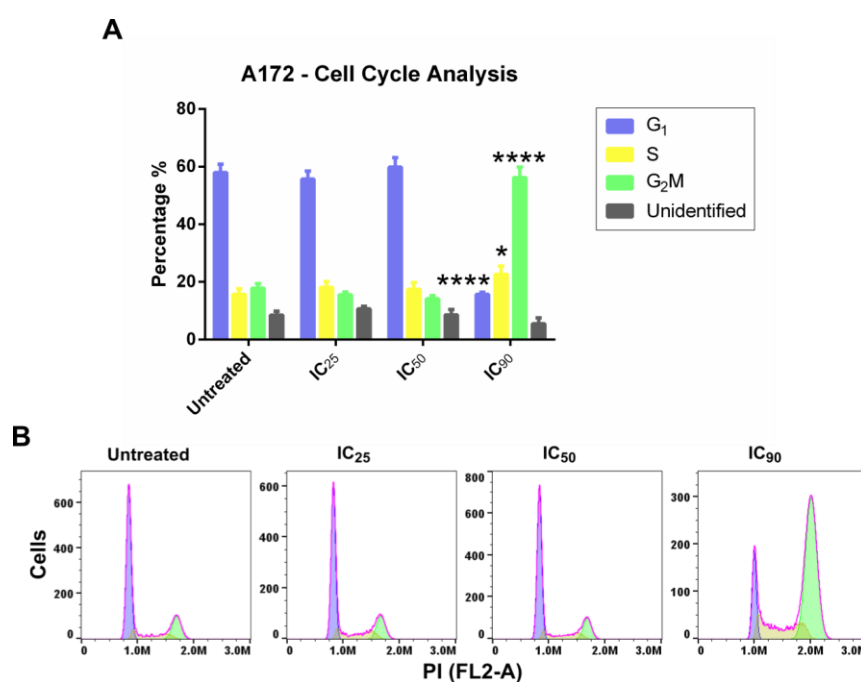


**Figure 4.11** Cell cycle analysis of the A172 cell line. **A)** The distribution in percentage of the different cell cycle phases for the untreated and treated samples. Mean  $\pm$  SD. (\* =  $p \leq 0.05$ , \*\* =  $p \leq 0.01$ , \*\*\* =  $p \leq 0.001$ , \*\*\*\* =  $p \leq 0.0001$  for untreated vs. IC<sub>90</sub>.) **B)** Histograms of the cell cycle for the untreated and three treatments, x-axis = number of cells and y-axis indicates PI detected in FL2-A. Blue = G<sub>1</sub> phase, yellow = S phase and green = G<sub>2</sub>M phase.

Little or no difference was observed for A172 when comparing IC<sub>25</sub>, and IC<sub>50</sub> with the untreated sample (**Figure 4.11**). Cabozantinib clearly induced G<sub>2</sub>M arrest at the highest drug concentration ( $p \leq 0.0001$ ). There was also a small increase of cells in the S phase at this dose ( $p \leq 0.05$ ), and a significant decrease in G<sub>1</sub> phase ( $p \leq 0.0001$ ).

U-87 MG also underwent G<sub>2</sub>M arrest at IC<sub>90</sub> ( $p \leq 0.01$ ) (**Figure 4.12**). A significant decrease in G<sub>1</sub> phase ( $p \leq 0.001$ ) and a small increase in S phase ( $p \leq 0.05$ ) was also observed. For the lower doses, there seemed to be no effect in cell cycle distribution.

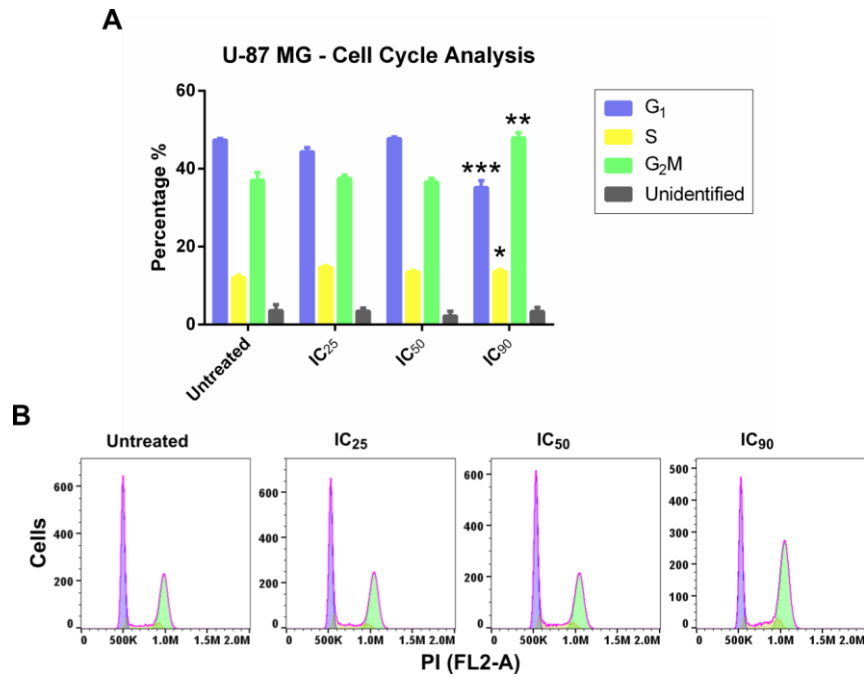


**Figure 4.12** Cell cycle analysis of the U-87 MG cell line. **A)** The distribution in percentage of the different cell cycle phases for the untreated and treated samples. Mean  $\pm$  SD. (\* =  $p \leq 0.05$ , \*\* =  $p \leq 0.01$ , \*\*\* =  $p \leq 0.001$ , \*\*\*\* =  $p \leq 0.0001$  for untreated vs. IC<sub>90</sub>.) **B)** Histograms of the cell cycle for the untreated and three treatments, x-axis = number of cells and y-axis indicates PI detected in FL2-A. Blue = G<sub>1</sub> phase, yellow = S phase and green = G<sub>2</sub>M phase.

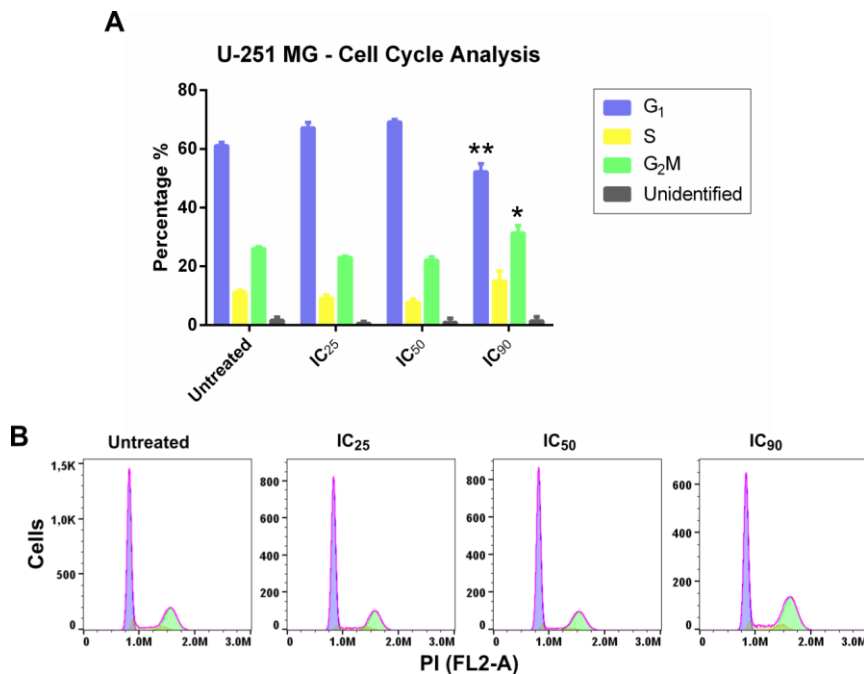


**Figure 4.13** Cell cycle analysis of the U-251 MG cell line. **A)** The distribution in percentage of the different cell cycle phases for the untreated and treated samples. Mean  $\pm$  SD. (\* =  $p \leq 0.05$ , \*\* =  $p \leq 0.01$ , \*\*\* =  $p \leq 0.001$ , \*\*\*\* =  $p \leq 0.0001$  for untreated vs. IC<sub>90</sub>.) **B)** Histograms of the cell cycle for the untreated and three treatments, x-axis = number of cells and y-axis indicates PI detected in FL2-A. Blue = G<sub>1</sub> phase, yellow = S phase and green = G<sub>2</sub>M phase.

A small G<sub>2</sub>M arrest was identified for the U-251 MG cell line at IC<sub>90</sub> ( $p \leq 0.05$ ) (**Figure 4.13**). Significant changes were not observed for the lower doses of cabozantinib, although the results indicated an increase in the G<sub>1</sub> phase. For the IC<sub>90</sub> no significant change was found in the S phase, however a decrease in G<sub>1</sub> phase was observed ( $p \leq 0.01$ ).

The results for GaMG differed, compared to the other cell lines (**Figure 4.14**). In general, the cell line had more cells in the S phase. After treatment with IC<sub>90</sub>, there was a significant increase of cells in the G<sub>2</sub>M phase ( $p \leq 0.01$ ), indicating G<sub>2</sub>M arrest. An increase in S phase ( $p \leq 0.01$ ) and a decrease in G<sub>1</sub> phase ( $p \leq 0.001$ ) suggested a concurrent shift from the G<sub>1</sub> phase to the S and G<sub>2</sub>M phases.

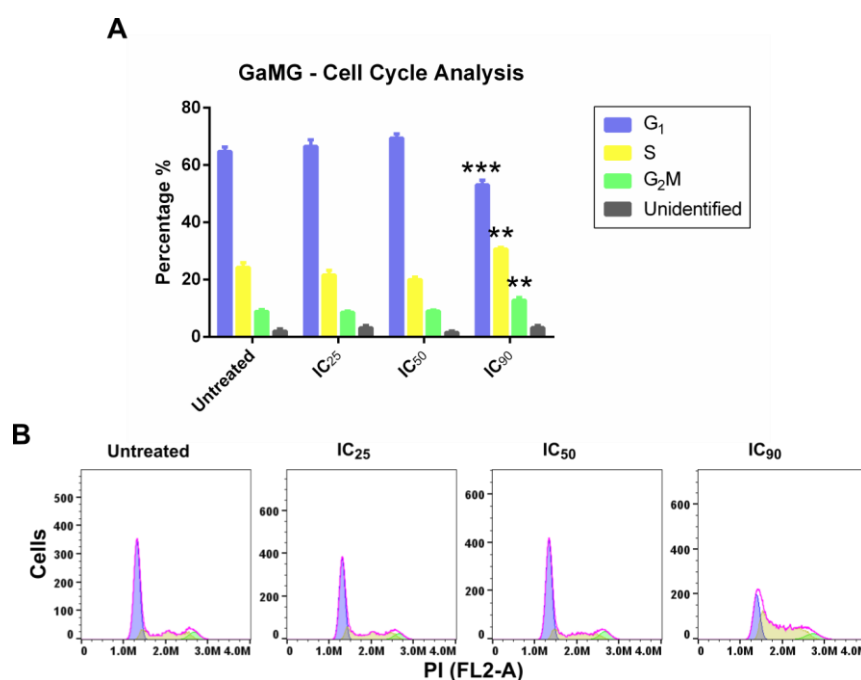


**Figure 4.14** Cell cycle analysis of the GaMG cell line. **A)** The distribution in percentage of the different cell cycle phases for the untreated and treated samples. Mean  $\pm$  SD. (\* =  $p \leq 0.05$ , \*\* =  $p \leq 0.01$ , \*\*\* =  $p \leq 0.001$ , \*\*\*\* =  $p \leq 0.0001$  for untreated vs. IC<sub>90</sub>.) **B)** Histograms of the cell cycle for the untreated and three treatments, x-axis = number of cells and y-axis indicates PI detected in FL2-A. Blue = G<sub>1</sub> phase, yellow = S phase and green = G<sub>2</sub>M phase.

## 4.4 Apoptosis Assay

A flow cytometry-based assay was used to study the effects of cabozantinib on apoptosis. Propidium iodide stains the nucleic acid of dead cells, and Annexin V binds to membranes of apoptotic cells. Triplicates of each sample was analyzed.

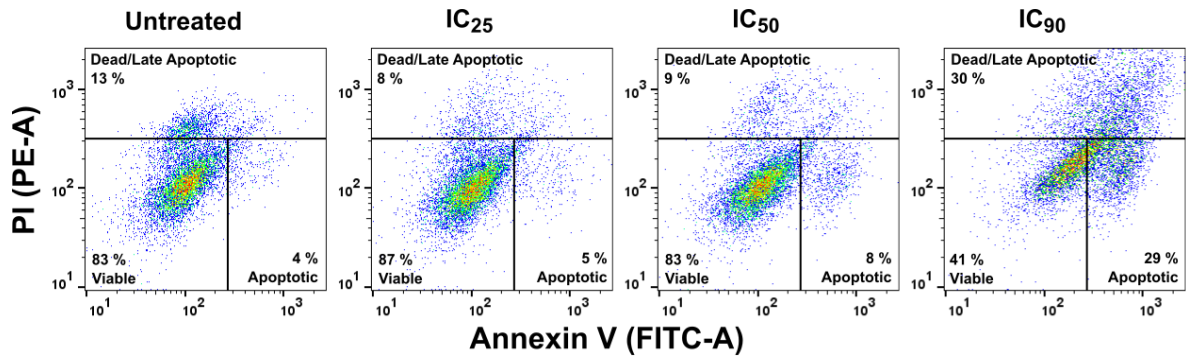


**Figure 4.15** Flow cytometry-based apoptosis distribution of the A172 cell line. Untreated sample and increasing doses of cabozantinib. The gating shows the distribution of viable-, apoptotic- and dead/late apoptotic cells (rounded off to the closest integer). The y-axis represents the detection of PI in the PE-A channel, and the x-axis Annexin V in the FITC-A channel of the flow cytometer.

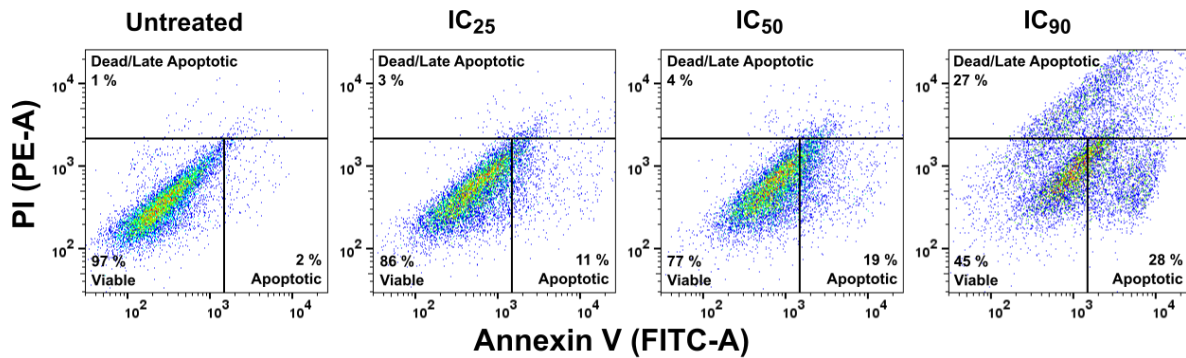


**Figure 4.16** Flow cytometry-based apoptosis distribution of the U-87 MG cell line. Untreated sample and increasing doses of cabozantinib. The gating shows the distribution of viable-, apoptotic- and dead/late apoptotic cells (rounded off to the closest integer). The y-axis represents the detection of PI in the PE-A channel, and the x-axis Annexin V in the FITC-A channel of the flow cytometer.

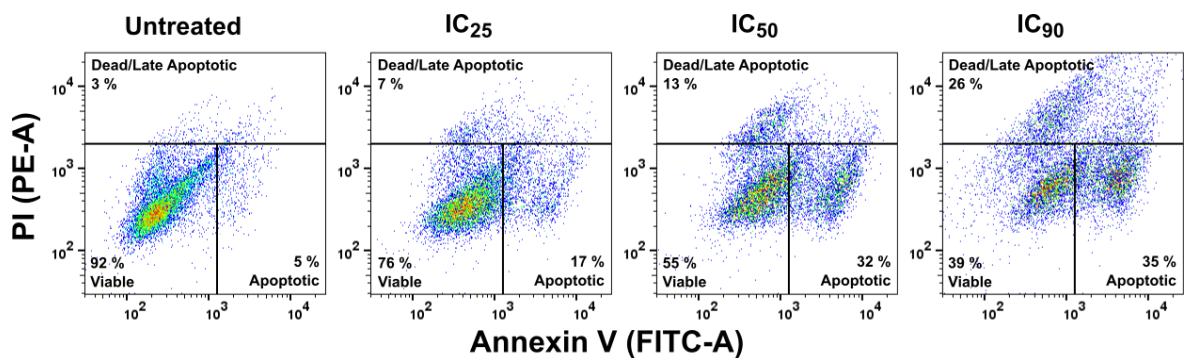


**Figure 4.17** Flow cytometry-based apoptosis distribution of the U-251 MG cell line. Untreated sample and increasing doses of cabozantinib. The gating shows the distribution of viable-, apoptotic- and dead/late apoptotic cells (rounded off to the closest integer). The y-axis represents the detection of PI in the PE-A channel, and the x-axis Annexin V in the FITC-A channel of the flow cytometer.

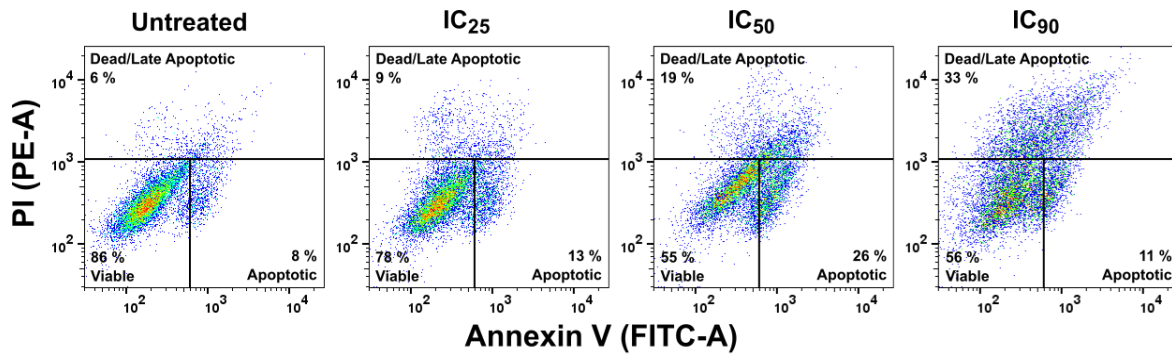


**Figure 4.18** Flow cytometry-based apoptosis distribution of the GaMG cell line. Untreated sample and increasing doses of cabozantinib. The gating shows the distribution of viable-, apoptotic- and dead/late apoptotic cells (rounded off to the closest integer). The y-axis represents the detection of PI in the PE-A channel, and the x-axis Annexin V in the FITC-A channel of the flow cytometer.

Overall, there was a decrease in viable (live) cells, and an increase in apoptotic- and dead cells with increasing drug doses, when examining the flow diagrams (**Figure 4.15-4.18**). The diagrams show the most representative flow chart of the three analyzed samples. Unstained sample was used to set the gating parameters, and is cell line dependent.

#### Apoptosis Assay - Flow Cytometry

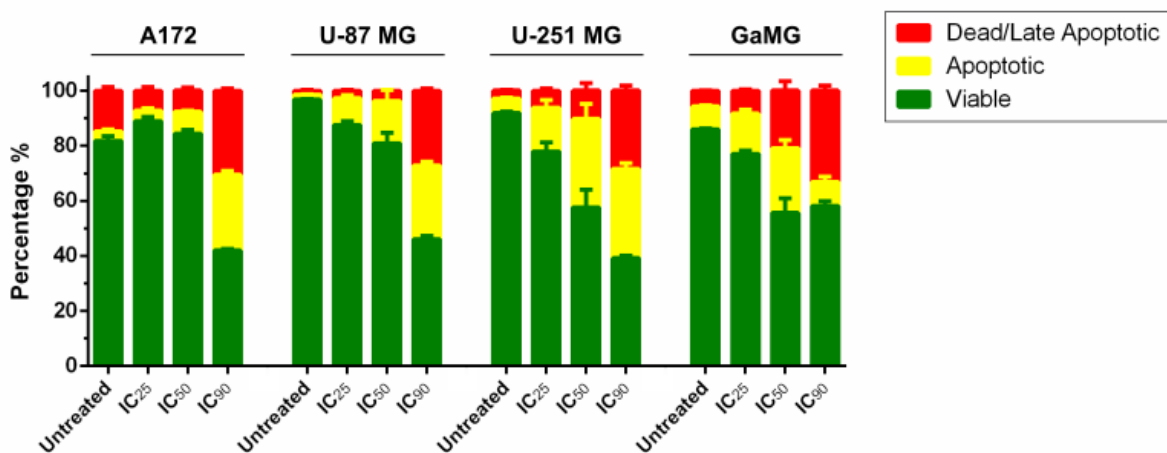


**Figure 4.19** Quantification of the flow cytometry-based apoptosis assay. The diagram shows the distribution of cells within each population: viable, apoptotic, and dead/late apoptotic, for untreated and treated samples. Mean  $\pm$  SD.

The quantification of the results from the flow study showed a dose-dependent increase in rate of apoptosis for all cell lines, especially for the IC<sub>90</sub> treatment (**Figure 4.19**). A two-way

ANOVA analysis, comparing the treatments against the untreated in each of the three cell populations (Dunnett's multiple comparisons test) revealed statistical significance ( $p \leq 0.0001$ ) for each cell line.

## 4.5 Mitochondrial Membrane Potential

To assess the ability of cabozantinib to interfere with the mitochondria, an evaluation of mitochondrial potential was performed. The assay was performed in triplicates. A two-tailed unpaired student *T*-test was used for statistical evaluation. The fluorometric measurement and images are from two different experiments. All images were obtained using a 10 $\times$  objective. A DMSO control was also included and revealed no effect (data not shown).

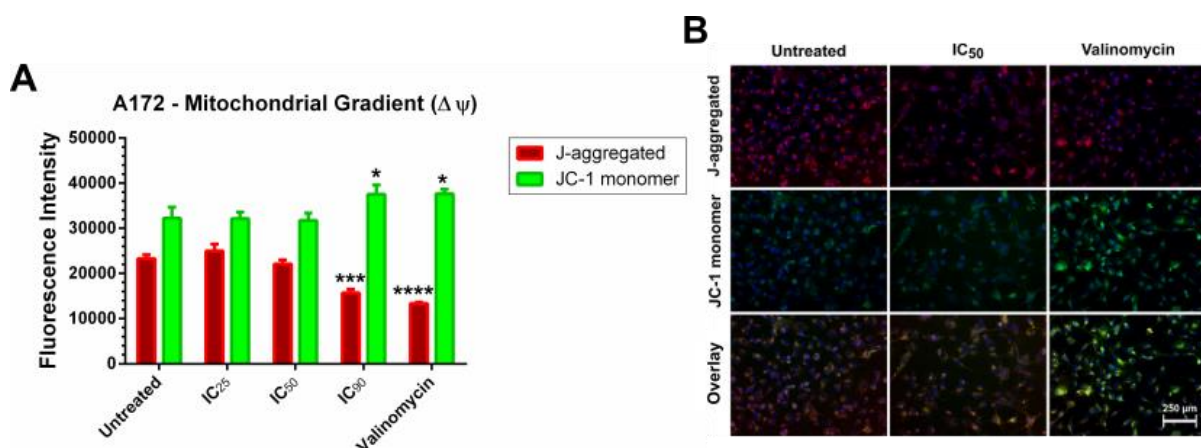


**Figure 4.20** Mitochondrial gradient disruption in the A172 cells. **A)** Fluorometric analysis of the J-aggregated (intact membrane) and JC-1 monomer (disrupted membrane). Mean  $\pm$  SD. (\* =  $p \leq 0.05$ , \*\* =  $p \leq 0.01$ , \*\*\* =  $p \leq 0.001$ , \*\*\*\* =  $p \leq 0.0001$  for untreated vs. treatments.) **B)** Fluorescent images of the J-aggregated, and JC-1 monomer, along with overlays for untreated, IC<sub>50</sub> and valinomycin. Cell nuclei are stained blue. Scale bar = 250  $\mu$ m.

Cabozantinib disrupted the membrane and decreased the  $\Delta\psi$  for the A172 cell line (**Figure 4.20**). Although a trend was seen for all treatments, a statistical significance was only found for IC<sub>90</sub> and valinomycin. The images confirmed an increase in green fluorescence after treatment, which indicates damaged mitochondria.

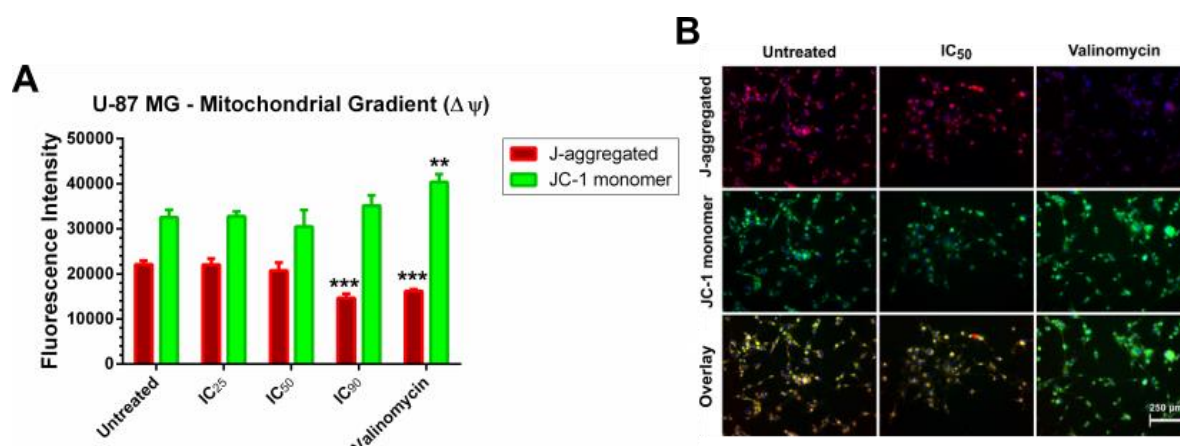


**Figure 4.21** Mitochondrial gradient disruption in the U-87 MG cells. **A)** Fluorometric analysis of the J-aggregated (intact membrane) and JC-1 monomer (disrupted membrane). Mean  $\pm$  SD. (\* =  $p \leq 0.05$ , \*\* =  $p \leq 0.01$ , \*\*\* =  $p \leq 0.001$ , \*\*\*\* =  $p \leq 0.0001$  for untreated vs. treatments.) **B)** Fluorescent images of the J-aggregated, and JC-1 monomer, along with overlays for untreated, IC<sub>50</sub> and valinomycin. Cell nuclei are stained blue. Scale bar = 250  $\mu$ m.

For the U-87 MG cell line, the results also showed a disruption of the  $\Delta\psi$  (**Figure 4.21**). Equally significant differences were found for IC<sub>90</sub> and valinomycin, which suggests a complete disruption of the membrane potential. The images also verified this.

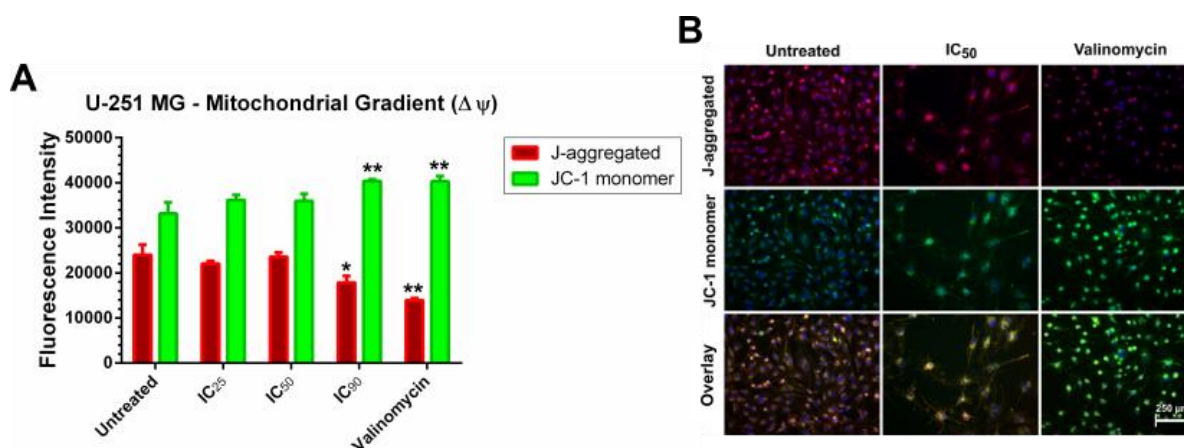


**Figure 4.22** Mitochondrial gradient disruption in the U-251 MG cells. **A)** Fluorometric analysis of the J-aggregated (intact membrane) and JC-1 monomer (disrupted membrane). Mean  $\pm$  SD. (\* =  $p \leq 0.05$ , \*\* =  $p \leq 0.01$ , \*\*\* =  $p \leq 0.001$ , \*\*\*\* =  $p \leq 0.0001$  for untreated vs. treatments.) **B)** Fluorescent images of the J-aggregated, and JC-1 monomer, along with overlays for untreated, IC<sub>50</sub> and valinomycin. Cell nuclei are stained blue. Scale bar = 250  $\mu$ m.

Similar results were also found for the U-251 MG cell line, showing a significant disruption of the membrane potential for IC<sub>90</sub> and valinomycin (**Figure 4.23**). The fluorescent intensity measurement revealed a less disrupted membrane for the IC<sub>90</sub> than valinomycin control.

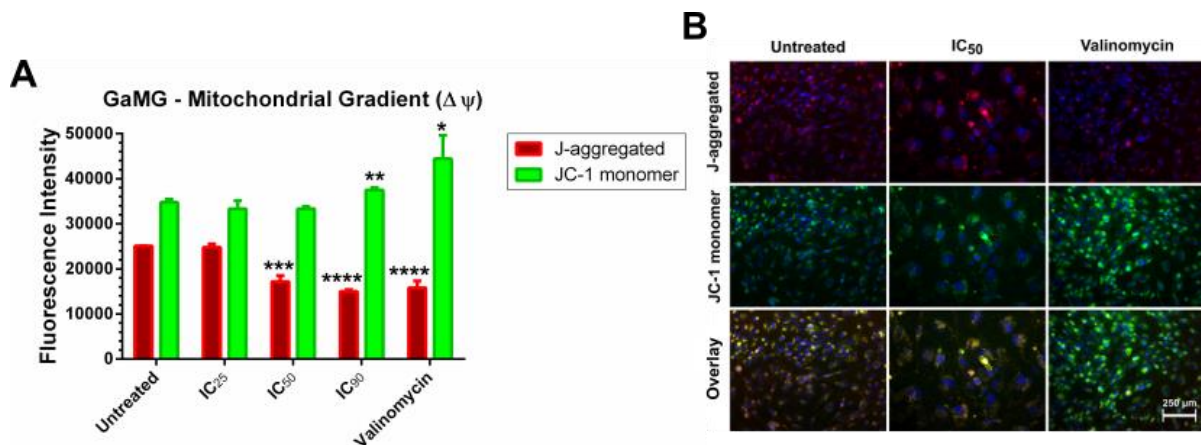


**Figure 4.23** Mitochondrial gradient disruption in the GaMG cells. **A**) Fluorometric analysis of the J-aggregated (intact membrane) and JC-1 monomer (disrupted membrane). Mean  $\pm$  SD. (\* =  $p \leq 0.05$ , \*\* =  $p \leq 0.01$ , \*\*\* =  $p \leq 0.001$ , \*\*\*\* =  $p \leq 0.0001$  for untreated vs. treatments.) **B**) Fluorescent images of the J-aggregated, and JC-1 monomer, along with overlays for untreated, IC<sub>50</sub> and valinomycin. Cell nuclei are stained blue. Scale bar = 250  $\mu$ m.

The GaMG cells were the most sensitive of all four cell lines in these experiments (**Figure 4.23**). There was a significant decrease of J-aggregated fluorescence already at IC<sub>50</sub> ( $p \leq 0.001$ ), and even more significant results for IC<sub>90</sub> and valinomycin ( $p \leq 0.0001$ ). The J-aggregated showed an even greater decrease than the valinomycin treated sample.

## 4.6 Growth Inhibition of Tumor Spheroids

The impact of cabozantinib on the growth rate of 3D tumor spheroids was measured over a period of 21 days. All images were obtained using a 4 $\times$  objective. Triplicate spheroid experiments were performed. In general, the images (**Figure 4.24-4.27**) illustrated that the untreated tumor spheroids grew faster than the treated ones. The spheroids differed in size, which was cell line dependent. Since a small DMSO effect was observed for the U-251 MG cell line (**Figure 4.26**), the DMSO control was included in the results of this experiment.

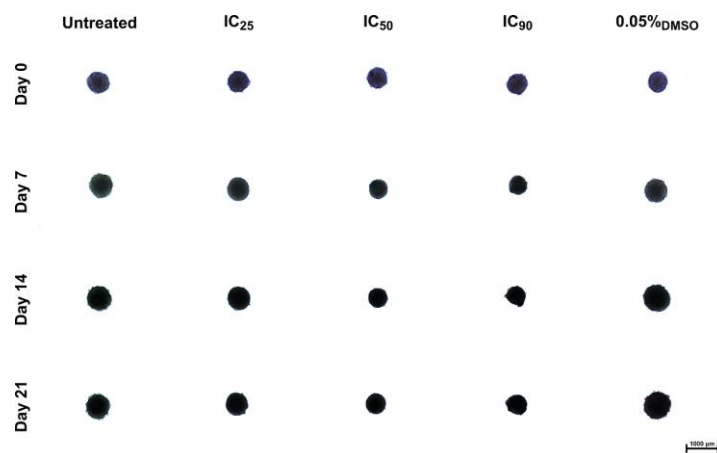


**Figure 4.24** Images of A172 spheroids over a 21-days treatment regime. A DMSO control was also included. Scale bar = 1000 μm.

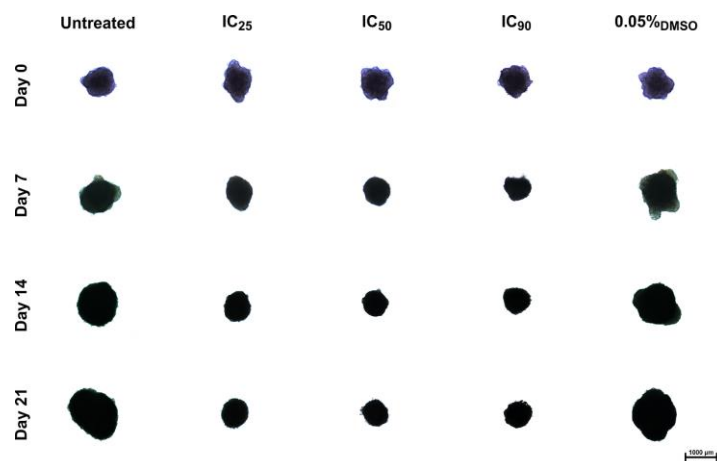


**Figure 4.25** Images of U-87 MG spheroids over a 21-days treatment regime. A DMSO control was also included. Scale bar = 1000 μm.

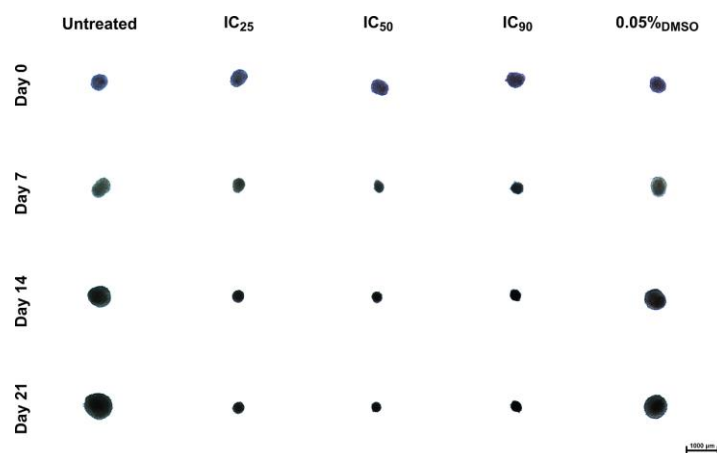


**Figure 4.26** Images of U-251 MG spheroids over a 21-days treatment regime. A DMSO control was also included. Scale bar = 1000 μm.

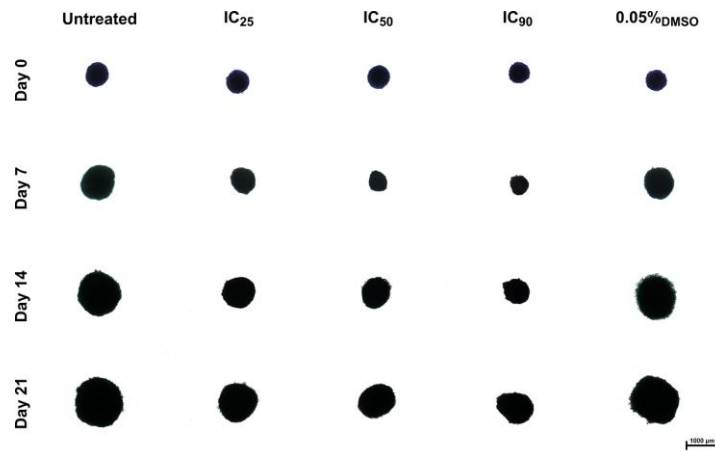


**Figure 4.27** Images of GaMG spheroids over a 21-days treatment regime. A DMSO control was also included. Scale bar = 1000  $\mu\text{m}$ .

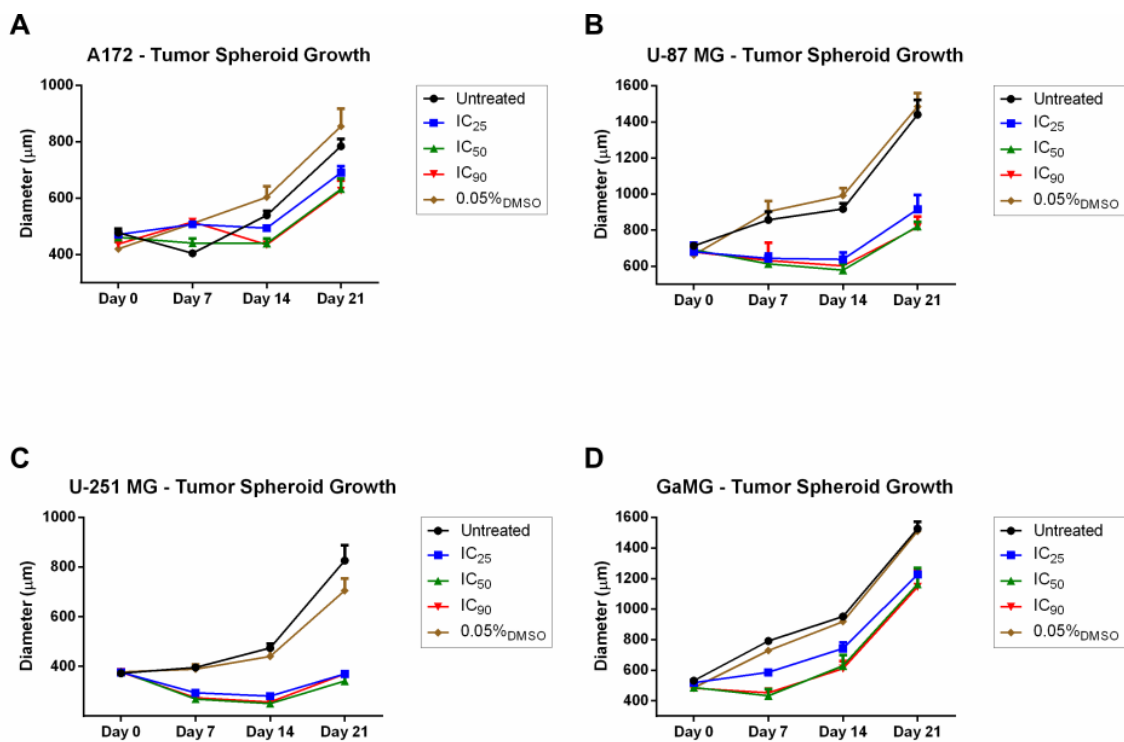


**Figure 4.28** Growth curves of tumor spheroids for all cell lines. The diameter (in  $\mu\text{m}$ ) of spheroids plotted against each registration day. Mean  $\pm$  SD. **A)** A172 cell line **B)** U-87 MG cell line **C)** U-251 MG cell line and **D)** GaMG cell line.

The growth curves for each cell line illustrated an increase of growth with time for all treatments (**Figure 4.28**). A two-tailed unpaired student *T*-test was used for comparison of individual spheroids on day 21, untreated against treatments (**Table 4.3**). All cell lines had significant results for all treatments. None of the DMSO controls were significant.

**Table 4.3** Results on the final day of spheroid treatment. The table shows  $p$ -values from a two-tailed unpaired student  $T$ -test, untreated spheroid compared against the different treated spheroids. n.s. = not significant.

<i>Treatment</i>	<b>Cell Lines</b>			
	<b>A172</b>	<b>U-87 MG</b>	<b>U-251 MG</b>	<b>GaMG</b>
IC <sub>25</sub>	≤ 0.05	≤ 0.01	≤ 0.001	≤ 0.001
IC <sub>50</sub>	≤ 0.01	≤ 0.001	≤ 0.001	≤ 0.01
IC <sub>90</sub>	≤ 0.01	≤ 0.001	≤ 0.001	≤ 0.01
0.05% <sub>DMSO</sub>	n.s.	n.s.	n.s.	n.s.

## 4.7 Migration Assay

To evaluate the effect of tumor cell migration after cabozantinib treatment, a 3D spheroid migration assay was performed. Three spheroids were examined per treatment. Images were obtained using a 4× objective. For determination of statistical significance, a two-tailed unpaired student  $T$ -test was carried out comparing treated spheroids against untreated spheroids on the final day of the experiment.

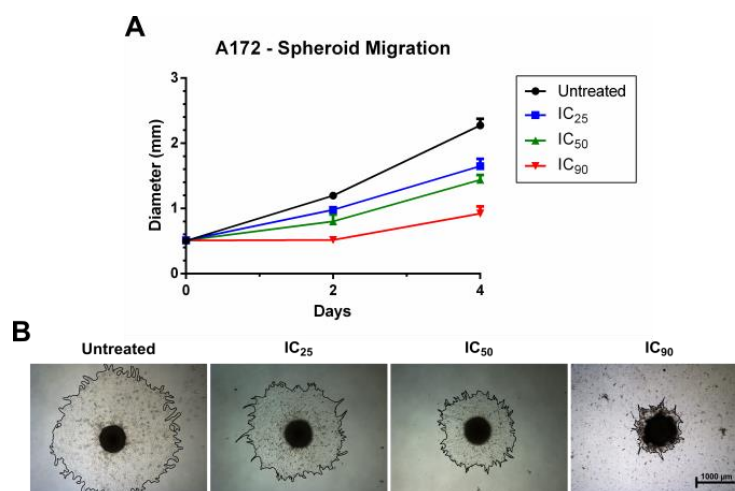


**Figure 4.29** Migration assay of A172 spheroids. **A)** Growth curve for the migration diameter (in mm) for untreated and treated tumor spheroids over a period of four days. Mean  $\pm$  SD. **B)** Images obtained on the last day (day 4) of the migration pattern. Scale bar = 1000  $\mu$ m.

For the A172 cell line, cabozantinib significantly inhibited the migration in a dose-dependent manner (**Figure 4.29**) (IC<sub>25</sub> -  $p \leq 0.01$ ; IC<sub>50</sub> -  $p \leq 0.001$ ; IC<sub>90</sub> -  $p \leq 0.0001$ ). The images obtained, verified these findings.

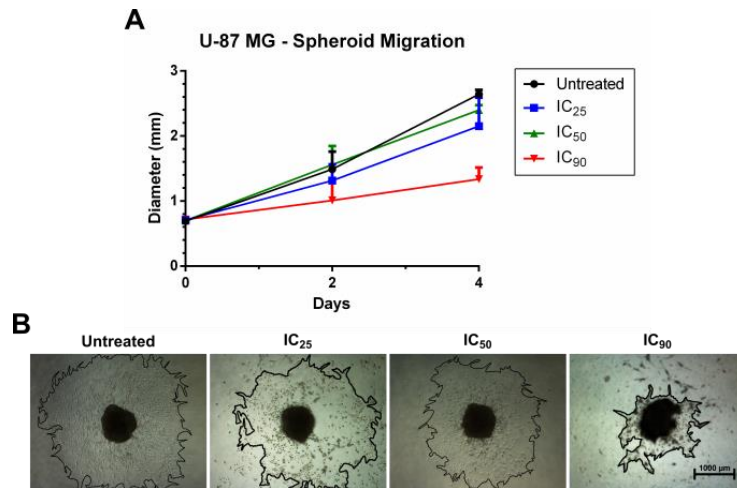


**Figure 4.30** Migration assay of U-87 MG spheroids. **A)** Growth curve for the migration diameter (in mm) for untreated and treated tumor spheroids over a period of four days. Mean  $\pm$  SD. **B)** Images obtained on the last day (day 4) of the migration pattern. Scale bar = 1000  $\mu$ m.

The drug also reduced migration for the U-87 MG cell line on the two highest doses of cabozantinib (**Figure 4.30**). (IC<sub>50</sub> -  $p \leq 0.05$ ; IC<sub>90</sub> -  $p \leq 0.01$ ).

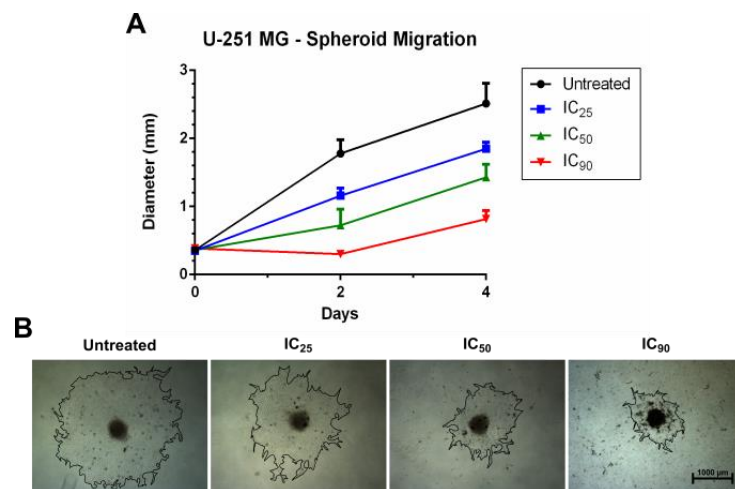


**Figure 4.31** Migration assay of U-251 MG spheroids. **A)** Growth curve for the migration diameter (in mm) for untreated and treated tumor spheroids over a period of four days. Mean  $\pm$  SD. **B)** Images obtained on the last day (day 4) of the migration pattern. Scale bar = 1000  $\mu$ m.

The migration assay for the U-251 MG cell line also shows significant inhibition of the migration pattern (**Figure 4.31**) ( $p \leq 0.01$  for all treatment doses).

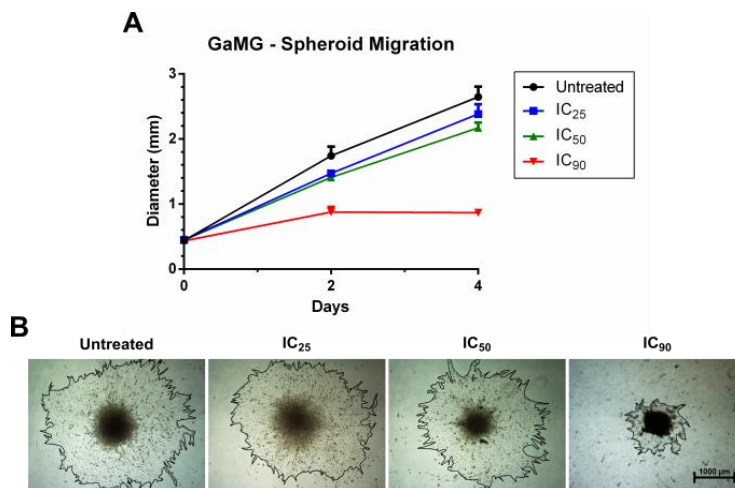


**Figure 4.32** Migration assay of GaMG spheroids. **A)** Growth curve for the migration diameter (in mm) for untreated and treated tumor spheroids over a period of four days. Mean  $\pm$  SD. **B)** Images obtained on the last day (day 4) of the migration pattern. Scale bar = 1000  $\mu$ m.

For the GaMG cell line, cabozantinib inhibited the migration out of the tumor at the two highest doses (**Figure 4.32**) (IC<sub>50</sub> -  $p \leq 0.05$ ; IC<sub>90</sub> -  $p \leq 0.01$ ).

## 4.8 CLSM Evaluation of Tumor Spheroids

Confocal laser scanning microscopy was carried out on LIVE/DEAD<sup>®</sup> stained spheroids from the GaMG cell line. Images were obtained using a 20 $\times$  objective.

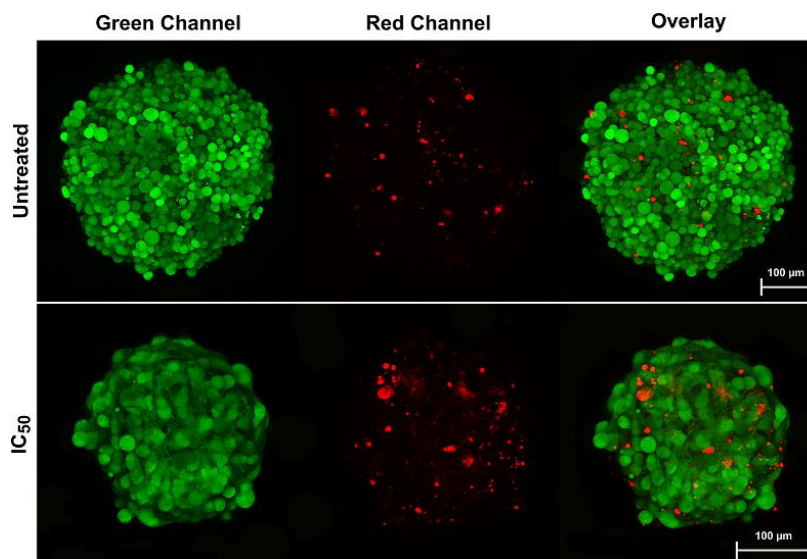


**Figure 4.33** Representative confocal scanning microscopy images of the GaMG spheroids. Untreated spheroid (top) and IC<sub>50</sub> treated (bottom). Live cells to the left (calcein AM detection in the green channel), dead cells in the middle (EthD-1 detection in the red channel), an overlay of the two images to the right. Scale bars = 100  $\mu$ m.

The confocal scanning images revealed a difference in the cellular composition of the two spheroids (**Figure 4.33**). The untreated one was considerably larger in size, and the treated one contained more dead cells (122) compared to the untreated spheroid (67). Cellular shape and morphology also varied substantially between the two spheroids, the untreated spheroid had defined round cells, while the treated spheroid carried deformed and damaged cells.

#### 4.9 Protein Analysis – Western Blot

To study the effects of cabozantinib on key proteins in signaling pathways, a western blot analysis was performed. The phosphorylation status of cell surface receptor tyrosine kinases, VEGFR-2 and MET was first examined (**Figure 4.34**). The results revealed no differences in the VEGFR-2 receptor expression after cabozantinib treatment. The protein level of MET decreased after treatment for the two cell lines U-87 MG and U-251 MG, the other cell lines appeared to be unaffected by treatment. GAPDH was used as a positive loading control.

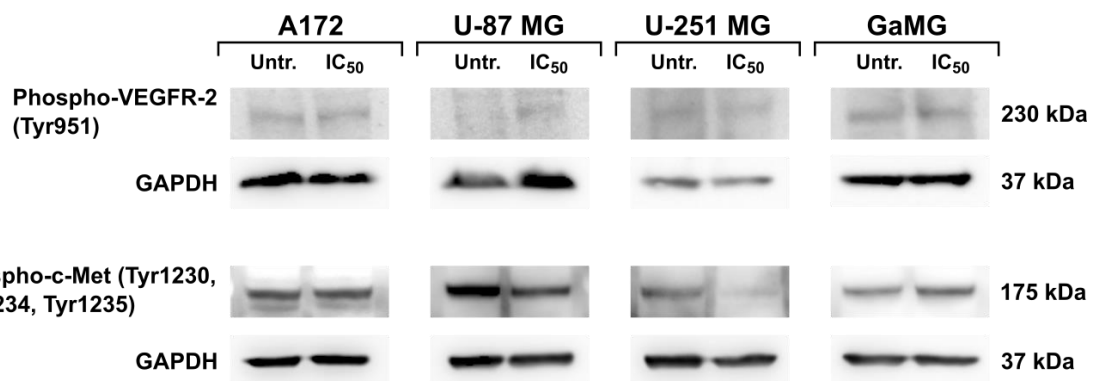


**Figure 4.34** Western blots of tyrosine kinase receptors. Untreated and IC<sub>50</sub>-treated samples for all cell lines. GAPDH used as a positive control.

Several intracellular proteins important in cell signaling, cell cycle regulation and mitochondrial metabolism was also evaluated using western blots. Both phosphorylated and regular proteins was examined (**Figure 4.35**). Phosphorylated mTOR decreased for the U-251 MG cell line. HIF-1 $\alpha$  expression decreased after treatment of cabozantinib for the U-87 MG cell line. Phosphorylated AKT was decreased for all the cell lines, however only a small difference was observed for the GaMG cell line. PTEN seemed not to be influenced by

treatment, even though a slight decrease may be observed for the U-87 MG cell line. The protein p27 generally increased in amount after treatment for all the cell lines, and p21 appeared to be unaffected (no bands were found for the U-251 MG cell line). PI 3-kinase, AKT1 and cytochrome *c* seems repellent of cabozantinib treatment. GAPDH was used as a loading control (only one is shown in the figure).

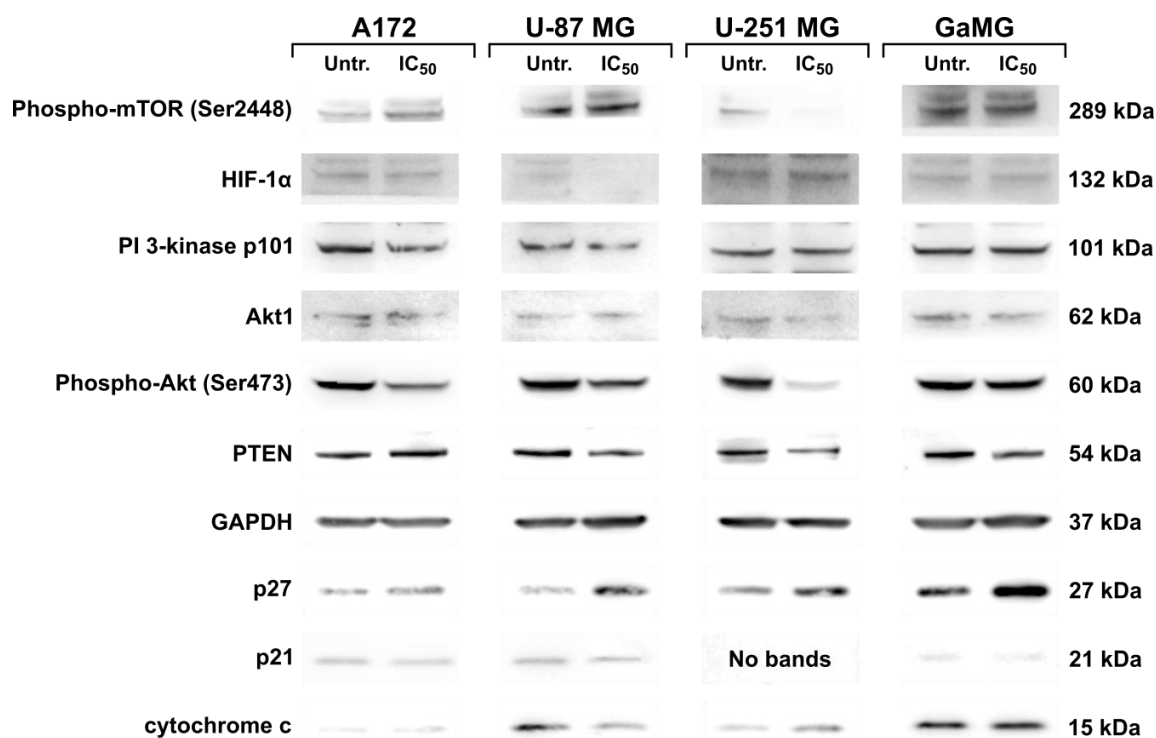


**Figure 4.35** Western blots of intracellular proteins. Untreated and IC<sub>50</sub>-treated samples for all cell lines. GAPDH used as a positive control.

#### 4.10 Long-term Treatment with Cabozantinib

To study if the cabozantinib treatment resulted in resistance development, a two-months treatment regime was carried out. One untreated flask and two treated flasks with the A172 cell line was used. The results showed no development of resistance towards the treatment. Resazurin viability assay was carried out after 5 and 10 passages (**Figure 4.36-4.37**). For the 5<sup>o</sup> experiment, the IC<sub>50</sub> doses were 13.20 μM for the untreated cells, 12.92 μM, and 16.47 μM for the treated ones. A two-tailed unpaired student *T*-test revealed no significance between any of them. Regarding the 10<sup>o</sup> experiment, IC<sub>50</sub> dose of 6.53 μM was found for the

untreated control, 7.94  $\mu\text{M}$  and 9.01  $\mu\text{M}$  was the results for the treated ones. A statistical test found no significance between these values.

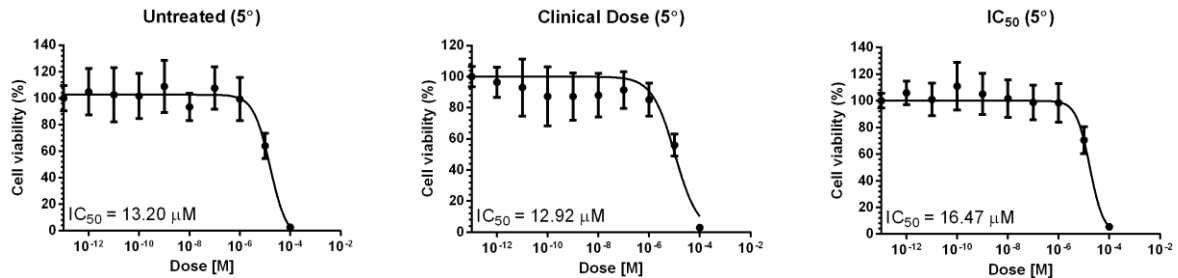


**Figure 4.36** Resazurin assay after 5 passages. The graphs shown are the most representative for each treatment regime. Mean  $\pm$  SD. The IC values presented in the figure are the mean dose of the three triplicates.

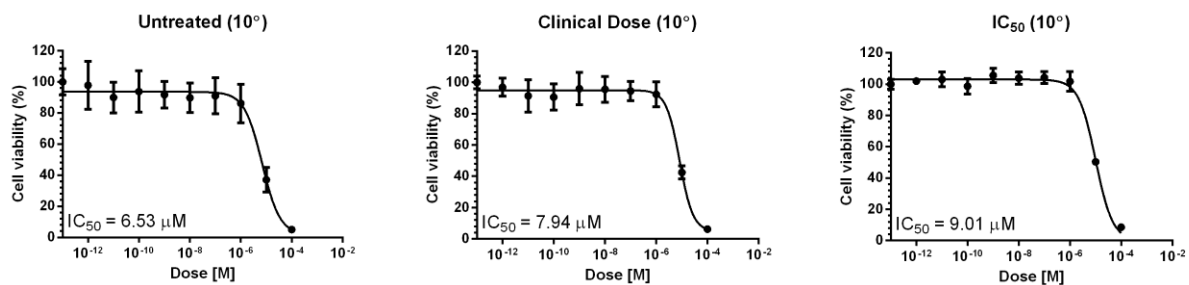


**Figure 4.37** Resazurin assay after 10 passages. The graphs shown are the most representative for each treatment regime. Mean  $\pm$  SD. The IC values presented in the figure are the mean dose of the three triplicates.

An increase in resistance can be evaluated using fold resistance (**Table 4.4**). For the two treatment regimes, the fold resistance was  $\sim 1$ , indicating that the pretreatment with cabozantinib did not result in a resistance towards cabozantinib.

**Table 4.4** Fold resistance from the resazurin assay. The fold resistance is the  $\text{IC}_{50}$  dose of the long-term treated cells divided by  $\text{IC}_{50}$  value untreated (control) cells. Clinical dose is the estimated concentration after administration of 60 mg cabozantinib.

Fold Resistance Values – Resazurin Assay		
Passage	Clinical Dose	$\text{IC}_{50}$
5°	0.98	1.25
10°	1.22	1.38

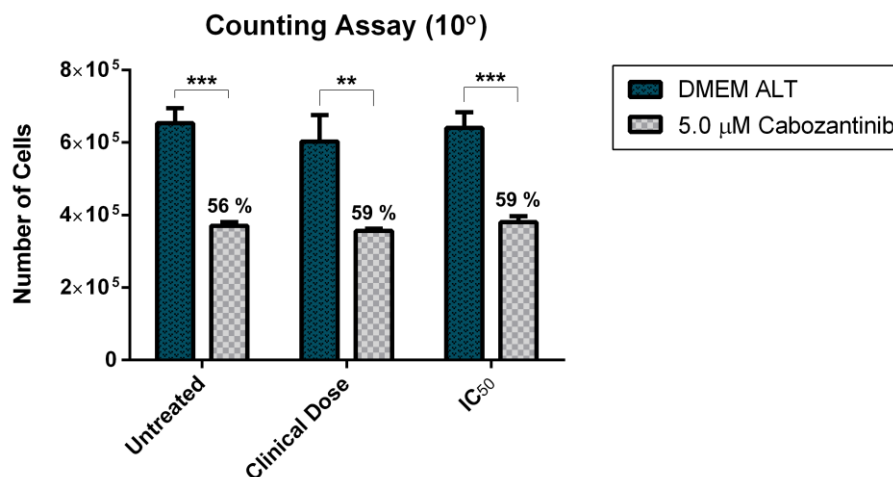


**Figure 4.38** Counting assay after 10 passages. Cells from each of the treatment regime, treated with 5.0 μM cabozantinib or DMEM ALT. Mean ± SD. (\*\* =  $p \leq 0.01$  and \*\*\* =  $p \leq 0.001$ ). The percentage (rounded off to the closest integer) represent the share of 5.0 μM treated cells in relation to the DMEM ALT sample.

To substantiate the findings, a counting assay after 10 passages was performed. Cells from all the three treatment regimens were counted after a single 5.0 μM dose of cabozantinib. The results illustrate that the drug worked equally effective, irrespective of pretreatment or not (**Figure 4.38**). A two-tailed unpaired student *T*-test revealed significance for all three, 5.0 μM cabozantinib compared against DMEM ALT. Untreated  $p \leq 0.001$ , clinical dose  $p \leq 0.01$  and IC<sub>50</sub>  $p \leq 0.001$ . The cell survival was 56.6 % for the untreated cells, 59.1 % for the clinical dose and 59.4 % for the IC<sub>50</sub>. A statistical test revealed no significance comparing the three 5.0 μM treated samples against each other, and the three DMEM ALT samples against each other.

## 5. Discussion

Among the malignant primary brain tumors, glioblastoma is the most frequently occurring and carries the poorest prognosis. The disease remains as an unsolved mystery to modern medicine. Despite improvements in treatment regimens, the median survival rate is no more than 14.6 months [11]. The incidence of patients diagnosed with a glioblastoma tumor is rising, and is proposed to rise even more in the future [109]. An up-and coming therapeutic approach is the role of receptor tyrosine kinases. These cell surface receptors are coupled with important signaling pathways and monitor functions like cell proliferation, migration and angiogenic regulation, among others [31]. Cabozantinib (XL 184) is a multiple receptor tyrosine kinase inhibitor, targeting MET, VEGFR-2 and RET and possibly several other receptors [63, 64]. The drug is administrated orally, and has been approved for treatment of other neoplasms. In fact, 75 current clinical trials are using cabozantinib to evaluate its effect on malignancies including brain metastasis, metastatic melanoma, and phase I and II trials at patients with glioblastoma [110-112]. The drug was proven effective and the results seems promising. However, very little, and inadequate information is reported on the *in vitro* effects and its possible mechanism of action in glioblastoma. This was thus the aim of the current study, and we found that cabozantinib inhibited proliferation and clonogenic ability, and induced cell cycle arrest and apoptosis in glioblastoma cell lines.

### 5.1 Monolayer Viability

The results from the resazurin assay showed a dose-dependent reduction in cell viability for all four cell lines, with  $IC_{50}$  doses in the micromolar range (2-13.06  $\mu$ M) (**Figure 4.1**). The images, both bright-field and fluorescent LIVE/DEAD<sup>®</sup> substantiated the results of the resazurin assay. All the dose-response curves had a sigmoid shape in correlation to increasing doses of the drug. The fact that none of the curves reached 0 % viability after administration of 100  $\mu$ M cabozantinib indicates that the drug is not capable of completely eradicate all the tumor cells. This is possibly due to presence of some cells that are resistant to the drug, or that they are still able to metabolize resazurin despite altered cellular functions. We did not increase the dose above 100  $\mu$ M, since this would not be clinically acceptable doses due to toxicity. In a previous study it was also indicated that increasing

---

cabozantinib further above 15  $\mu\text{M}$  did not lead to a more substantial reduction of viability related to 10  $\mu\text{M}$  [113].

Several other studies have investigated the effects of cabozantinib on the cell viability. Zang et al. showed that neuroblastoma cell lines were sensitive to cabozantinib and found  $\text{IC}_{50}$  doses ranging from 1.6-16.2  $\mu\text{M}$  [114]. Neuroblastoma is also a cancer of the nervous system, and the  $\text{IC}_{50}$  doses were quite similar to what we found. The assay used by Zang and colleagues was similar to ours, the only difference was a tetrazolium dye (MTT) used instead of resazurin as an indicator of metabolic viability. Reuther and co-workers found a reduction in viability of 30-59 % in neuroendocrine tumor cells after 72 hours of treatment with 10  $\mu\text{M}$  cabozantinib [115]. The study also showed that a reduction of the viability already was present after 24 hours of treatment, indicating that the drug works rapidly after administration. Studies of non-neurological cancer have also shown effects on cell viability. Hage et al. investigated cabozantinib on pancreatic ductal adenocarcinoma (PDA) cell lines [113]. They found a reduction in viability down to 40 % after using a dose of 10  $\mu\text{M}$ . Moreover, they stated that cabozantinib does not influence the viability of non-cancerous pancreatic cells, which indicates that cabozantinib does not interfere normal healthy cells. Taking all these findings in consideration, it seems that  $\sim 10 \mu\text{M}$  reduces viability by 50 %.

## 5.2 Cell Tumorigenicity – Clonogenic Assay

The clonogenic assay showed somewhat ambiguous results (**Figure 4.10**). Cabozantinib reduced the number of colonies for all cell lines at  $\text{IC}_{50}$  and  $\text{IC}_{90}$  concentrations. This is also the case for the  $\text{IC}_{25}$  concentration regarding the GaMG cell line. For the other cell lines,  $\text{IC}_{25}$  in fact increased colony formation. The reason for this may be diverse. In the clonogenic assay, a colony is normally defined as  $\geq 50$  [116]. This definition could be used for the GaMG cells, but for the other three cell lines, most of colonies formed contained less than 50 cells (**Figure 4.6-4.9**). In these cases, a colony was defined as listed in the results. This could question the validity of the clonogenic assay on these three cell lines, since proper sized colonies were not achieved. As higher drug doses eradicated the colonies, the results were still included in this work. Difficulties in performing this assay on the U-251 MG cell line have been reported previously [90], and also here smaller colonies formed which were difficult to define. As the GaMG cell line formed large and well-defined colonies and did not

show an increase in colony formation after IC<sub>25</sub> treatment, it is plausible that the increase seen for the other cell lines is due to poor ability for colony formation. The colony formation time in our experiments was set to 7 days. In a previous study performing the clonogenic assay on glioblastoma cell lines, the number of colonies were determined after 14 days [117]. The seeding density of the cells after treatment can interfere with the results, which is why we used both  $1 \times 10^3$  and  $5 \times 10^3$  cells to evaluate the impact on the results. The experience with increasing formation of colonies after IC<sub>25</sub> treatment was applicable for both experiments. Another more alternatively explanation may be the hormesis phenomena. Hormesis is defined as a biphasic dose response which means that the outcome of a small stimulation is opposite of the intended [118]. After the cells are introduced to the drug, they try to evade its effect by increasing cell growth resulting in an overcompensation, which means that the cells suppress the inhibition by proliferation. This yields an adverse and higher response. The situation is typically present at low drug concentrations because the biphasic response will shift to its normal state when higher doses are administrated and the cells are unable to compensate. Since only the IC<sub>25</sub> dose in our experiments showed an increase in number of colonies and the drug was effective at higher concentrations, a biphasic response might therefore be present.

The clonogenic assay in general has some limitations as a tumorigenic assay [119]. The lack of normal cell to cell interactions is for instance lost in the assay since it is based on the capability of a single treated cell to form a colony. Counting the accurate number of the colonies can be difficult. It can also be a challenge to distinguish cell colonies from general clumps and debris in the wells. The crystal violet stains proteins and nucleic acids, and therefore stain remnants that can be left in the wells after wash with PBS. Despite its drawbacks, the assay is widely used in drug utilization studies, and it illustrates the capability of cabozantinib to reduce proliferation of glioblastoma cells.

### 5.3 Flow Cytometry Assays

In general, cabozantinib induced G<sub>2</sub>M arrest of the glioblastoma cell lines (**Figure 4.11-4.14**). This was in particular evident for the A172 cells, while the GaMG cell line had a small G<sub>2</sub>M arrest along with a significant increase in S phase. The capability of cabozantinibs to arrest cell cycle have been studied extensively by others. Reuther and colleagues identified a

---

G<sub>2</sub>M arrest on neuroendocrine tumor cell lines after cabozantinib treatment [115], as did Li et al. in oral squamous cell carcinoma [120]. Others have found a G<sub>1</sub> arrest in cabozantinib treated cells. Lu and co-workers discovered a significant G<sub>1</sub> arrest on acute myeloid leukemia (AML) cell lines after treatment with as little as 5 nM cabozantinib for 24 hours [121]. A G<sub>1</sub> arrest was likewise identified by Ruan et al. in papillary thyroid cancer [122]. These findings indicate that induction of cell cycle arrest by cabozantinib is dependent on cell type.

Cell cycle proteins are encoded by genes that are rapidly mutated in diverse cancer types. For the cell to pass the G<sub>1</sub> checkpoint the DNA must be undamaged, otherwise the progression will be stopped. This is regulated by several CDKs, and overall surveillance by TP53. Since *TP53* is rapidly mutated in glioblastoma, one predominant theory is that the G<sub>1</sub> checkpoint is escaped and the cells are being arrested in the G<sub>2</sub>M phase instead. The G<sub>2</sub>M checkpoint monitors the alignment of chromosomes in addition to catch up DNA replication failure, as the cell prepare for cytokinesis. This is mainly regulated by CDK1, which is normally maintained at low levels but has to be upregulated in order for the cell to complete its cell cycle [123]. In glioblastoma cells, it has been found that CDK1 are overexpressed with as much as 78.6 % [124]. This indicates that gliomas can easily pass through to cell division as the CDK1 is present at such high levels. Downregulation of CDK1 after cabozantinib treatment have been demonstrated in neuroendocrine tumor cells [115]. This strengthen our findings of a G<sub>2</sub>M arrest after cabozantinib treatment.

The size of the cells has also an impact on cell cycle regulation [125]. The exact mechanism by which cells regulate its size remains unknown. Monitoring of the cell size is of major importance in the G<sub>2</sub>M phase, since the cell is soon to be divided in two. CDK1 has also been linked to this mechanism, and it has been suggested that its activation may be involved in attaining proper cell size [125].

In this work, the dose needed to induce G<sub>2</sub>M arrest was high, as the cell cycle distribution seemed unaffected until using the IC<sub>90</sub> dose. Cells quite rarely undergoes G<sub>2</sub>M arrest as a natural mechanism, it occurs in response to regulators inducing the arrest [123]. The arrest showed in our results may possibly be linked to a downregulation of CDK1 caused by a high dose of cabozantinib. Doublettes (two individual cells clumped together during analysis) is a common problem in flow cytometry, that can influence the result of a cell cycle analysis. Excluding doublettes from single cells is therefore of great importance in determination of the

DNA amount. Gating in FL2-H vs. FL2-A reduces this problem, but remaining doublets can still be present. The GaMG cells had results differing from the other cell lines, as a rather small G<sub>2</sub>M arrest was observed and a significant increase in S phase was present. This cell line has a near triploid chromosome content [91], which may explain the higher rate of DNA replication. Bjerkvig et al. identified the cell cycle distribution of the GaMG cell line (untreated) to be 70 % G<sub>1</sub>, 16 % S and 13 % G<sub>2</sub>M [91], which is similar to our findings for this cell line.

Results from the Annexin V/PI apoptosis assay showed a dose-dependent reduction of viable (live) cells and an increase in apoptosis for all cell lines (**Figure 4.19**). The cell lines U-87 MG and U-251 MG had the highest portion of apoptotic cells, whereas the A172 and GaMG cell lines seemed more resistant. Xiang et al. also found a dose-dependent development of apoptotic cells in hepatocellular carcinoma after treatment with cabozantinib in nM concentrations [126]. Hage and co-workers found an increase in apoptosis on PDA cell lines, however some of these cell lines did not respond to cabozantinib [113]. Apoptosis is mainly induced by one of two major pathways; the death-receptor-mediated extrinsic pathway, or the mitochondria-dependent intrinsic pathway. The regulation of the relation between several members of the Bcl-2 protein family is important for the cell to evade apoptosis and is disrupted in cancer cells [127]. They are located in the outer mitochondrial membrane where pro-apoptotic proteins e.g. Bax (Bcl-2-associated X protein) and Bad (Bcl-2-associated death promoter) induces apoptosis and anti-apoptotic e.g. Bcl-2 (B-cell lymphoma 2) and Bcl-xL (B-cell lymphoma-extra large) thwart apoptosis [127]. The activity in intracellular growth factor receptor pathways PI3K/AKT/mTOR and Ras/Raf/MAPK has been linked to the Bcl-2 protein family [128]. Raf has a dual effect, with the capability of both inhibiting and promoting apoptosis [129, 130]. AKT are capable of inactivating Bad through mTOR and thus contribute to evade apoptosis [128]. Another interesting fact is that active MET interacts with the Fas receptor by prevent binding of the Fas ligand (FasL), and thereby inhibits extrinsic pathway induced apoptosis [131]. Since cabozantinib blocks the MET receptor, its ability of inducing apoptosis can thus be linked to both main apoptotic pathways.

The numbers of viable cells remaining after the treatment with 100  $\mu$ M cabozantinib do not correspond to the findings in the resazurin assay, where the proportion was much lower. The reason for this may be diverse. Different assays will attain different results, but it can also

---

implicate that cabozantinib exert inhibitory functions that are not related to apoptosis inducement.

The dead/late apoptotic population in the flow diagrams (**Figure 4.15-4.18**) are somewhat elusive and lack the distinct shape of an individual cell population. The explanation of this might be incomplete PI staining and thereby not optimal detection of this fluorochrome. FITC and PE have overlapping absorbance spectra. Some of the FITC causes a spillover into the PE channel at joint emission wavelengths. This is a drawback of using this apoptosis assay. A possible elucidation of this may be to stain one sample with Annexin V and one with PI, analyze them individually and compensate for the spillover in the PE channel. We used an unstained sample to set the gating for the stained samples. It has some limitations doing this if the stained sample differ considerably, nevertheless it is considered as the optimal gate parameter. Setting the gating is always difficult, and is a subjective process.

An inevitable problem in flow cytometry is the presence of autofluorescence, which is fluorescence emitted from molecules within unstained cells [132]. These compounds (e.g. NADH and riboflavin) have broad emission spectra (500-700 nm) when excited with a 488 nm laser, but the peak is in the green area [132]. Thus, the FITC fluorescence can be highly influenced, and to some extent this can also occur in the PE channel. Autofluorescence is directly related to cell size, as larger cells have more organelles in the cytoplasm and thus exhibit more autofluorescence. Glioblastoma cells are fairly large cells, and because of this autofluorescence can interfere with the results.

## 5.4 Mitochondrial Membrane Potential

The disruption of the mitochondrial membrane is an early event in apoptosis, as apoptotic factors are released into the cytosol [133]. To substantiate the results from the apoptosis assay, we wanted to investigate the ability of cabozantinib to obstruct the mitochondrial gradient ( $\Delta\psi$ ). The results showed an effective disruption of the mitochondrial membrane potential after treatment with cabozantinib for all the cell lines (**Figure 4.20-4.23**), as verified by both the fluorometric measurements and the images obtained. A recent study examined the relation between cabozantinib and the  $\Delta\psi$  in medullary thyroid cancer cells. Starenki et al. found that cabozantinib increased the  $\Delta\psi$ , by using a tetramethylrhodamine

ethyl ester (TMRE) flow cytometry based assay [134], which is in conflict with our findings. This indicates that cabozantinibs alteration of the  $\Delta\psi$  is cell type dependent.

It has previously been shown that inhibition of the PI3K/AKT pathway can induce apoptosis in cells when the mitochondrial membrane potential is disrupted [135]. PDGFR suppresses apoptosis by preventing mitochondrial depolarization, thus promoting carcinogenesis [136]. Receptor tyrosine kinase inhibitors should therefore be able to induce apoptosis by inhibition of PDGFR. No data until date verifies that cabozantinib works directly against PDGFR, but it is likely that other RTKs may be involved in the induction of apoptosis, since it involves the PI3K/AKT pathway [135]. Chou et al. found a depolarization of  $\Delta\psi$  in correlation with apoptosis inducement after treatment with phenethyl isothiocyanate (PEITC) in glioblastoma cells [137]. The study also showed an upregulation of Bad/Bax, and a downregulation of Bcl-2/Bcl-xL alongside with a disrupted mitochondrial membrane potential, which shows the impact of  $\Delta\psi$  on apoptosis in glioblastoma cells.

An intact mitochondrion is crucial for optimal energy metabolism. The IDH enzyme is important in cell metabolism in glioblastoma. The *IDH1*<sup>R132H</sup> mutation results in production of 2-hydroxyglutarate (a possible oncometabolite) and alter the production of NADPH [138]. Oizel and colleagues examined the effects of this mutation on the  $\Delta\psi$  in the U-251 MG cell line, using the JC-1 assay after treatment with etoposide [139]. The cell line was transfected with vectors encoding wild-type or mutant form. The results from the JC-1 assay revealed a significantly higher number of healthy cells in the *IDH1*<sup>R132H</sup> mutation group compared to the wild type group. This indicates a possible hyperpolarization of the membrane in *IDH1*<sup>R132H</sup> mutated cells [139]. The role of IDH in glioblastoma is gaining vital attention, and is a field undergoing extensive research.

## 5.5 Tumor Spheroid Based Assays

One of the drawbacks using monolayer cultures for assessing drug effects is that these assays do not mimic the tumor environment *in situ*. Therefore, we carried out several experiments using tumor spheroids, as it relates more to a real cancer situation regarding cell to cell interactions, nutrient supply and oxygen levels.

---

A dose-dependent reduction in tumor spheroid size after treatment with cabozantinib was seen for all four glioblastoma cell lines (**Figure 4.28**). A general phenomenon was a size reduction observed at day 7 compared to day 0 for all treatments (**Figure 4.24-4.27**), indicating that the drug was more effective in early phases of the treatment. Further, cabozantinib effectively reduced the size of the tumor spheroids throughout the 21 days.

Hage et al. studied the effect of cabozantinib on pancreatic tumor spheroids and found an efficient dose-dependent reduction of size after administration of 5-, 7.5- and 10  $\mu\text{M}$  doses [113]. Pancreatic spheroids have a rather different morphology compared to glioblastoma spheroids, with spheroids looking like a cluster of grapes, and not a compact round tumor. Nevertheless, the study supports our findings of significant tumor growth inhibition.

The size of the tumor spheroid at the start of the treatment period is essential. If the spheroid is too big and the growth curve starts to flatten during the experiment, it is hard to predict whether this is due to the drug or if the spheroid has reached its maximum size. It is therefore important to use the tumor spheroids while they are in a growing state. Carlsson and colleagues investigated the growth of spheroids made from the U-251 MG cell line [140]. They found that the spheroids (200  $\mu\text{m}$  in diameter at initiation) could be cultured for at least 35 days before the growth curve reached its top point and started to flatten.

The results from the migration assay also showed a dose-dependent reduction of migrating tumor cells out of the spheroid after treatment of cabozantinib for all cell lines (**Figure 4.29-4.32**). The influence of cabozantinib on migrating glioblastoma cells have been evaluated in tumor spheroids from the E98 xenograft model. Navis et al. found a significant retaining of migration in E98 spheroids after treatment with 1  $\mu\text{M}$  cabozantinib and almost complete inhibition after 10  $\mu\text{M}$  [141]. In a combination study with dasatinib and cabozantinib on diffuse intrinsic pontine glioma (DIPG) cell lines, Truffaux and co-workers discovered a significant reduction in migration after treatment with 0.1  $\mu\text{M}$  dasatinib and 0.1  $\mu\text{M}$  cabozantinib, compared to dasatinib alone [142]. In addition, Xiang et al. found a considerable reduction of migration in hepatocellular carcinoma after treatment with 0.1  $\mu\text{M}$  cabozantinib [126]. These results reflect ours of effective inhibition of migration by cabozantinib. The latter two studies used a monolayer wound-healing assay, which may explain the low doses necessary to inhibit migration, as a higher concentration might be necessary for affecting cell migration from spheroids.

Higher drug doses were needed in our assays to suppress migration of the U-87 MG and GaMG cell lines, which may be related to tumor spheroid size. The spheroids from these two cell lines were noticeable larger, and should likely have been made smaller as necrosis tends to arise in tumor spheroids reaching 400-600  $\mu\text{m}$  [143], which may inhibit the response to drug treatment. In glioblastoma, necrosis is always present and works as a hallmark for this tumor type [14]. Ahn and colleagues investigated the influence of necrosis on the migration of glioblastoma cells. They discovered that necrotic cells stimulated the surrounding cells to increase migration, through upregulation of IL-8 (interleukin 8) via NF- $\kappa$ B and AP-1 (activator protein 1) [144]. The IL-8 positive glioblastoma cells were primarily located in the boundary between the necrotic and viable tumor cells, indicating that the regulation takes place in this rim. This may explain why the U-87 MG and GaMG cell lines were more resistant to treatment in this study.

The confocal microscopy examination of LIVE/DEAD<sup>®</sup> stained tumor spheroids from the GaMG cell line revealed an appreciable difference in morphology after treatment with cabozantinib (**Figure 4.33**), with reduction in spheroid size and increase in the number of dead cells after treatment. However, some of the dead cells may have been lost when transferring the spheroids to the coverglass before the microscopy study was performed.

## 5.6 Western Blot

The western blot showed no effect of cabozantinib treatment on the phosphorylated (active) VEGFR-2 (**Figure 4.34**). No band appeared of the untreated U-87 MG cell line. The GAPDH was also diffuse for this sample, indicating that something had gone wrong rather than the protein was not present, as a band appeared in the treated protein sample. VEGFR-2 is mostly expressed on endothelial cells, where the expression rate is regulated by the glioblastoma microenvironment [145]. The receptor is also found to be expressed on the glioblastoma cells themselves in some tumors [146]. Navis et al. found a reduction of phospho-VEGFR-2 in the xenograft derived E89 glioblastoma cells after treatment with 10  $\mu\text{M}$  cabozantinib [141]. They also treated the cells with 10 ng/mL VEGF, which may explain the differences between their and our results. Tumor cells upregulate and release VEGF as a response to hypoxia. A monolayer of cells is well supplied with oxygen, and thereby the activity of VEGF is kept at a minimum. As the antibody detects an active (phosphorylated)

---

VEGFR-2, we may not expect to detect the receptor, as it is likely not stimulated. We did however identify that the receptor was present in all four cell lines.

The MET receptor decreased its activity after treatment with cabozantinib for the U-87 MG and U-251 MG cell lines, while the other two cell lines seemed unaffected (**Figure 4.34**). Navis and colleagues also investigated the status of MET and found a complete inhibition of the receptor after treatment with 0.5  $\mu$ M cabozantinib on xenograft derived glioblastoma cells [141]. The status of MET and its relation to MET inhibitors in different glioblastoma cell lines including A172 and U-87 MG, have been thoroughly investigated by Zhang et. al [147]. They discovered a slightly larger portion of MET and a considerably greater HGF contribution in the U-87 MG cell line compared to A172. The study also demonstrated that sensitivity to MET kinase inhibitor correlated with co-expression of HGF. This indicates that there is a difference in MET mediated activity dependent on cell line, and can thus explain why U-87 MG responded to cabozantinib while A172 remained latent.

We further investigated the state of multiple intracellular proteins by western blot (**Figure 4.35**). Phospho-mTOR revealed divisive results, as a downregulation was seen in U-251 MG after treatment, whereas the protein was upregulated in A172 and U-87 MG. The implication of mTOR in glioblastoma signaling is not fully understood. The function of mTOR is carried out through two complexes: mTORC1 and mTORC2 [148]. Hyperactivation of mTOR signaling is reported to occur in most glioblastoma tumors [149]. mTOR strongly interacts with PI3K/AKT signaling via mTORC1 and mTORC2. Our results showed that the AKT receptor was affected by cabozantinib, as all the cell lines decreased its amount of AKT after treatment.

Western blot of both phosphorylated and unphosphorylated AKT were performed, and no prominent results appeared for the native AKT. In addition, no results were obtained on the PI3K protein, showing the importance of also using antibodies against phosphorylated residues. It has been shown that mTORC2 can activate AKT by phosphorylation of ser473 [148]. The phospho-Akt antibody we used was directed against this ser473 residue. As the results of inhibited AKT was strongest for the U-251 MG cell line, the same cell line that also showed downregulation of mTOR certifies the influence of mTORC2. Navis et al. also identified a downregulation of AKT after treatment of cabozantinib in a xenograft glioblastoma cell line [141], which corroborate our statement that AKT is influenced.

HIF-1 $\alpha$  was investigated, however no considerable differences after cabozantinib treatment was found, although a slight downregulation could be seen for the U-87 MG cell line. This however verifies our findings on VEGFR-2, as VEGF is likely not present at substantial levels to activate the receptor.

The tumor suppressor PTEN negatively regulates protein kinase signaling in the PI3K/AKT/mTOR pathway, and *PTEN* is rapidly mutated in most glioblastomas, thus contributing to carcinogenesis [150]. It has been shown that expression of VEGFR-2 on the glioma cells induce treatment resistance in PTEN deficient glioblastomas [146]. Therefore, we evaluated changes in PTEN after treatment with cabozantinib, but the results showed no differences, likely because the antibody was not directed against mutated PTEN.

We also investigated the state of the cyclin-dependent kinase inhibitors p21 and p27. Whereas p21 remained unaffected by cabozantinib treatment, we interestingly found that p27 was upregulated for all cell lines. p27 (fully named p27<sup>Kip1</sup>) belongs to the Cip/Kip family and negatively regulates CDKs in the cell cycle, and also inhibits cell proliferation and invasion in glioblastoma [151]. The mechanism by which p27 can be upregulated in glioblastoma have previously been investigated [128, 152]. Cathepsin B and its receptor urokinase plasminogen activator (uPAR) are frequently overexpressed in glioblastoma. When they are knocked down, the expression of p27 is upregulated through downregulation of the signaling pathways [152]. The two major actors are extracellular signal-regulated kinase (ERK; same protein as MAPK) and AKT, as they are both downregulated when p27 expression is induced. The induction is mediated by transcription factors in the forkhead box factor (FOX) family [128]. In addition, it has also been shown that phosphorylated- AKT and proto-oncogene tyrosine kinase sarc (SRC) are important for degradation of p27 [153]. Our findings of a downregulation of AKT after cabozantinib treatment encapsulates the role of p27. Whether cabozantinib interferes with uPAR is unknown, but the role of downregulation of AKT for p27 induction and active AKT for p27 degradation is essential. The regulation of p27 is important in all phases of cell cycle regulation, and it has been shown that p27 deficiency debilitate G<sub>2</sub>M arrest [154]. This reflects our findings that cabozantinib induces G<sub>2</sub>M arrest and upregulates p27.

Cytochrome *c* is an essential enzymatic complex in the inner mitochondrial membrane where it is involved in crucial functions like generation of the  $\Delta\psi$  through oxidative

---

phosphorylation in the electron transport chain, as well as regulation of apoptosis [155]. Apoptosis can be induced by release of cytochrome *c* from the mitochondria, regulated by members of the Bcl-2 protein family [156]. Thus, we evaluated the status of cytochrome *c* after treatment with cabozantinib. No changes were observed, apart from a possible small downregulation in the U-87 MG cell line. This might be because our antibody did not distinguish between mitochondrial bound- and cytosolic cytochrome *c*. The pro-apoptotic factors Bad and Bax are essential in the mitochondrial membrane. AKT are capable of inactivating Bad through mTOR and thus contribute to evading of apoptosis [128]. Bax has a similar effect and we therefore did western blot against Bax, but no bands appeared and consequently it was excluded from the results.

## 5.7 Long-term Treatment with Cabozantinib

Resistance development towards RTK inhibitors is unfortunately a common and aggravating problem in cancer treatment. Cancer cells tend to evade the effect of the drug by carry out carcinogenesis through other RTKs or modulate the intracellular signaling pathways in order to maintain its aggressive growth rate [157]. The A172 cell line did not show any sign of resistance development after 5 or 10 passages with various doses of cabozantinib, as verified by resazurin assay (**Figure 4.36-4.37**). When comparing the result after the 5<sup>o</sup> and 10<sup>o</sup> measurements, there was a difference in the IC<sub>50</sub> doses, likely due to biological interference rather than any drug induced difference. If cabozantinib had caused these changes, a change between the treated samples and the untreated control would have been observed. To verify our findings from the resazurin assay we carried out a simple counting assay, but no resistance was found (**Figure 4.38**).

Resistance development after cabozantinib treatment have previously been investigated for pancreatic cancer. Hage and co-workers found a low level of resistance development after two weeks treatment with increasing doses of cabozantinib [113]. However, this study used a considerable shorter treatment period and higher doses of cabozantinib than we did. It would be interesting to measure several other parameters as well in our long-term treated cells, in addition to cell viability such as apoptosis and cell cycle arrest, to assess if these functions have been altered.

## 5.8 Summary and Future Perspectives

This work shows that cabozantinib inhibited the viability of glioblastoma cells in a dose-dependent manner with  $IC_{50}$  doses in the micromolar range. Cabozantinib affected the tumorigenicity, although an increase in proliferation was observed for some cell lines at lower drug dose. The cells were arrested in the G<sub>2</sub>M phase of the cell cycle when a high dose of cabozantinib was administered. The drug induced apoptosis in a dose-dependent increase for all cell lines even though a considerable number of cells remained viable after treatment. Cabozantinib disrupted the mitochondrial membrane by depolarizing the membrane gradient, indicating metabolic disturbances leading to apoptosis. The tumor spheroids responded in a dose-dependent manner by inhibition of growth and migrating tumor cells, and morphological changes were seen. In general, the assays involving tumor spheroids demonstrated the clearest results, which is a good thing since it is a more realistic *in vitro* model than cell monolayers. Western blot analysis of the RTKs did not disclose clear results of inhibition, possibly due to lack of adequate activation in our *in vitro* model. We revealed that many intracellular proteins were altered, including AKT, which suggest that the PI3K/AKT pathway is inhibited. Long-term treatment of glioblastoma cells with cabozantinib did not result in treatment resistance.

To conclude, our results state that cabozantinib is an effective agent for inhibiting carcinogenic functions of glioblastoma cells *in vitro*. Based on this and the aspects discussed above, the overall aims for this thesis are considered achieved.

In further studies, several of the assays should be redone. The western blot of the cell surface receptors should be repeated, and also to study whether VEGFR-2 is activated either by adding VEGF to the growth medium or incubating the cells in a hypoxic environment. As glioblastomas are highly vascular tumors, the role of VEGFR-2 is important. One could also prepare cell lysates based on tumor spheroids rather than monolayers, as both intra- and extracellular signaling are better illustrated under such conditions. A longer colony formation period should be applied for the clonogenic assay, to see if the results gained more clearance. The flow cytometry based apoptosis assay should also be redone, possibly by increasing the amount of PI as our staining might have been inadequate.

---

As cabozantinib is a multiple RTK inhibitor, it could be interesting to study if the drug is able to inhibit other receptors on glioma cells as well, e.g. AXL (tyrosine-protein kinase receptor UFO), which is involved in the aggressiveness of glioblastoma by being constitutively phosphorylated [158]. Additional western blots against the CDK1, ERK/MAPK, mTORC1/mTORC2 and possible various caspase enzymes would substantiate the findings we obtained.

Neuronal stem cells are gaining increasingly attention, since it is predicted that much of the tumorigenic traits are located here. In fact, it has been identified that the A172, U-87 MG and U-251 MG cell lines all contain some proportion of stem cells, as they all express the CD133 NSC marker [159]. It has been reported that cabozantinib is able to reduce the expression of CD133 in pancreatic cancer, thus indicating that the drug can eliminate stem cell features [113]. Assessing the inhibitory effect of cabozantinib on a pure glioblastoma stem cell lineage would of these reasons be of interest.

The MET receptor is partly responsible for the stem cell-like phenotype in glioblastoma, implicating resistance to treatment. It has been shown that resistance against bevacizumab treatment is mediated by overexpression of MET [160]. Therefore, *in vitro* and *in vivo* studies of combining cabozantinib and bevacizumab could be of clinical relevance.

We used free base cabozantinib in this study. In the clinic, it is administered as a malate salt and metabolized in the liver, resulting in less active metabolites which probably carry out the inhibitory effect [60]. It is therefore necessary to supply our findings with *in vivo* experiments to outline the effect of the drug in a metabolizing environment.

Finally, it is possible to radiolabel cabozantinib, which opens many possibilities of evaluating *in vivo* drug efficiency using PET/CT. One can thus easily monitor drug distribution, and evaluate its ability to penetrate the BBB and exert effects on intracranial tumors.

## References

1. Chan, V., C. Xiong, and A. Colantonio, *Patients With Brain Tumors: Who Receives Postacute Occupational Therapy Services?* The American Journal of Occupational Therapy, 2015. **69**(2): p. 1-6.
2. Madhusudanan, P., S. Reade, and S.A. Shankarappa, *Neuroglia as targets for drug delivery systems: A Review*. Nanomedicine: Nanotechnology, Biology, and Medicine, 2016.
3. Ho, V.K.Y., et al., *Changing incidence and improved survival of gliomas*. European Journal of Cancer, 2014.
4. Sukhdeo, K., D. Hambardzumyan, and Jeremy n. Rich, *Glioma Development: Where Did It All Go Wrong?* Cell, 2011. **146**(2): p. 187-188.
5. Iarc, et al., *WHO Classification of Tumours of the Central Nervous System*. 4th ed. ed. WHO Classification of Tumours, v.1. 2007, Geneva: World Health Organization.
6. Louis, D.N., et al., *The 2016 World Health Organization Classification of Tumors of the Central Nervous System: a summary*. Acta Neuropathologica, 2016. **131**(6): p. 803-820.
7. Ray, S.K., *Glioblastoma*. 2009, Dordrecht: Springer. p. 43, 78-79, 95, 100-102.
8. Ostrom, Q.T., et al., *CBTRUS Statistical Report: Primary Brain and Central Nervous System Tumors Diagnosed in the United States in 2006-2010*. Neuro-Oncology, 2013. **15**(suppl2): p. ii1-ii56.
9. Hayat, M.A. and M.A. Hayat, *Tumors of the Central Nervous System, Volume 8 : Astrocytoma, Medulloblastoma, Retinoblastoma, Chordoma, Craniopharyngioma, Oligodendroglioma, and Ependymoma*. Tumors of the Central Nervous System, Volume 8 : Astrocytoma, Medulloblastoma, Retinoblastoma, Chordoma, Craniopharyngioma, Oligodendroglioma, and Ependymoma. 2012, Dordrecht: Springer. p. 49.
10. Woehrer, A., L. Bauchet, and J.S. Barnholtz-Sloan, *Glioblastoma survival: has it improved? Evidence from population-based studies*. Current opinion in neurology, 2014. **27**(6): p. 666.
11. Stupp, R., et al., *Radiotherapy plus Concomitant and Adjuvant Temozolomide for Glioblastoma*. The New England Journal of Medicine, 2005. **352**(10): p. 987-996.

- 
12. Sant, M., et al., *Survival of European patients with central nervous system tumors*. International Journal of Cancer, 2012. **131**(1): p. 173-185.
  13. Preusser, M., et al., *Current concepts and management of glioblastoma*. Annals of Neurology, 2011. **70**(1): p. 9-21.
  14. Ricard, D., et al., *Primary brain tumours in adults*. The Lancet, 2012. **379**(9830): p. 1984-1996.
  15. Behin, A., et al., *Primary brain tumours in adults*. The Lancet, 2003. **361**(9354): p. 323-331.
  16. Chayer, C. and M. Freedman, *Frontal lobe functions*. Current Neurology and Neuroscience Reports, 2001. **1**(6): p. 547-552.
  17. Abd-El-Barr, M., et al., *Effect of disease and recovery on functional anatomy in brain tumor patients: insights from functional MRI and diffusion tensor imaging*. 2013, Future Medicine Ltd: London. p. 333-346.
  18. Zhao, Z.-X., et al., *A new method to classify pathologic grades of astrocytomas based on magnetic resonance imaging appearances*. Neurology India, 2010. **58**(5): p. 685-690.
  19. Abdelzahe, E. *CNS tumor, Astrocytic tumors, Glioblastoma multiforme*. 2013 [cited 2017 01.29]; Available from: <http://www.pathologyoutlines.com/topic/cnstumorglioblastoma.html>.
  20. Sheila, K.S., et al., *Cancer stem cells in nervous system tumors*. Oncogene, 2004. **23**(43): p. 7267.
  21. Sheila, K.S., et al., *Identification of human brain tumour initiating cells*. Nature, 2004. **432**(7015): p. 396.
  22. Shideng, B., et al., *Glioma stem cells promote radioresistance by preferential activation of the DNA damage response*. Nature, 2006. **444**(7120): p. 756.
  23. Ohgaki, H. and P. Kleihues, *Epidemiology and etiology of gliomas*. Acta Neuropathologica, 2005. **109**(1): p. 93-108.
  24. Nygaard, R., et al., *Second Malignant Neoplasms in Patients Treated for Childhood Leukemia: A Population-based Cohort Study from the Nordic Countries*. Acta Pædiatrica, 1991. **80**(12): p. 1220-1228.

- 
25. Brüstle, O., et al., *Primitive neuroectodermal tumors after prophylactic central nervous system irradiation in children. Association with an activated K- ras gene.* Cancer, 1992. **69**(9): p. 2385-2392.
  26. Lahkola, A., et al., *Mobile phone use and risk of glioma in 5 North European countries.* International Journal of Cancer, 2007. **120**(8): p. 1769-1775.
  27. Smeitink, J., *Metabolism, Gliomas, and IDH1.* The New England Journal of Medicine, 2010. **362**(12): p. 1144-1145.
  28. Reni, M., et al., *Central nervous system gliomas.* Critical Reviews in Oncology / Hematology, 2017. **113**: p. 213-234.
  29. Chaurasia, A., et al., *Immunohistochemical Analysis of ATRX, IDH1 and p53 in Glioblastoma and Their Correlations with Patient Survival.* Journal of Korean Medical Science, 2016. **31**(8): p. 1208-1214.
  30. Mao, H., et al., *Deregulated signaling pathways in glioblastoma multiforme: molecular mechanisms and therapeutic targets.* Cancer investigation, 2012. **30**(1): p. 48.
  31. Carrasco-García, E., M. Saceda, and I. Martínez-Lacaci, *Role of receptor tyrosine kinases and their ligands in glioblastoma.* Cells, 2014. **3**(2): p. 199.
  32. Aldape, K., et al., *Glioblastoma: pathology, molecular mechanisms and markers.* Pathology and Mechanisms of Neurological Disease, 2015. **129**(6): p. 829-848.
  33. Wang, E., et al., *The Role of Factor Inhibiting HIF (FIH-1) in Inhibiting HIF-1 Transcriptional Activity in Glioblastoma Multiforme.* PLoS One, 2014. **9**(1): p. e86102.
  34. Zagzag, D., et al., *Expression of hypoxia-inducible factor 1alpha in brain tumors: association with angiogenesis, invasion, and progression.* Cancer, 2000. **88**(11): p. 2606.
  35. Livio, T., B. Andrea, and M.C. Paolo, *MET signalling: principles and functions in development, organ regeneration and cancer.* Nature Reviews Molecular Cell Biology, 2010. **11**(12): p. 834.
  36. Boccaccio, C. and P. Comoglio, *The MET Oncogene in Glioblastoma Stem Cells: Implications as a Diagnostic Marker and a Therapeutic Target,* in Cancer Res. 2013. p. 3193-3199.

- 
37. Rückert, F., et al., *RET -protooncogene variants in patients with sporadic neoplasms of the digestive tract and the central nervous system*. *Clinical and Molecular Gastroenterology and Surgery*, 2011. **26**(7): p. 835-840.
  38. Pucci, B., M. Kasten, and A. Giordano, *Cell Cycle and Apoptosis*. *Neoplasia*, 2000. **2**(4): p. 291-299.
  39. Velpula, K., et al., *Cell cycle regulation of glioblastoma progression by cord blood stem cells is mediated by downregulation of cyclin D1*. *Cancer Res.*, 2011. **71**(8 Supplement).
  40. Zolota, V., et al., *Expression of cell cycle inhibitors p21, p27, p14 and p16 in gliomas. Correlation with classic prognostic factors and patients' outcome*. *Neuropathology*, 2008. **28**(1): p. 35-42.
  41. Kraus, A., et al., *Aberrant p21 regulation in radioresistant primary glioblastoma multiforme cells bearing wild-type p53*. *Journal of neurosurgery*, 2000. **93**(5): p. 863.
  42. Ding, Q., et al., *P27(Kip) and cyclin D1 are necessary for focal adhesion kinase regulation of cell cycle progression in glioblastoma cells propagated in vitro and in vivo in the scid mouse brain*. *J. Biol. Chem.*, 2005. **280**(8): p. 6802-6815.
  43. Sanai, N., et al., *An extent of resection threshold for newly diagnosed glioblastomas*. *Journal of neurosurgery*, 2011. **115**(1): p. 3.
  44. Lobo, F.A., M. Wagemakers, and A.R. Absalom, *Anaesthesia for awake craniotomy*. 2016. p. 740-744.
  45. Alexander, B., K. Ligon, and P. Wen, *Enhancing radiation therapy for patients with glioblastoma*. *Expert Review of Anticancer Therapy*, 2013. **13**(5): p. 569-81.
  46. Klein, E.E., et al., *Technical Advances in Oncology Outside of Radiation Medicine*. 2016. p. 1323-1326.
  47. Wenger, C., et al., *Improving Tumor Treating Fields Treatment Efficacy in Patients With Glioblastoma Using Personalized Array Layouts*. *International Journal of Radiation Oncology, Biology, Physics*, 2016. **94**(5): p. 1137-1143.
  48. Huncharek, M., B. Kupelnick, and D. Bishop, *Platinum analogues in the treatment of recurrent high grade astrocytoma*, in *Cancer Treat. Rev.* 1998. p. 307-316.
  49. Wang, Y., et al., *Continuous dose-intense temozolomide and cisplatin in recurrent glioblastoma patients*. *Medicine*, 2017.

- 
50. Capdevila, L., et al., *Neoadjuvant cisplatin plus temozolomide versus standard treatment in patients with unresectable glioblastoma or anaplastic astrocytoma: a differential effect of MGMT methylation*. *Journal of Neuro-Oncology*, 2014. **117**(1): p. 77-84.
  51. Fine, H.A., *Bevacizumab in Glioblastoma — Still Much to Learn*. *The New England Journal of Medicine*, 2014. **370**(8): p. 764-765.
  52. Wang, X., et al., *Pharmacokinetics and tissue distribution model of cabozantinib in rat determined by UPLC–MS/MS*. *Journal of Chromatography B*, 2015. **983-984**: p. 125-131.
  53. *Exelixis receives fast track designation for cabozantinib from US FDA*. M2 Pharma, 2015.
  54. *FDA Approves Cometriq in MTC*. *J. Nucl. Med.*, 2013. **54**(2): p. 15N-15N.
  55. Information., N.C.f.B. and P.C. Database. *PubChem Compound Database; CID=25102847*. 2008 [cited 2017 01.24]; Available from: <https://pubchem.ncbi.nlm.nih.gov/compound/25102847>
  56. Palmer, A.M., *The blood–brain barrier*. 2010. p. 1-2.
  57. De Boer, R.H. and C.D. Hart, *Profile of cabozantinib and its potential in the treatment of advanced medullary thyroid cancer*. *OncoTargets and Therapy*, 2013. **2013**(default): p. 1-7.
  58. *Clinical Research - Clinical Trials and Studies; New Findings from Samuel Oschin Comprehensive Cancer Institute in Clinical Trials and Studies Provides New Insights (Intracranial Activity of Cabozantinib in MET Exon 14-Positive NSCLC with Brain Metastases)*. *Cancerweekly Plus*, 2017: p. 682.
  59. Pajouhesh, H. and G. Lenz, *Medicinal chemical properties of successful central nervous system drugs*. *NeuroRX*, 2005. **2**(4): p. 541-553.
  60. Lacy, S., et al., *Metabolism and Disposition of Cabozantinib in Healthy Male Volunteers and Pharmacologic Characterization of Its Major Metabolites*. *Drug metabolism and disposition: the biological fate of chemicals*, 2015. **43**(8): p. 1190.
  61. Kurzrock, R., et al., *Activity of XL184 (Cabozantinib), an Oral Tyrosine Kinase Inhibitor, in Patients With Medullary Thyroid Cancer*. *J. Clin. Oncol.*, 2011. **29**(19): p. 2660-2666.

- 
62. Saal, C. and A. Becker, *Pharmaceutical salts: A summary on doses of salt formers from the Orange Book*. European Journal of Pharmaceutical Sciences, 2013. **49**(4): p. 614-623.
  63. Sennino, B., et al., *Suppression of tumor invasion and metastasis by concurrent inhibition of c-Met and VEGF signaling in pancreatic neuroendocrine tumors*. Cancer discovery, 2012. **2**(3): p. 270.
  64. Jahangiri, A., et al., *Gene Expression Profile Identifies Tyrosine Kinase c-Met as a Targetable Mediator of Antiangiogenic Therapy Resistance*. Clin. Cancer Res., 2013. **19**(7): p. 1773-1783.
  65. Carmen, B., et al., *Met, metastasis, motility and more*. Nature Reviews Molecular Cell Biology, 2003. **4**(12): p. 915.
  66. Yakes, F.M., et al., *Cabozantinib (XL184), a novel MET and VEGFR2 inhibitor, simultaneously suppresses metastasis, angiogenesis, and tumor growth*. Molecular cancer therapeutics, 2011. **10**(12): p. 2298.
  67. Xin, X., et al., *Hepatocyte Growth Factor Enhances Vascular Endothelial Growth Factor-Induced Angiogenesis in Vitro and in Vivo*. The American Journal of Pathology, 2001. **158**(3): p. 1111-1120.
  68. Waltenberger, J., et al., *Different signal transduction properties of KDR and Flt1, two receptors for vascular endothelial growth factor*. J Biol Chem, 1994. **269**(43): p. 26988-95.
  69. Ferrara, N., H.-P. Gerber, and J. LeCouter, *The biology of VEGF and its receptors*. Nature Medicine, 2003. **9**(6): p. 669.
  70. Plate, K., et al., *Vascular endothelial growth factor is a potential tumour angiogenesis factor in human gliomas in vivo*. Nature, 1992. **359**(6398): p. 845-8.
  71. Stommel, J.M., et al., *Coactivation of receptor tyrosine kinases affects the response of tumor cells to targeted therapies*. Science (New York, N.Y.), 2007. **318**(5848): p. 287.
  72. Administration, U.S.F.D. *CABOMETYX™ (cabozantinib) tablets, for oral use Initial U.S. Approval: 2012* Revised: 04/2016 [cited 2017 05.18]; Available from: [https://www.accessdata.fda.gov/drugsatfda\\_docs/label/2016/208692s0001bl.pdf](https://www.accessdata.fda.gov/drugsatfda_docs/label/2016/208692s0001bl.pdf).
  73. Shi, H.-C., et al., *In vitro isolation and cultivation of rabbit tracheal epithelial cells using tissue explant technique*. In Vitro Cellular & Developmental Biology - Animal, 2013. **49**(4): p. 245-249.

74. Niu, N. and L. Wang, *In vitro human cell line models to predict clinical response to anticancer drugs*, in *Pharmacogenomics*. 2015. p. 273-285.
75. Allen, D.D., et al., *Cell Lines as In Vitro Models for Drug Screening and Toxicity Studies*. *Drug Development and Industrial Pharmacy*, 2005, Vol.31(8), p.757-768, 2005. **31**(8): p. 757-768.
76. McDermott, M., et al., *In vitro Development of Chemotherapy and Targeted Therapy Drug-Resistant Cancer Cell Lines: A Practical Guide with Case Studies*. *Frontiers in Oncology*, 2014. **4**.
77. Jahan-Tigh, R.R., et al., *Flow Cytometry*. *Journal of Investigative Dermatology*, 2012. **132**(10): p. 1-6.
78. Delude, R., *Flow cytometry*. *Crit. Care Med.*, 2005. **33**(12): p. S426-S428.
79. van Engeland, M., et al., *Annexin V-affinity assay: A review on an apoptosis detection system based on phosphatidylserine exposure*, in *Cytometry*. 1998. p. 1-9.
80. Cecchini, M.J., M. Amiri, and F.A. Dick, *Analysis of cell cycle position in mammalian cells*. *Journal of visualized experiments : JoVE*, 2012(59).
81. Murphy, D.B. and M.W. Davidson, *Fundamentals of Light Microscopy and Electronic Imaging*. 2nd ed. ed. *Fundamentals of Light Microscopy and Electronic Imaging*, Second Edition. 2012, Hoboken: Wiley. p. 200.
82. Stephens, D.J. and V.J. Allan, *Light microscopy techniques for live cell imaging*. *Science*, 2003. **300**(5616): p. 82.
83. Price, R. and W.G. Jerome, *Basic Confocal Microscopy*. 2011, Dordrecht: Springer. p. 3.
84. Giard, D.J., et al., *In vitro cultivation of human tumors: establishment of cell lines derived from a series of solid tumors*. *Journal of the National Cancer Institute*, 1973. **51**(5): p. 1417.
85. Kiseleva, L., et al., *A172 and T98G cell lines characteristics*. *Cell and Tissue Biology*, 2016. **10**(5): p. 341-348.
86. Ponten, J. and E.H. Macintyre, *Long term culture of normal and neoplastic human glia*. *Acta Pathol Microbiol Scand*, 1968. **74**(4): p. 465-86.
87. Allen, M., et al., *Origin of the U87MG glioma cell line: Good news and bad news*. *Sci Transl Med*, 2016. **8**(354): p. 354re3.

- 
88. Westermark, B., J. Pontén, and R. Hugosson, *DETERMINANTS FOR THE ESTABLISHMENT OF PERMANENT TISSUE CULTURE LINES FROM HUMAN GLIOMAS*. Acta Pathologica Microbiologica Scandinavica Section A Pathology, 1973. **81**(6): p. 791-805.
  89. Mark, J., et al., *Banding patterns in human glioma cell lines*. Hereditas, 1978. **87**(2): p. 243-260.
  90. Torsvik, A., et al., *U-251 revisited: genetic drift and phenotypic consequences of long-term cultures of glioblastoma cells*. Cancer Med, 2014. **3**(4): p. 812-24.
  91. Akslen, L.A., K.J. Andersen, and R. Bjerkvig, *Characteristics of human and rat glioma cells grown in a defined medium*. Anticancer Res, 1988. **8**(4): p. 797-803.
  92. Memmel, S., et al., *Cell Surface Area and Membrane Folding in Glioblastoma Cell Lines Differing in PTEN and p53 Status*.(Research Article). PLoS ONE, 2014. **9**(1): p. e87052.
  93. Zhao, Y., et al., *An Extensive Invasive Intracranial Human Glioblastoma Xenograft Model: Role of High Level Matrix Metalloproteinase 9*. The American Journal of Pathology, 2010. **176**(6): p. 3032-3049.
  94. Elhag, R., E.A. Mazzi, and K.F. Soliman, *The effect of silibinin in enhancing toxicity of temozolomide and etoposide in p53 and PTEN-mutated resistant glioma cell lines*. Anticancer Res, 2015. **35**(3): p. 1263-9.
  95. *The American Tissue Culture Collection GLIOMA TUMOR CELL PANEL 2013* [cited 2017 05.09]; Available from: <https://www.lgcstandards-atcc.org/~media/A77B5F5B2B91478B8DF4F4E9E6ABACD0.ashx>.
  96. Lonza. *MycoAlert™ Mycoplasma Detection Kit*. 2017 [cited 2017 04.04]; Available from: <http://www.lonza.com/products-services/bio-research/cell-culture-products/mycoplasma-detection-and-removal/mycoalert-mycoplasma-detection-kit.aspx>.
  97. Invitrogen. *Countess™ Automated Cell Counter User Manual 2017* [cited 2017 04.04]; Available from: <https://tools.thermofisher.com/content/sfs/manuals/mp10227.pdf>.
  98. Company, A.A.A.a.E. *Cabozantinib (XL184, BMS-907351) VEGFR2/Met/Ret/Kit/FLT//AXL inhibitor*. 2013 [cited 2017 04.04]; Available from: <http://www.apexbt.com/cabozantinib-xl184-bms-907351.html>.
  99. Riss, T.L., et al., *Cell Viability Assays*, in *Assay Guidance Manual*, G.S. Sittampalam, et al., Editors. 2004, Eli Lilly & Company and the National Center for Advancing Translational Sciences: Bethesda (MD).

- 
100. Prism, G. *GraphPad ECanything from EC50*. 2009 [cited 2017 05.07]; Available from: <http://www.graphpad.com/support/faqid/169/>.
  101. technologies, M.P.i.d. *LIVE/DEAD® Viability/Cytotoxicity Kit \*for mammalian cells\** 2005 [cited 2017 04.05]; Available from: <https://tools.thermofisher.com/content/sfs/manuals/mp03224.pdf>.
  102. Inc., S.-A. *Mitochondria Staining Kit*. Technical Bulletin 2008 [cited 2017 04.09]; Available from: <http://www.sigmaaldrich.com/content/dam/sigmaaldrich/docs/Sigma/Bulletin/cs0390bul.pdf>.
  103. Scientific, T. *General information and protocols for using theNuPAGE® electrophoresis system*. NuPAGE®Technical Guide 2010 [cited 2017 05.01]; Available from: [https://tools.thermofisher.com/content/sfs/manuals/nupage\\_tech\\_man.pdf](https://tools.thermofisher.com/content/sfs/manuals/nupage_tech_man.pdf).
  104. Mahmood, T. and P.-C. Yang, *Western blot: Technique, theory, and trouble shooting*. North American Journal of Medical Sciences, 2012. **4**(9): p. 429-434.
  105. Singh, H., et al., *U.S. Food and Drug Administration Approval: Cabozantinib for Treatment of Advanced Renal Cell Carcinoma*. Clinical cancer research : an official journal of the American Association for Cancer Research, 2016.
  106. Research, C.f.D.E.a. *Clinical Pharmacology and Biopharmaceutics Review - Cabozantinib*. 203756Orig1s000 2012 [cited 2017 04.09]; Available from: [https://www.accessdata.fda.gov/drugsatfda\\_docs/nda/2012/203756Orig1s000ClinPharmR.pdf](https://www.accessdata.fda.gov/drugsatfda_docs/nda/2012/203756Orig1s000ClinPharmR.pdf).
  107. Zhang, Y., et al., *XL-184, a MET, VEGFR-2 and RET kinase inhibitor for the treatment of thyroid cancer, glioblastoma multiforme and NSCLC*. IDrugs, 2010. **13**(2): p. 112-21.
  108. Fan, J. and I.A.M. de Lannoy, *Pharmacokinetics*. Biochemical Pharmacology, 2014. **87**(1): p. 93-120.
  109. Johnson, D., *Rising incidence of glioblastoma and meningioma in the United States: Projections through 2050*. J. Clin. Oncol., 2012. **30**(15).
  110. Schiff, D., et al., *Phase I dose escalation trial of the safety and pharmacokinetics of cabozantinib concurrent with temozolomide and radiotherapy or temozolomide after radiotherapy in newly diagnosed patients with high-grade gliomas*. Cancer, 2016. **122**(4): p. 582-587.
  111. De Groot, J., et al., *A phase II study of XL184 in patients (pts) with progressive glioblastoma multiforme (GBM) in first or second relapse*. J. Clin. Oncol., 2009. **27**(15).

- 
112. ClinicalTrials.gov. *Clinical Trials Cabozantinib*. Clinical Trials Cabozantinib 2017 [cited 2017 05.29]; Available from: <https://clinicaltrials.gov/ct2/results?term=cabozantinib&Search=Search>.
  113. Hage, C., et al., *The novel c-Met inhibitor cabozantinib overcomes gemcitabine resistance and stem cell signaling in pancreatic cancer*. *Cell Death and Disease*, 2013. **4**(5): p. e627.
  114. Zhang, L., et al., *Sensitivity of neuroblastoma to the novel kinase inhibitor cabozantinib is mediated by ERK inhibition*. *Cancer Chemotherapy and Pharmacology*, 2015. **76**(5): p. 977-987.
  115. Reuther, C., et al., *Cabozantinib and Tivantinib, but Not INC280, Induce Antiproliferative and Antimigratory Effects in Human Neuroendocrine Tumor Cells in vitro: Evidence for 'Off-Target' Effects Not Mediated by c-Met Inhibition*. *Neuroendocrinology*, 2016. **103**(3-4): p. 383.
  116. Nicolaas, A.P.F., et al., *Clonogenic assay of cells in vitro*. *Nature Protocols*, 2006. **1**(5): p. 2315.
  117. Wang, K., J.O. Park, and M. Zhang, *Treatment of glioblastoma multiforme using a combination of small interfering RNA targeting epidermal growth factor receptor and [beta]-catenin*. *Journal of Gene Medicine*, 2013. **15**(1): p. 42-50.
  118. Calabrese, E.J., I. Iavicoli, and V. Calabrese, *Hormesis*. *Human & Experimental Toxicology*, 2013. **32**(2): p. 120-152.
  119. Hoffman, R.M., *In vitro sensitivity assays in cancer: a review, analysis, and prognosis*. *J Clin Lab Anal*, 1991. **5**(2): p. 133-43.
  120. Li, D.-L., et al., *Anti-tumor activity of cabozantinib by FAK down-regulation in human oral squamous cell carcinoma*. *Bangladesh Journal of Pharmacology*, 2015. **11**(1): p. 119.
  121. Lu, J.-W., et al., *Cabozantinib is selectively cytotoxic in acute myeloid leukemia cells with FLT3-internal tandem duplication (FLT3-ITD)*. *Cancer Letters*, 2016. **376**(2): p. 218-225.
  122. Ruan, M., et al., *Iodide- and Glucose-Handling Gene Expression Regulated by Sorafenib or Cabozantinib in Papillary Thyroid Cancer*. *The Journal of Clinical Endocrinology & Metabolism*, 2015. **100**(5): p. 1771-1779.
  123. Rhind, N. and P. Russell, *Signaling pathways that regulate cell division*. *Cold Spring Harbor perspectives in biology*, 2012. **4**(10).

- 
124. Chen, H., et al., [*CDK1 expression and effects of CDK1 silencing on the malignant phenotype of glioma cells*]. *Zhonghua Zhong Liu Za Zhi*, 2007. **29**(7): p. 484-8.
  125. Jorgensen, P. and M. Tyers, *How Cells Coordinate Growth and Division*. *Current Biology*, 2004. **14**(23): p. R1014-R1027.
  126. Xiang, Q., et al., *Cabozantinib suppresses tumor growth and metastasis in hepatocellular carcinoma by a dual blockade of VEGFR2 and MET*. *Clinical cancer research : an official journal of the American Association for Cancer Research*, 2014. **20**(11): p. 2959.
  127. Wong, R., *Apoptosis in cancer: from pathogenesis to treatment*. *Journal of Experimental & Clinical Cancer Research*, 2011. **30**(1): p. 87.
  128. Chang, F., et al., *Involvement of PI3K/Akt pathway in cell cycle progression, apoptosis, and neoplastic transformation: a target for cancer chemotherapy*. *Leukemia*, 2003. **17**(3): p. 590-603.
  129. Lau, Q.C., S. Brusselbach, and R. Muller, *Abrogation of c-Raf expression induces apoptosis in tumor cells*. *Oncogene*, 1998. **16**(14): p. 1899-902.
  130. Kauffmann-Zeh, A., et al., *Suppression of c-Myc-induced apoptosis by Ras signalling through PI(3)K and PKB*. *Nature*, 1997. **385**(6616): p. 544-8.
  131. Wang, X., et al., *A Mechanism of Cell Survival: Sequestration of Fas by the HGF Receptor Met*. *Molecular Cell*, 2002. **9**(2): p. 411-421.
  132. Mosiman, V.L., et al., *Reducing cellular autofluorescence in flow cytometry: an in situ method*. *Cytometry*, 1997. **30**(3): p. 151-6.
  133. Budihardjo, I., et al., *Biochemical pathways of caspase activation during apoptosis*. *Annual review of cell and developmental biology*, 1999. **15**: p. 269.
  134. Starenki, D., et al., *Vandetanib and cabozantinib potentiate mitochondria-targeted agents to suppress medullary thyroid carcinoma cells*. *Cancer Biol Ther*, 2017: p. 0.
  135. Zhang, Y., et al., *Oxymatrine induces mitochondria dependent apoptosis in human osteosarcoma MNNG/HOS cells through inhibition of PI3K/Akt pathway*. *Tumor Markers, Tumor Targeting and Translational Cancer Research*, 2014. **35**(2): p. 1619-1625.
  136. Jonathan, M.L., *Inhibition of p53-dependent apoptosis by the KIT tyrosine kinase: regulation of mitochondrial permeability transition and reactive oxygen species generation*. *Oncogene*, 1998. **17**(13): p. 1653.

- 
137. Chou, Y.-C., et al., *PEITC induces apoptosis of Human Brain Glioblastoma GBM8401 Cells through the extrinsic- and intrinsic -signaling pathways*. *Neurochemistry International*, 2015. **81**: p. 32-40.
  138. Cohen, A., S. Holmen, and H. Colman, *IDH1 and IDH2 Mutations in Gliomas*. *Current Neurology and Neuroscience Reports*, 2013. **13**(5): p. 1-7.
  139. Oizel, K., et al., *D-2-Hydroxyglutarate does not mimic all the IDH mutation effects, in particular the reduced etoposide-triggered apoptosis mediated by an alteration in mitochondrial NADH*. *Cell Death and Disease*, 2015. **6**(3): p. e1704.
  140. Carlsson, J., et al., *Formation and growth of multicellular spheroids of human origin*. *International Journal of Cancer*, 1983. **31**(5): p. 523-533.
  141. Navis, A.C., et al., *Effects of Dual Targeting of Tumor Cells and Stroma in Human Glioblastoma Xenografts with a Tyrosine Kinase Inhibitor against c-MET and VEGFR2.(Research Article)(vascular endothelial growth factor receptor 2)(Report)*. *PLoS ONE*, 2013. **8**(3): p. e58262.
  142. Truffaux, N., et al., *Preclinical evaluation of dasatinib alone and in combination with cabozantinib for the treatment of diffuse intrinsic pontine glioma*. *Neuro-Oncology*, 2015. **17**(7): p. 953-964.
  143. Groebe, K. and W. Mueller-Klieser, *On the relation between size of necrosis and diameter of tumor spheroids*. *Int J Radiat Oncol Biol Phys*, 1996. **34**(2): p. 395-401.
  144. Ahn, S.-H., et al., *Necrotic cells influence migration and invasion of glioblastoma via NF- $\kappa$ B/AP-1-mediated IL-8 regulation*. *Scientific reports*, 2016. **6**(1): p. 24552.
  145. Jaal, J., et al., *VEGFR-2 Expression in Glioblastoma Multiforme Depends on Inflammatory Tumor Microenvironment*. *International Journal of Inflammation*, 2015. **2015**.
  146. Kessler, T., et al., *Glioma cell VEGFR-2 confers resistance to chemotherapeutic and antiangiogenic treatments in PTEN-deficient glioblastoma*. *Oncotarget*, 2015. **6**(31): p. 31050-68.
  147. Zhang, Y., et al., *Hepatocyte growth factor sensitizes brain tumors to c-MET kinase inhibition*. *Clinical cancer research : an official journal of the American Association for Cancer Research*, 2013. **19**(6): p. 1433.
  148. Duzgun, Z., Z. Eroglu, and C. Biray Avci, *Role of mTOR in glioblastoma*. *Gene*, 2016. **575**(2 Pt 1): p. 187-90.

- 
149. Gini, B., et al., *The mTOR kinase inhibitors, CC214-1 and CC214-2, preferentially block the growth of EGFRvIII-activated glioblastomas*. *Clinical cancer research : an official journal of the American Association for Cancer Research*, 2013. **19**(20): p. 5722.
  150. Koul, D., *PTEN signaling pathways in glioblastoma*. *Cancer Biol Ther*, 2008. **7**(9): p. 1321-5.
  151. Schiappacassi, M., et al., *p27Kip1 expression inhibits glioblastoma growth, invasion, and tumor-induced neoangiogenesis*. *Molecular cancer therapeutics*, 2008. **7**(5): p. 1164.
  152. Gopinath, S., et al., *Mechanism of p27 upregulation induced by downregulation of cathepsin B and uPAR in glioma*. *Mol Oncol*, 2011. **5**(5): p. 426-37.
  153. Abukhdeir, A.M. and B.H. Park, *p21 and p27: roles in carcinogenesis and drug resistance*. *Expert Rev. Mol. Med.*, 2008. **10**(19).
  154. Payne, S.R., et al., *p27kip1 Deficiency Impairs G2/M Arrest in Response to DNA Damage, Leading to an Increase in Genetic Instability*. *Molecular and Cellular Biology*, 2008. **28**(1): p. 258.
  155. Hüttemann, M., et al., *The multiple functions of cytochrome c and their regulation in life and death decisions of the mammalian cell: From respiration to apoptosis*. *Mitochondrion*, 2011. **11**(3): p. 369-381.
  156. Jiang, X. and X. Wang, *Cytochrome C-mediated apoptosis*. *Annu Rev Biochem*, 2004. **73**: p. 87-106.
  157. Alexander, P. and X.-F. Wang, *Resistance to receptor tyrosine kinase inhibition in cancer: molecular mechanisms and therapeutic strategies*. *Frontiers of Medicine*, 2015. **9**(2): p. 134-138.
  158. Martinho, O., L.E. Zucca, and R.M. Reis, *AXL as a modulator of sunitinib response in glioblastoma cell lines*. *Experimental Cell Research*, 2015. **332**(1): p. 1-10.
  159. Qiang, L., et al., *Isolation and characterization of cancer stem like cells in human glioblastoma cell lines*. *Cancer Lett*, 2009. **279**(1): p. 13-21.
  160. McCarty, J.H., *Glioblastoma resistance to anti-VEGF therapy: has the challenge been MET?* *Clinical cancer research : an official journal of the American Association for Cancer Research*, 2013. **19**(7): p. 1631.





